Black Hole Photon Ring Dimming by Axion-Photon Conversion

野村，皇太

(Degree)
博士（理学）
(Date of Degree)
2024-03-25
(Date of Publication)
2025-03-01
(Resource Type)
doctoral thesis
(Report Number)
甲第8850号
(URL)
https://hdl.handle.net/20.500.14094/0100490075

Doctoral Dissertation

Black Hole Photon Ring Dimming by Axion-Photon Conversion

（アクシオン・光子転換によるブラックホール光子球の減光）

January 2024

Graduate School of Science, Kobe University

Kimihiro Nomura

（野村　皇太）

Abstract

Axions are hypothetical pseudoscalar particles rooted in quantum chromodynamics and string theory. They can assume pivotal roles in cosmology, functioning as inflatons, dark matter, or dark energy. Consequently, the search for the axions stands as one of the paramount challenges in contemporary physics.

In this thesis, we propose an innovative approach to probe the axions through observations of black holes using electromagnetic waves. It is known that magnetic fields are present near black holes and photons can go around the black holes due to strong gravity. When the photons propagate in the magnetic fields over substantial distances, they undergo conversion into axions. The conversion of such photons into axions leads to a dimming of a photon ring encircling the black hole shadow. Our analysis reveals that the photon ring dimming can occur efficiently for supermassive black holes. For instance, in the case of the black hole in the center of the galaxy M87, a dimming of approximately 10% will be observed in the X ray and gamma ray bands. The photon energy band and the extent of the dimming depend on the axion-photon coupling constant and the axion mass. Consequently, the distorted spectrum of the photon ring serves as a valuable tool for elucidating the nature of the axions.

Contents

Chapter 1

Introduction

Axions are hypothetical pseudoscalar particles motivated by physics beyond the Standard Model. Historically, they were initially introduced to address the strong CP problem in quantum chromodynamics (QCD) [1–7]: They can naturally account for why CP symmetry is realized in QCD. Notably, pseudoscalar particles are expected to emerge ubiquitously in string theory [8]. Henceforth, we refer to these pseudoscalar particles simply as axions. Axions can play crucial roles in cosmology [9]. Indeed, heavy axions can realize slow-roll inflation in the very early universe naturally owing to their shift symmetry [10–12]. Light axions can be dark matter [13–17], the key ingredient in cosmic structure formation. Axions with a mass around 10^{-33} eV can mimic a cosmological constant [18–22], potentially accounting for the current accelerated expansion of the universe. Therefore, probing axions and determining their mass hold paramount significance from a cosmological standpoint.

One crucial property of axions is their coupling with photons described by the interaction Lagrangian $\mathcal{L}_{\rm int} = -(g_{a\gamma}/4)\phi F_{\mu\nu}\widetilde{F}^{\mu\nu}$, where $g_{a\gamma}$ is the axion-photon coupling constant, ϕ is the axion field, $F_{\mu\nu}$ is the electromagnetic field strength tensor, and $\widetilde{F}_{\mu\nu}$ is its dual. An intriguing consequence of this interaction is the conversion from photons into axions in the presence of a magnetic field, and vice versa [23, 24]. This axion-photon conversion phenomenon serves as a fundamental principle [25, 26] in the search for solar axions [27, 28] and axion dark matter [29]. Axion-photon conversion has been extensively discussed in cosmological and astrophysical contexts. For example, it is argued that high-energy photons from extragalactic sources reach us through the conversion from photons into axions and subsequent reconversion from axions into photons; otherwise, these photons would be annihilated via electron-positron pair production [30–35]. There are various proposals to account for the recent detections of high-energy gamma rays based on this idea [36–44]. It is also suggested that the conversion will lead to spectral distortions of the cosmic microwave background [45–47] and X/gamma rays from high-energy sources like active galactic nuclei [48–55]. On the other hand, axions may be produced in the cores of supernovae, superclusters, and white dwarfs, and they will be converted into photons that we may observe [56–58]. In any case, the absence of observational signatures can be translated into a constraint on the coupling constant $g_{a\gamma}$. Combining observations [59–61], the upper limit of the coupling constant is currently obtained as $g_{a\gamma} \lesssim 10^{-11}$–$10^{-10}$ GeV^{-1} in the mass range $m_a \lesssim 10^{-5}$ eV.

Recently, the Event Horizon Telescope observed polarized synchrotron emission at 230 GHz from the vicinity of the black hole in the center of the M87 galaxy (M87*), reporting a magnetic field strength of 1–30 Gauss [62]. It is expected that magnetic fields of these orders of magnitude are commonly present around black holes in our universe. Hence, it is intriguing to investigate axion-photon conversion around black holes. In this case, the propagation length of photons required for conversion into axions is typically comparable to or longer than the radius of supermassive black holes. One might initially suspect that a magnetic field sustained over such a radial distance is necessary for conversion. However, we should notice that the strong gravity of the black hole allows the photons to stay in its vicinity for a considerable period of time. Specifically, a black hole spacetime possesses a *photon sphere*, where circular orbits of photons exist. Considering photons emitted from a source outside the black hole, a part of them will first approach the photon sphere, then stay around the sphere for a certain period of time, and eventually escape from the sphere, that we observe. While orbiting the photon sphere, the photons stay at a nearly constant radius around the black hole. This fact automatically ensures the persistence of the magnetic field during propagation. In Refs. [63, 64], the conversion of photons near the photon sphere has been studied focusing on conversion into gravitons. For gravitons, however, the coupling to photons is suppressed by the Planck scale, $M_{\rm Pl}^{-1} \sim 10^{-19}$ GeV^{-1}. In contrast, the coupling of photons to axions is less constrained by observations, making axion-photon conversion potentially more effective. Therefore, in this thesis, we investigate axion-photon conversion near the photon sphere of black holes.

Axion-photon conversion near the black hole photon sphere will hold significant importance in observations of the near black hole region, particularly the bright ring-like image (referred to as the "photon ring") created around the dark region (the "black hole shadow"). Notably, in this thesis, we predict that the number of photons emanating from the vicinity of a black hole will be reduced by conversion into axions, which implies that *the photon ring will be darkened*. Remarkably, we will see that photon ring dimming can occur efficiently for supermassive black holes. In the case of M87*, the dimming is expected to reach 10% in the X ray and gamma ray bands for axions with a coupling constant $g_{a\gamma} \sim 10^{-11}$ GeV^{-1} and mass $m_a \lesssim 10^{-7}$ eV. The analysis in this thesis will demonstrate that the photon energy band and the magnitude of the dimming depend on the values of $g_{a\gamma}$ and m_a. Consequently, observing the distorted spectrum of the photon ring provides a novel tool for probing the properties of axions.

The organization of this thesis is structured as follows:

- Chapter 2 is a review of axions. It begins by presenting several theoretical motivations for introducing axions, particularly in addressing the strong CP problem and within the context of string theory. Following this, the potential roles of axions in cosmology are outlined, encompassing perspectives on inflation, dark matter, and dark energy. The chapter then delves into a detailed examination of the conversion phenomenon between photons and axions in a magnetic field. The photon-axion conversion probability is expressed as a function of propagation distance, emphasizing the pivotal roles of magnetic field strength and axion-photon coupling constant in determining the conversion efficiency and the conversion length (the propagation distance required for conversion). Finally, a brief summary of current experimental constraints on axions is provided.

- Chapter 3 is a review of black hole spacetime. After the concept of the black hole is introduced, the particle orbits around a black hole are studied. Specifically, we demonstrate the existence of circular orbits of photons around a black hole due to strong gravity. It is shown that when observing the black hole, a bright ring-like image can be created by the photon orbits, referred to as the photon ring. Subsequently, the chapter focuses on deriving the orbiting time of photons around a black hole, emphasizing its dependency on the impact parameter of incident photons. The result of the orbiting time is utilized in the subsequent chapter. We conclude the chapter with a discussion of the astrophysical aspects of black holes observed in our universe.

- Chapter 4 is the main part of this thesis, which is based on the author's paper [65]. Building upon the insights gained from the preceding chapters, we study axion-photon conversion in magnetic fields around black holes and its observational consequences. We apply the conversion formula to supermassive black holes and show that efficient conversion can occur due to the long-distance propagation on the photon sphere. Consequently, we observe that the number of photons from the black hole decreases, and thus the ring-like image around the black hole becomes darker, i.e., the *photon ring dimming* occurs, at a certain photon energy band. Furthermore, we derive the expected spectra of photons and axions under a simple modeling of the photon source. We demonstrate that the axion mass and the axion-photon coupling can be read off from the photon spectrum distorted by conversion. Besides, the axion flux produced by conversion is briefly estimated.

- Chapter 5 is devoted to the conclusion and future prospects.

Conventions

In this thesis, unless otherwise noted, the following natural unit system is adopted:

$$c = \hbar = k_{\mathrm{B}} = G = 1\,,$$

where c is the speed of light, $\hbar$ is the reduced Planck constant, k_{B} is the Boltzmann constant, and G is the Newton constant. For electromagnetism, rationalized Heaviside–Lorentz units are used in Chapter 2, while Gaussian units, commonly utilized in astrophysics, are adopted in Chapter 4. The signature of the four-dimensional metric is $(-,+,+,+)$.

Chapter 2

Axions

In this chapter, we provide a review of axions, hypothetical pseudoscalar particles that arise from physics beyond the Standard Model. In Section 2.1, we delve into theoretical motivations for the introduction of axions. These motivations are explored in the context of addressing the strong CP problem and in connection with string theory. In Section 2.2, we examine the potential roles of axions in cosmology from the perspectives of inflation, dark matter, and dark energy. In Section 2.3, a detailed analysis of the conversion phenomenon between photons and axions in the presence of a magnetic field is presented. We express the conversion probability as a function of propagation distance, highlighting the crucial roles of magnetic field strength and the axion-photon coupling constant in determining conversion efficiency. Finally, in Section 2.4, we briefly summarize the current experimental constraints on axions.

This review is grounded in existing literature, with references including [9, 66–70].

2.1 Theoretical Motivations

2.1.1 The QCD Axion

Quantum chromodynamics (QCD) exhibits a kind of unnaturalness known as the "strong CP problem." The general construction of the QCD Lagrangian allows for the inclusion of the following "θ term,"

$$\mathcal{L}_{\theta\mathrm{QCD}} = \frac{\theta_{\mathrm{QCD}}}{32\pi^2}\,\mathrm{tr}\,G_{\mu\nu}\widetilde{G}^{\mu\nu}\,, \tag{2.1}$$

where $G_{\mu\nu}$ represents the gluon field strength, $\widetilde{G}^{\mu\nu} = (1/2)\epsilon^{\mu\nu\rho\sigma}G_{\rho\sigma}$ is its dual, and θ_{QCD} is a constant parameter. This θ term violates CP symmetry and gives rise to an electric dipole moment for the neutron as [71, 72]

$$d_n \sim 10^{-16}\,\theta_{\rm QCD}\,e\ {\rm cm}\,, \tag{2.2}$$

where e is the elementary charge. The dipole moment is experimentally constrained as $|d_n| < 3 \times 10^{-26}\,e$ cm, leading to the bound on the constant parameter $\theta_{\rm QCD}$ as

$$|\theta_{\rm QCD}| \lesssim 10^{-10}\,. \tag{2.3}$$

This constraint implies an extreme fine-tuning, as the parameter $\theta_{\rm QCD}$ encompasses contributions from CP violation in the electroweak sector and the bare violation in the gluon sector induced by instanton effects. Indeed, the observable quantity is expressed as

$$\theta_{\rm QCD} = \bar\theta_{\rm QCD} + \arg\det\, M_u M_d\,, \tag{2.4}$$

where $\bar\theta_{\rm QCD}$ is the bare parameter in the gluon term, and M_u and M_d are the mass matrices for up- and down-type quarks, respectively. From the perspective of low-energy effective field theory, the value of $\theta_{\rm QCD}$ is entirely arbitrary and can even be of $\mathcal{O}(1)$. The apparent fine-tuning implied by the experimental constraints in Eq. (2.3) may suggest the presence of new physics to restore CP symmetry.

The QCD axion is a hypothetical pseudoscalar field coupled to the gluon term ${\rm tr}\, G_{\mu\nu}\widetilde{G}^{\mu\nu}$, initially proposed by Peccei and Quinn [1]. The axion field arises from the spontaneous breaking of a hypothetical global symmetry. The nonperturbative dynamics of QCD generates a nontrivial periodic potential for the axion field at low energies below the confinement scale $\Lambda_{\rm QCD} \sim 200\,{\rm MeV}$. Introducing the axion field is effectively equivalent to replacing the parameter $\theta_{\rm QCD}$ in Eq. (2.1) with a dynamical scalar field, the axion. The expectation value of the axion field settles at the minimum of the potential, where CP becomes conserved. Therefore, the strong CP problem can be resolved. Expanding the axion potential around the minimum, the axion mass is given by

$$m_a \simeq 6 \times 10^{-6}\ {\rm eV}\left(\frac{10^{12}\ {\rm GeV}}{f_a}\right), \tag{2.5}$$

where f_a is the axion decay constant, related to the energy scale of the spontaneous breaking of the introduced hypothetical symmetry.

The coupling of the axion to the gluon term ${\rm tr}\, G_{\mu\nu}\widetilde{G}^{\mu\nu}$ is induced by the anomaly in the chiral rotation on the fermions. Similarly, the chiral anomaly also leads to a coupling of the axion to the electromagnetic field (photon) term $F_{\mu\nu}\widetilde{F}^{\mu\nu}$. The nonperturbative dynamics in QCD further contributes to the axion-photon coupling at low energies. The axion-photon coupling is commonly expressed in the following form,

$$\mathcal{L}_{\rm int} = -\frac{1}{4}\, g_{a\gamma}\, \phi\, F_{\mu\nu} \widetilde{F}^{\mu\nu}\,, \tag{2.6}$$

where ϕ is the canonically normalized axion field, and $g_{a\gamma}$ is the axion-photon coupling constant. The value of $g_{a\gamma}$ depends on each model construction.

In the earliest model, the Peccei–Quinn–Weinberg–Wilczek (PQWW) axion [1–3], where the axion decay constant was identified as the electroweak scale, has been excluded by experiments. In the Kim–Shifman–Vainshtein–Zakharov (KSVZ) axion model [4, 5], in which a scalar field and heavy quarks are introduced, the coupling reads

$$|g_{a\gamma}| \simeq 2.2 \times 10^{-15}\,\mathrm{GeV}^{-1} \left(\frac{10^{12}~\mathrm{GeV}}{f_a} \right). \tag{2.7}$$

In the Dine–Fischler–Srednicki–Zhitnitsky (DFSZ) axion model [6, 7], in which a scalar field and an additional Higgs field are introduced, the coupling is given by

$$|g_{a\gamma}| \simeq 8.7 \times 10^{-16}\,\mathrm{GeV}^{-1} \left(\frac{10^{12}~\mathrm{GeV}}{f_a} \right). \tag{2.8}$$

Different predictions may arise from alternative model constructions.

Note that there is a model-independent property in QCD axion models: The coupling $g_{a\gamma}$ has mass dimension -1 and is necessarily proportional to the inverse of the axion decay constant f_a, resulting in suppression by the energy scale of symmetry breaking. Since the axion mass also depends on f_a, there exists a relationship between the axion mass and the axion-photon coupling constant for the QCD axion.

2.1.2 Axions in String Theory

String theory is anticipated to be the most fundamental theory successfully describing quantum gravity. A consistent formulation of string theory requires that the spacetime dimension is ten (or eleven). To reproduce the four-dimensional spacetime we observe, one approach is to compactify the extra dimensions. Through this compactification, numerous scalar fields emerge as Kaluza–Klein zero modes associated with the antisymmetric tensor fields present in the theory [8]. These scalar fields share similar properties with the QCD axion, such as an approximate shift symmetry, and are therefore referred to as "axion-like particles (ALPs)" or simply "axions." The plausible prediction is the existence of a large number of axions weakly coupled to other particles across a broad mass range. This scenario, where our universe is populated by numerous axions, is known as the "string axiverse" [73].

For the QCD axion, a certain relationship between the mass m_a and the axion-photon coupling constant $g_{a\gamma}$ has been established. However, in the case of the string axion, a simple relationship may not necessarily hold. The consideration of string axions allows for a broader range of possibilities in the parameter space.

2.2 Axions in Cosmology

In this section, we explore the significant roles that axions can play in various cosmological scenes. Henceforth, we will use the term "axion" in the most general sense, referring to a (pseudo)scalar field with an approximate shift symmetry.

2.2.1 Inflation

Inflation is an accelerated expansion phase in the very early universe, expected to account for the observed flatness of space and the large-scale homogeneity we observe today. The simplest inflation model involves a scalar field known as the "inflaton," slowly rolling on a nearly flat potential to achieve a sufficiently long cosmic expansion. Given the approximate shift symmetry of an axion, it naturally emerges as a candidate for the inflaton.

The "natural inflation" model [10] exemplifies axion inflation, utilizing the periodic potential generated by instanton effects,

$$V(\phi) = \Lambda_a^4 \left[1 - \cos\left(\frac{\phi}{f_a}\right)\right], \tag{2.9}$$

where Λ_a represents the energy scale at which nonperturbative dynamics become significant, and f_a is the axion decay constant. Notably, slow-roll inflation is achieved in a parameter set where Λ_a corresponds to the grand unified theory scale $\Lambda_{\rm GUT} \sim 10^{15}$ GeV, and f_a equals the Planck scale $M_{\rm Pl} \sim 10^{19}$ GeV. Although QCD axions cannot be appropriate inflatons, axions in a more general sense, originating from certain high-energy physics, can successfully realize inflation.

From the potential (2.9), the axion mass is given by

$$m_a \sim 10^{11}\,\mathrm{GeV} \left(\frac{\Lambda_a}{10^{15}\,\mathrm{GeV}}\right)^2 \left(\frac{M_{\rm Pl}}{f_a}\right). \tag{2.10}$$

Consequently, a heavy axion with $m_a \sim 10^{11}\,\mathrm{GeV}$ emerges as a viable candidate for the inflaton. However, the original framework, while producing primordial scalar perturbations consistent with observations, predicts relatively large primordial tensor perturbations that are in tension with Planck satellite observations [74]. Nonetheless, researchers have actively explored possible variations of the axion inflation model, and the unique predictions arising from these variations will be subject to testing in future observations.

2.2.2 Dark Matter

Cosmic observations at various scales, including galaxy rotation curves, galaxy clusters, large-scale structures, and the cosmic microwave background (CMB), provide evidence for the existence of invisible matter, commonly referred to as dark matter [75]. The axion emerges as a viable dark matter candidate due to the suppression of their coupling with other particles by a high energy scale f_a. One of the conventional mechanisms responsible for the production of axion dark matter, known as the *misalignment mechanism*, unfolds through the following sequence of events.

If the axion field arose from spontaneous symmetry breaking during inflation in the early universe, it would undergo a process of homogenization by inflation.[*1] (Here, the axion is not presumed to serve as the inflaton, implying that it does not constitute the primary energy component during inflation.) Subsequently, a potential for the axion is generated due to non-perturbative effects. The equation of motion governing the homogeneous axion field with mass m_a is expressed as

$$\ddot{\phi} + 3H\dot{\phi} + m_a^2\phi = 0\,, \tag{2.11}$$

where the dot denotes the time derivative, and H represents the Hubble expansion rate. Given an initial misalignment from the potential minimum as $\phi_{\rm ini} \neq 0$, the axion field remains at this value during $H \gtrsim m_a$, owing to the presence of the friction term $3H\dot{\phi}$ in the left-hand side of the equation. Subsequently, as $H \lesssim m_a$, the axion field commences coherent oscillations around the potential minimum.

The energy density of the oscillating axion field follows a scaling behavior $\rho_a \propto a^{-3}$, with a representing the cosmic scale factor. This scaling is analogous to that of nonrelativistic matter. Given our knowledge of $H_{\rm eq} \sim 10^{-28}\,\text{eV}$ at matter-radiation equality, an axion with mass $m_a \gtrsim 10^{-28}\,\text{eV}$ can fulfill the role of dark matter [13–17].

The distinctive characteristic of axion dark matter lies in its macroscopic wave-like behavior, leading to the suppression of structure formation at small scales. Consequently, scrutinizing small-scale structures through observations enables the imposition of constraints on this dark matter scenario. A recent proposal posits that a scalar field with a mass lighter than $m_a \sim 10^{-21}\,\text{eV}$, constituting the entire dark matter content, would be incompatible with the matter power spectrum inferred

[*1] If spontaneous symmetry breaking occurs after inflation, the axion field values will not be uniform, and many patches will appear in which the field values differ from each other. This scenario leads to other cosmological consequences, such as the appearance of topological defects like cosmic strings and domain walls.

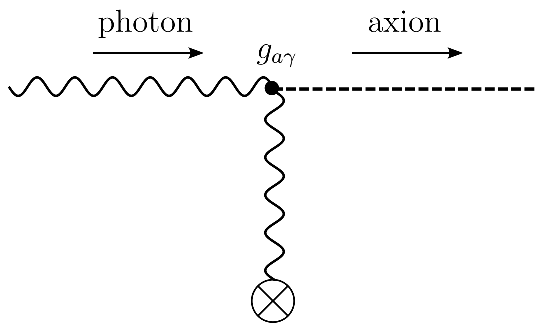

Figure 2.1. In the presence of an external electromagnetic field (denoted by $\otimes$), photons are converted into axions. The inverse process is also possible.

from high-redshift Lyman-α observations [76]. Ongoing and future cosmological observations are poised to refine and extend constraints on the permissible mass range.

2.2.3 Dark Energy

Our universe is currently undergoing accelerated expansion. The energy source that causes the expansion is still unknown and is called dark energy. One way to account for this accelerated expansion is by introducing a positive cosmological constant. However, alternative scenarios explore the possibility of a dynamical field serving as dark energy [18–22].

Consider an axion with the equation of motion given by Eq. (2.11). If the inequality $H > m_a$ holds up to the present time, the axion field remains frozen at its initial value $\phi_{\rm ini}$. This implies that the energy density of the axion remains approximately constant at $V(\phi_{\rm ini}) \simeq (1/2)m_a^2\phi_{\rm ini}^2$, resembling the behavior of a positive cosmological constant. Given the present Hubble expansion rate $H_0 \sim 10^{-33}\,\text{eV}$, this scenario holds for an axion with a mass $m_a \lesssim 10^{-33}\,\text{eV}$. Slightly heavier axions may undergo a slow roll down the potential throughout cosmic history. While such axions could still act as dark energy, their predictions differ from those of a cosmological constant and are subject to observational tests.

2.3 Axion-Photon Conversion

A phenomenologically important property of axions is their interaction with photons, as indicated in Eq. (2.6). This interaction occurs between one axion and two photons. Now, let us examine a scenario involving an external electromagnetic field. By substituting one photon linked to the interaction vertex with the external field, we observe a mixing of a photon and an axion, as depicted in Figure 2.1. This implies that photons propagating in an external electromagnetic field can be converted into axions, and vice versa. This conversion phenomenon is known as the Primakoff process. (Originally, Primakoff [77] investigated the conversion of photons to neutral pions in external electric fields, such as the Coulomb field of nuclei.)

The axion-photon conversion process forms the fundamental principle in various axion detection experiments. In this section, we provide a review of the derivation of the conversion probability between photons and axions in the presence of a background magnetic field, following Raffelt and Stodolsky [24]. Throughout this section, we adopt natural units where $c = \hbar = 1$. Additionally, we use rationalized Heaviside–Lorentz units for electromagnetism, where 4π does not appear in the Maxwell equations but does in the Coulomb law. In the subsequent manipulations, we operate in flat space.

We consider a system of axions and photons described by the following Lagrangian:

$$\mathcal{L} = -\frac{1}{4}F_{\mu\nu}F^{\mu\nu} - \frac{1}{2}\partial_\mu\phi\partial^\mu\phi - \frac{1}{2}m_a^2\phi^2 - \frac{1}{4}g_{a\gamma}\phi F_{\mu\nu}\widetilde{F}^{\mu\nu}\,, \tag{2.12}$$

where $F_{\mu\nu}$ is the electromagnetic field strength tensor, ϕ is the axion field, m_a is the mass of the axion, $g_{a\gamma}$ is the axion-photon coupling constant, and $\widetilde{F}_{\mu\nu} = (1/2)\epsilon_{\mu\nu\rho\sigma}F^{\rho\sigma}$ is the Hodge dual of $F_{\mu\nu}$. Here, the tensor $\epsilon_{\mu\nu\rho\sigma}$ is completely antisymmetric in the indices and normalized as $\epsilon_{0123} = 1$.

From the above Lagrangian, the equation of motion for axions is given by

$$\Box\phi - m_a^2\phi = \frac{1}{4}g_{a\gamma}F_{\mu\nu}\widetilde{F}^{\mu\nu}\,, \tag{2.13}$$

where $\Box = \partial^\mu\partial_\mu$. On the other hand, the equation of motion for photons reads

$$\partial_\mu F^{\mu\nu} = -g_{a\gamma}\widetilde{F}^{\mu\nu}\partial_\mu\phi\,. \tag{2.14}$$

Here, the Bianchi identity $\partial_\mu\widetilde{F}^{\mu\nu} = 0$ is used. This is the Maxwell equation with the coupling to axions.

Let us consider a situation in which electromagnetic waves propagate in a background magnetic field. The total electromagnetic field is the sum of the background magnetic field and the electromagnetic waves. We express the total field as

$$F_{\mu\nu} = \bar{F}_{\mu\nu} + \partial_\mu A_\nu - \partial_\nu A_\mu\,. \tag{2.15}$$

Here, the background field is denoted by $\bar{F}_{\mu\nu}$. For simplicity, we assume that the background magnetic field is static and uniform. Representing the background magnetic field vector as $\mathbf{B} = (B_i)$, the components of $\bar{F}_{\mu\nu}$ are given by

$$\bar{F}_{0i} = 0\,, \tag{2.16}$$

$$\widetilde{\bar{F}}_{0i} = \frac{1}{2}\epsilon_{0ijk}\bar{F}_{jk} = B_i (= \text{const.}) \tag{2.17}$$

On the other hand, in Eq. (2.15), the propagating photon field is represented by A_μ. For the propagating photons, we adopt the Coulomb gauge condition

$$\boldsymbol{\nabla} \cdot \mathbf{A} = 0\,. \tag{2.18}$$

Hereafter, we consider equations in the linear order of A_μ or ϕ. Under the Coulomb gauge, the spatial components of the Maxwell equation (2.14) read

$$\Box\mathbf{A} - \boldsymbol{\nabla}\dot{A}^0 = g_{a\gamma}\mathbf{B}\dot{\phi}\,, \tag{2.19}$$

where a dot represents the time derivative. The A^0 component is determined by a constraint equation following from the $\nu = 0$ component of Eq. (2.14),

$$\boldsymbol{\nabla}^2 A^0 = -g_{a\gamma}\mathbf{B} \cdot \boldsymbol{\nabla}\phi\,. \tag{2.20}$$

Meanwhile, the equation of motion for axions (2.13) is recast as

$$(\Box - m_a^2)\phi = -g_{a\gamma}\mathbf{B} \cdot (\dot{\mathbf{A}} + \boldsymbol{\nabla}A^0)\,. \tag{2.21}$$

From Eqs. (2.19) and (2.21), it can be seen that only the component of $\mathbf{A}$ parallel to the background magnetic field $\mathbf{B}$ couples to the axion ϕ. Let us take $\mathbf{A}$ and ϕ to be plane waves propagating along the z direction. Then, the A_z component vanishes because of the Coulomb gauge condition. Without loss of generality, we can take $\mathbf{B}$ to lie in the x-z plane. In the (x, y, z) coordinates, we set

$$\mathbf{B} = (B\sin\Theta, 0, B\cos\Theta)\,, \tag{2.22}$$
$$\mathbf{A} = (A_\parallel(t,z), A_\perp(t,z), 0)\,, \tag{2.23}$$

where Θ is the angle between the direction of $\mathbf{B}$ and the z axis (the direction of the wave number vector of the propagating fields). See Figure 2.2.

In the free field approximation, neglecting the axion-photon coupling, we can set $A^0 = 0$, and $A_\parallel$ and $A_\perp$ have plane wave solutions $\propto e^{-i(\omega t - kz)}$ with $\omega = k$. Furthermore, we consider relativistic axions with a large momentum $k \gg m_a$, so it is also a valid approximation to take the axions as the plane wave $\propto e^{-i(\omega t - kz)}$ with $\omega = k$. In the presence of the coupling, the A^0 component is generally sourced via Eq. (2.20). However, as long as we consider the ϕ field propagating in the z direction, the A_0 should also have spatial dependence only in the z direction. Thus, the A_0 does not contribute to the motion of $A_\parallel$ and $A_\perp$ as seen from Eq. (2.19). Moreover, since the sourced A_0 is of order $g_{a\gamma}$, it should appear in Eq. (2.21) at higher order of $g_{a\gamma}$. For these reasons, we will completely neglect A_0.

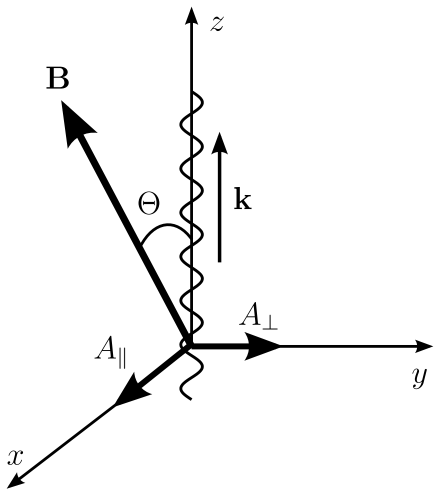

Figure 2.2. The direction of propagation of photons (wave number vector $\mathbf{k}$) is chosen to be along the z axis. The background magnetic field $\mathbf{B}$ lies in the x-z plane. The polarization components of the photons in the x and y directions are denoted by $A_\parallel$ and $A_\perp$, respectively.

As the background magnetic field becomes stronger, quantum effects such as virtual electron pair production become non-negligible. Virtual electron loops induce nonlinear interactions of electromagnetic fields, which are described by the Euler–Heisenberg effective Lagrangian [78, 79]. In the leading order, the effective Lagrangian reads

$$\mathcal{L}_{\mathrm{EH}} = \frac{\alpha^2}{90 m_e^4}\left[(F_{\mu\nu}F^{\mu\nu})^2 + \frac{7}{4}(F_{\mu\nu}\widetilde{F}^{\mu\nu})^2\right], \tag{2.24}$$

where $\alpha = 1/137$ is the fine-structure constant and $m_e = 511$ keV is the electron mass. Originated from this effective Lagrangian, the following term

$$\frac{4\alpha^2}{45 m_e^4}\partial_\mu\left(F_{\rho\sigma}F^{\rho\sigma}F^{\mu\nu} + \frac{7}{4}F_{\rho\sigma}\widetilde{F}^{\rho\sigma}\widetilde{F}^{\mu\nu}\right) \tag{2.25}$$

is added to the right-hand side of Eq. (2.14). Using the parametrizations in Eqs. (2.22) and (2.23), we obtain

$$F_{\mu\nu}F^{\mu\nu} = 2B^2 - 4(\partial_z A_\perp)B\sin\Theta\,, \tag{2.26}$$

$$F_{\mu\nu}\widetilde{F}^{\mu\nu} = -4(\partial_t A_\parallel)B\sin\Theta\,, \tag{2.27}$$

in the linear order of $\mathbf{A}$.

Since the contribution from the effective Lagrangian itself is expected to be small, it is reasonable to substitute the free field limit. Then, at the leading approximation, the $\nu = x$ component of Eq. (2.25) reads

$$-\omega^2 \frac{4\alpha^2}{45 m_e^4} 7 (B \sin\Theta)^2 A_\parallel \,, \tag{2.28}$$

and the $\nu = y$ component reads

$$-\omega^2 \frac{4\alpha^2}{45 m_e^4} 4 (B \sin\Theta)^2 A_\perp \,. \tag{2.29}$$

By adding these terms to the right-hand side of Eq. (2.19), we have

$$\Box A_\parallel + 7\omega^2 \xi \sin^2\Theta A_\parallel - g_{a\gamma} B \sin\Theta \dot{\phi} = 0 \,, \tag{2.30}$$

$$\Box A_\perp + 4\omega^2 \xi \sin^2\Theta A_\perp = 0 \,, \tag{2.31}$$

where $\Box = -\partial_t^2 + \partial_z^2$ and

$$\xi \equiv \frac{\alpha}{45\pi} \left(\frac{B}{B_{\rm crit}} \right)^2 \tag{2.32}$$

with the critical magnetic field determined by the electron mass m_e and the elementary charge e,

$$B_{\rm crit} \equiv \frac{m_e^2}{e} = 4 \times 10^{13}\,{\rm Gauss} \,. \tag{2.33}$$

Note that the perturbative expansion in Eq. (2.24) is applicable as long as the magnetic field B is sufficiently smaller than the critical value $B_{\rm crit}$. Hereafter, we focus only on $A_\parallel$ to see mixing with the axion.

In reality, the environment in which electromagnetic waves propagate may not be a vacuum. We consider an environment composed of a uniform plasma. In this scenario, incident electromagnetic waves induce oscillations of ionized electrons, generating oscillating electric currents. Consequently, these currents induce an effective mass for the electromagnetic waves, quantified by the plasma frequency

$$\omega_{\rm pl} \equiv \sqrt{\frac{4\pi\alpha n_e}{m_e}} \,, \tag{2.34}$$

where n_e is the number density of the electron. [Here, we neglected the motion of the protons, resulting in a negligible correction of $m_e/m_p \simeq (2 \times 10^3)^{-1}$.] The effective mass induced by the surrounding plasma can be incorporated by adding a term $-\omega_{\rm pl}^2 A_\parallel$ to the Maxwell equation (2.30):[*2]

$$\Box A_\parallel - \omega_{\rm pl}^2 A_\parallel + 7\omega^2 \xi \sin^2\Theta A_\parallel - g_{a\gamma} B \sin\Theta \dot{\phi} = 0\,. \tag{2.35}$$

On the other hand, the equation of motion for the axion (2.21) is now given by

$$(\Box - m_a^2)\phi + g_{a\gamma} B \sin\Theta \dot{A}_\parallel = 0\,. \tag{2.36}$$

To analyze the conversion, it is convenient to express $A_\parallel$ and ϕ as

$$A_\parallel(t,z) = i\,\widetilde{A}(z) e^{-i(\omega t - kz)} + \text{c.c.}\,, \tag{2.37}$$

$$\phi(t,z) = \widetilde{\phi}(z) e^{-i(\omega t - kz)} + \text{c.c.}\,, \qquad \omega = k\,. \tag{2.38}$$

The factor i in the right-hand side of Eq. (2.37) is included for later convenience. The plane wave $e^{-i(\omega t - kz)}$ satisfies the free and massless wave equations, $\Box A_\parallel(t,z) = \Box\phi(t,z) = 0$. We investigate how the photons propagating over a distance in the z direction are converted into axions. We incorporate the z-dependent amplitudes, $\widetilde{A}(z)$ and $\widetilde{\phi}(z)$, to observe how these amplitudes vary with distance z.

It is expected that the variation of these amplitudes due to the coupling is slow, i.e., $|\partial_z^2 \widetilde{A}(z)| \ll k|\partial_z \widetilde{A}(z)|$ and $|\partial_z^2 \widetilde{\phi}(z)| \ll k|\partial_z \widetilde{\phi}(z)|$. Thus, we have

$$\Box A_\parallel(t,z) \simeq 2i\omega(i\,\partial_z \widetilde{A}(z)) e^{-i(\omega t - kz)} + \text{c.c.}\,, \tag{2.39}$$

$$\Box\phi(t,z) \simeq 2i\omega \partial_z \widetilde{\phi}(z) e^{-i(\omega t - kz)} + \text{c.c.} \tag{2.40}$$

These are the leading approximations to observe the z-dependence of the amplitudes $\widetilde{A}(z)$ and $\widetilde{\phi}(z)$. Now, the equations of motion are reduced to

$$i\frac{d}{dz}\begin{pmatrix} \widetilde{A}(z) \\ \widetilde{\phi}(z) \end{pmatrix} = \begin{pmatrix} \Delta_{\rm pl} - \Delta_{\rm vac} & -\Delta_{\rm M} \\ -\Delta_{\rm M} & \Delta_a \end{pmatrix} \begin{pmatrix} \widetilde{A}(z) \\ \widetilde{\phi}(z) \end{pmatrix}\,, \tag{2.41}$$

where $\Delta_{\rm M}$, Δ_a, $\Delta_{\rm pl}$, and $\Delta_{\rm vac}$ are defined as follows:[*3]

$$\Delta_{\rm M} \equiv \frac{1}{2} g_{a\gamma} B \sin\Theta\,, \tag{2.42}$$

[*2]In the case of plasma with finite temperature, there is additional random thermal motion of electrons and protons, resulting in pressure. However, as long as we consider transverse electromagnetic waves, where electric and magnetic fields are perpendicular to the propagating direction, the thermal pressure has no effect [80]. On the other hand, it is known that pressure allows the presence of longitudinal waves, called Langmuir waves (see, e.g., Ref. [81]), which are outside the scope of our interest.

[*3]The definition of Δ_i's ($i = {\rm M}, a, {\rm pl}, {\rm vac}$) here is not exactly the same as the definition in Ref. [24]. In this thesis, Δ_i's are defined to be all positive. On the other hand, in Ref. [24], they are defined so that the refractive index n_i is expressed as $n_i = 1 + \Delta_i/\omega$. In particular, Δ_a and $\Delta_{\rm pl}$ (denoted by $\Delta^{\rm gas}$ in Ref. [24]) are opposite in sign.

$$\Delta_a \equiv \frac{m_a^2}{2\omega}\,, \tag{2.43}$$

$$\Delta_{\rm pl} \equiv \frac{\omega_{\rm pl}^2}{2\omega}\,, \tag{2.44}$$

$$\Delta_{\rm vac} \equiv \frac{7}{2}\omega\frac{4\alpha^2}{45m_e^4}(B\sin\Theta)^2\,. \tag{2.45}$$

We rewrite the above equation (2.41) as

$$i\frac{d}{dz}\vec{\Psi}(z) = \mathbf{M}\vec{\Psi}(z)\,. \tag{2.46}$$

Here, we used the notations

$$\vec{\Psi}(z) = \begin{pmatrix} \widetilde{A}(z) \\ \widetilde{\phi}(z) \end{pmatrix}, \qquad \mathbf{M} = \begin{pmatrix} \Delta_{\parallel} & -\Delta_{\rm M} \\ -\Delta_{\rm M} & \Delta_a \end{pmatrix}, \tag{2.47}$$

where

$$\Delta_{\parallel} \equiv \Delta_{\rm pl} - \Delta_{\rm vac}\,. \tag{2.48}$$

The eigenvalues of the matrix $\mathbf{M}$ are given by

$$\lambda_{\pm} = \frac{\Delta_{\parallel} + \Delta_a \pm \sqrt{(\Delta_{\parallel} - \Delta_a)^2 + 4\Delta_{\rm M}^2}}{2}\,. \tag{2.49}$$

Since $\mathbf{M}$ is a real and symmetric matrix, it can be diagonalized by an orthogonal matrix $\mathbf{R}$ as

$$\mathbf{R}^{\rm T}\mathbf{M}\mathbf{R} = \begin{pmatrix} \lambda_+ & 0 \\ 0 & \lambda_- \end{pmatrix}, \qquad \mathbf{R} = \begin{pmatrix} \cos\theta & -\sin\theta \\ \sin\theta & \cos\theta \end{pmatrix}, \tag{2.50}$$

where θ is a real parameter. Through the direct calculation using the expressions for $\mathbf{M}$ and $\mathbf{R}$ in Eqs. (2.47) and (2.50), we find the off-diagonal component of $\mathbf{R}^{\rm T}\mathbf{M}\mathbf{R}$ as

$$\mathbf{R}^{\rm T}\mathbf{M}\mathbf{R} = \begin{pmatrix} * & * \\ \cos 2\theta(-\Delta_{\rm M}) + \frac{1}{2}\sin 2\theta(\Delta_a - \Delta_{\parallel}) & * \end{pmatrix}. \tag{2.51}$$

Since $\mathbf{R}$ is the matrix that diagonalizes $\mathbf{M}$, the off-diagonal component must vanish. Therefore, the *mixing angle* θ is determined as

$$\tan 2\theta = \frac{2\Delta_{\rm M}}{\Delta_a - \Delta_{\parallel}}\,. \tag{2.52}$$

Using the matrix $\mathbf{R}$, Eq. (2.46) is recast as

$$i\frac{d}{dz}(\mathbf{R}^{\mathrm{T}}\vec{\Psi}(z)) = \begin{pmatrix} \lambda_+ & 0 \\ 0 & \lambda_- \end{pmatrix} (\mathbf{R}^{\mathrm{T}}\vec{\Psi}(z)) \,. \tag{2.53}$$

This equation can be solved as

$$\vec{\Psi}(z) = \mathbf{R} \begin{pmatrix} e^{-i\lambda_+ z} & 0 \\ 0 & e^{-i\lambda_- z} \end{pmatrix} \mathbf{R}^{\mathrm{T}}\vec{\Psi}(0) \,, \tag{2.54}$$

where $\vec{\Psi}(0)$ is provided by the initial condition. Finally, we obtain the general solutions

$$\widetilde{A}(z) = (\cos^2\theta e^{-i\lambda_+ z} + \sin^2\theta e^{-i\lambda_- z})\widetilde{A}(0) + \sin\theta\cos\theta(e^{-i\lambda_+ z} - e^{-i\lambda_- z})\widetilde{\phi}(0) \,, \tag{2.55}$$

$$\widetilde{\phi}(z) = \sin\theta\cos\theta(e^{-i\lambda_+ z} - e^{-i\lambda_- z})\widetilde{A}(0) + (\sin^2\theta e^{-i\lambda_+ z} + \cos^2\theta e^{-i\lambda_- z})\widetilde{\phi}(0) \,. \tag{2.56}$$

We consider the initial condition in which only photons exist, and no axions exist. Given $\widetilde{\phi}(0) = 0$ and $\widetilde{A}(0) = 1$, we obtain the conversion probability at a distance z as

$$\begin{aligned} P_{\gamma\to a}(z) &= |\widetilde{\phi}(z)|^2 \\ &= \sin^2 2\theta \sin^2\left(\frac{\Delta_{\mathrm{osc}}}{2}z\right) \\ &= \left(\frac{\Delta_{\mathrm{M}}}{\Delta_{\mathrm{osc}}/2}\right)^2 \sin^2\left(\frac{\Delta_{\mathrm{osc}}}{2}z\right) \,, \end{aligned} \tag{2.57}$$

where we used Eq. (2.52) and defined

$$\Delta_{\mathrm{osc}}^2 \equiv (\Delta_{\mathrm{pl}} - \Delta_{\mathrm{vac}} - \Delta_a)^2 + 4\Delta_{\mathrm{M}}^2 \,. \tag{2.58}$$

Note that the conversion probability (2.57) exhibits oscillatory behavior with distance z. This oscillation is analogous to that between K^0 mesons and the antiparticles [82], and that between neutrinos [83, 84].

The first maximum of the conversion probability (2.57) is realized at $z = \pi\Delta_{\mathrm{osc}}^{-1}$, at which the maximum value is given by

$$P_{\gamma\to a,\mathrm{max}} = \left(\frac{\Delta_{\mathrm{M}}}{\Delta_{\mathrm{osc}}/2}\right)^2 . \tag{2.59}$$

From Eq. (2.58), we observe that the maximum probability $P_{\gamma\to a,\mathrm{max}}$ approaches unity if $\Delta_{\mathrm{M}} \gg \Delta_{\mathrm{pl}}, \Delta_{\mathrm{vac}}, \Delta_a$ so that $\Delta_{\mathrm{osc}} \simeq 2\Delta_{\mathrm{M}}$. In other words, efficient conversion is possible if the mixing effect Δ_{M} (the off-diagonal component in $\mathbf{M}$) is more dominant than the diagonal components. There is another possibility where the maximum probability approaches unity: Even if $\Delta_{\rm pl}$ is sizable, if $\Delta_{\rm vac}$ and/or Δ_a cancels it in Eq. (2.58), we obtain $\Delta_{\rm osc} = 2\Delta_{\rm M}$. This case in which the photons and axions become degenerate is called the *level crossing.* Eventually, the above examples show that the actual value of $P_{\gamma\to a,\max}$ depends on the situation. Of course, for the conversion probability to reach the maximum value $P_{\gamma\to a,\max}$, the propagation distance of $z = \pi\Delta_{\rm osc}^{-1}$ should be ensured.

In the short distance limit $z \ll \Delta_{\rm osc}^{-1}$, we can expand the $\sin^2$ term in Eq. (2.57) and we obtain

$$P_{\gamma\to a}(z) \simeq \Delta_{\rm M}^2 z^2\,, \qquad \text{for} \;\; z \ll \Delta_{\rm osc}^{-1}\,. \tag{2.60}$$

2.4 Experimental Bounds

In this section, we provide a brief summary of current experimental constraints on axions. For the latest updates and detailed information, reference [85] will be a useful resource.

2.4.1 Solar Axion Search

The sun is anticipated to produce axions through the Primakoff process. The spectral number flux of solar axions detected at Earth is given by [69]

$$\begin{aligned}\frac{d\Phi_a^{\rm sun}}{dE} &= 6.0\times 10^{10}\left(\frac{g_{a\gamma}}{10^{-10}\,{\rm GeV}^{-1}}\right)^2\left(\frac{E}{\rm keV}\right)^{2.481}\\ &\quad\times\exp\left(-\frac{E}{1.205\,{\rm keV}}\right)\,{\rm cm}^{-2}\cdot{\rm sec}^{-1}\cdot{\rm keV}^{-1}\,,\end{aligned} \tag{2.61}$$

where E represents the axion energy. The solar axion distribution peaks at 3 keV. By integrating Eq. (2.61) over energy, the total number flux is obtained as

$$\Phi_a^{\rm sun} = 3.75\times 10^{11}\left(\frac{g_{a\gamma}}{10^{-10}\,{\rm GeV}^{-1}}\right)^2 {\rm cm}^{-2}\cdot{\rm sec}^{-1}\,. \tag{2.62}$$

The total luminosity of the solar axion is estimated as

$$L_a^{\rm sun} = 1.85\times 10^{-3} L_\odot\left(\frac{g_{a\gamma}}{10^{-10}\,{\rm GeV}^{-1}}\right)^2 {\rm cm}^{-2}\cdot{\rm sec}^{-1}\,, \tag{2.63}$$

where $L_\odot = 3.83\times 10^{33}\,{\rm erg/sec}$ is the solar photon luminosity. The average energy of the solar axion is 4.2 keV.

Solar axions can be directly sought through their conversion into X ray photons within a helioscope subjected to a magnetic field. The CERN Axion Solar Telescope (CAST) has not detected any significant signal to date, leading to an upper limit on the axion-photon coupling of [27]

$$g_{a\gamma} < 6.6 \times 10^{-11}\ \mathrm{GeV}^{-1}\,, \qquad \text{for}\ \ m_a \lesssim 0.02\,\mathrm{eV}\,. \tag{2.64}$$

The International AXion Observatory (IAXO), envisioned as the next-generation axion helioscope, is expected to explore the coupling with an order of magnitude greater sensitivity [86].

2.4.2 Astrophysics

Globular Cluster Stars. In our galaxy, there exist many globular clusters, which are gravitationally bound systems of stars formed around the same time. These clusters exhibit characteristic trajectories in a color-magnitude diagram (or Hertzsprung–Russell diagram), plotting surface brightness against surface temperature. Stars on the horizontal branch (HB) of this diagram are believed to have initiated helium burning. The Primakov process, which emits axions, can reduce the lifetime of HB stars for axion masses $m_a \lesssim 100\,\mathrm{keV}$ [69]. Consequently, constraints on the axion-photon coupling can be derived by counting the number of HB stars. An analysis of a sample of 39 globular clusters yielded an upper limit on the axion-photon coupling as [87]

$$g_{a\gamma} < 6.6 \times 10^{-11}\,\mathrm{GeV}^{-1}\,. \tag{2.65}$$

Supernova. In a core-collapse supernova, axions can be produced via the Primakoff process, with an average energy of approximately 100 MeV. As they propagate through the magnetic field in the galaxy, they may be converted into gamma rays, potentially observable concurrently with neutrinos. The absence of a gamma ray signal from the SN1987A supernova sets a constraint on the axion-photon coupling as [56]

$$g_{a\gamma} \lesssim 5.3 \times 10^{-12}\,\mathrm{GeV}^{-1}\,, \qquad \text{for}\ \ m_a \lesssim 4.4 \times 10^{-10}\,\mathrm{eV}\,. \tag{2.66}$$

2.4.3 Axion Dark Matter Search

In Section 2.2.2, we discussed the potential for the axion to serve as a dark matter candidate. The concept of axion-photon conversion can be employed to detect axion dark matter within the galaxy. Dark matter axions, when passing through a microwave cavity with a magnetic field, can undergo conversion into photons, providing an observational signature.

Dark matter axions are sufficiently nonrelativistic, and thus, they have energy closely matching their mass m_a. Consequently, if the cavity's eigenmode aligns with the axion mass, resonant conversion to photons occurs. This resonant behavior allows for searches even with a significantly smaller coupling. The pioneering idea of the axion dark matter haloscope was introduced by Sikivie [25, 88, 89], and it is implemented in the Axion Dark Matter eXperiment (ADMX) [29]. The ADMX has excluded QCD axion dark matter provided by the KSVZ model in the mass range $3.3 \times 10^{-6}\,\mathrm{eV} < m_a < 4.2 \times 10^{-6}\,\mathrm{eV}$, assuming a mass density $\rho_a \gtrsim 0.1\,\mathrm{GeV/cm^3}$ [90].

Chapter 3

Black Holes

In our universe, there are numerous black holes, which are the most massive compact objects. Given that magnetic fields are known to exist around astrophysical black holes, we can anticipate axion-photon conversion, as discussed in Section 2.3. Before delving into this topic, this chapter provides a review of various aspects of black holes.

In Section 3.1, we introduce the concept of the Schwarzschild black hole, which is the spherically symmetric black hole solution in General Relativity. In Section 3.2, we study the trajectories of free particles, i.e., geodesics, around a black hole. In particular, we demonstrate the existence of circular orbits for photons around a black hole due to the strong gravity. It will be revealed that when observing a black hole, a luminous ring-like image, known as the *photon ring*, can be generated by the orbits of photons. In Section 3.3, we derive the orbiting time of photons around a black hole. The obtained result for the orbiting time will be utilized in the subsequent chapter. Finally, Section 3.4 describes the properties of astrophysical black holes observed in our universe and the sources of radiation around them.

Sections 3.1 and 3.2 are dedicated to the review of fundamental concepts of black holes in General Relativity, based on the literature [91, 92]. Section 3.3 delves into a more advanced analysis, relying on Ref. [93] and the author's work [65]. The review of the astrophysical aspects of black holes in Section 3.4 is based on the literature [92, 94, 95].

3.1 The Schwarzschild Solution

In General Relativity, the spherically symmetric solution for a gravitational field in a vacuum is given by the Schwarzschild metric. In spherical coordinates, the Schwarzschild metric is expressed as

$$ds^2 = g_{\mu\nu} dx^\mu dx^\nu = -f(r)\, dt^2 + \frac{1}{f(r)}\, dr^2 + r^2 \left(d\theta^2 + \sin^2\theta\, d\phi^2\right), \tag{3.1}$$

where

$$f(r) = 1 - \frac{2M}{r} \,. \tag{3.2}$$

Here, the constant parameter M represents the mass of the gravitational source. Notice that we adopt the units $c = G = 1$, where c denotes the speed of light, and G is the Newton constant. By combining the mass parameter M with c and G, a dimensionless quantity GM/c^2 is constructed, having the dimension of length. In practice, the parameter M consistently appears in the combination GM/c^2. Consequently, in our $c = G = 1$ units, it is reasonable to consider the mass M as a specific length scale. We define the Schwarzschild radius r_S as

$$r_\mathrm{S} \equiv 2M \,. \tag{3.3}$$

Numerically, the Schwarzschild radius is given by

$$r_\mathrm{S} \sim 3\,\mathrm{km} \left(\frac{M}{M_\odot}\right) , \tag{3.4}$$

where we normalize the mass by the solar mass $M_\odot \sim 10^{33}\,\mathrm{g}$. Referring to the parameter M as the "mass" of the gravitational source is justified by the fact that the metric (3.1) reproduces the Newtonian potential sourced by the mass at a large distance.

The Schwarzschild metric exhibits a peculiar behavior at $r = r_\mathrm{S}$—specifically, the time component of the metric vanishes at this point. Ordinary stellar stars typically have a radius larger than r_S (for instance, the solar radius is $7 \times 10^5\,\mathrm{km}$). For such stars, the metric (3.1) describes the vacuum region exterior, connecting to an internal solution with matter at the surface. Consequently, the metric remains entirely regular for ordinary stellar stars.

In contrast, extraordinarily dense stars, where matter is concentrated within r_S, exhibit anomalous behavior in the metric component. For these highly massive stars, any object or light that enters inside r_S is irreversibly trapped due to the intense gravitational field. The term *black hole* is defined for spacetime structures wherein once a particle enters the interior region, escape becomes impossible. The boundary of the spacetime region that is not causally connected to infinity is called the *event horizon*. When the metric (3.1) is applicable throughout the interior of the Schwarzschild radius r_S, it characterizes a spherically symmetric vacuum black hole, namely, the Schwarzschild black hole. In the case of the Schwarzschild black hole, the event horizon is situated at $r = r_\mathrm{S}$.

3.2 Geodesics and Photon Ring

In this section, we study the behavior of geodesics traced by free particles around a Schwarzschild black hole. Specifically, we will observe that the black hole spacetime allows for circular orbits of photons, giving rise to a luminous ring-like image known as the *photon ring*.

3.2.1 Geodesic Equations

Let us parametrize a geodesic as $x^\mu(\lambda) = (t(\lambda), r(\lambda), \theta(\lambda), \phi(\lambda))$, where λ is an affine parameter. The four-velocity vector U^μ along the trajectory is defined as

$$U^\mu \equiv \frac{dx^\mu}{d\lambda}\,, \tag{3.5}$$

where $x^\mu = x^\mu(\lambda)$ is regarded as a function of the parameter λ. In terms of the four-velocity, the geodesic equation is expressed as

$$U^\nu \nabla_\nu U^\mu = 0\,, \tag{3.6}$$

where ∇_μ is the covariant derivative associated with the spacetime metric $g_{\mu\nu}$. More explicitly, Eq. (3.6) is equivalent to

$$\frac{d^2x^\mu}{d\lambda^2} + \Gamma^\mu_{\nu\rho}\frac{dx^\nu}{d\lambda}\frac{dx^\rho}{d\lambda} = 0\,, \tag{3.7}$$

where

$$\Gamma^\mu_{\nu\rho} = \frac{1}{2}g^{\mu\lambda}(\partial_\nu g_{\lambda\rho} + \partial_\rho g_{\nu\lambda} - \partial_\lambda g_{\nu\rho}) \tag{3.8}$$

represents the Christoffel symbol. The geodesic equation is followed by the trajectory of free particles. Indeed, Eq. (3.7) is a natural generalization of the equation for uniform linear motion in flat spacetime, $d^2x^\mu/d\lambda^2 = 0$, to curved spacetime.

In the following, we normalize the affine parameter λ as

$$-g_{\mu\nu}\frac{dx^\mu}{d\lambda}\frac{dx^\nu}{d\lambda} \equiv \kappa\,, \tag{3.9}$$

where $\kappa = +1$ for massive particles, and $\kappa = 0$ for massless particles. In fact, since the parameter κ defined as Eq. (3.9) is constant along the geodesic, i.e., $d\kappa/d\lambda = 0$, such normalization is always possible. Note that, for massless particles, the affine parameter cannot be fixed by Eq. (3.9) since $\kappa = 0$. We choose the affine parameter for massless particles so that the four-velocity is equal to the four-momentum: $p^\mu = dx^\mu/d\lambda$.

In the Schwarzschild spacetime (3.1), the components of the geodesic equation (3.7) corresponding to $\mu = t$, r, θ, and ϕ are expressed as

$$\frac{d^2t}{d\lambda^2} + \frac{2M}{r^2 f(r)} \frac{dt}{d\lambda} \frac{dr}{d\lambda} = 0\,, \tag{3.10}$$

$$\frac{d^2r}{d\lambda^2} - \frac{M}{r^2 f(r)} \left(\frac{dr}{d\lambda}\right)^2 + \frac{M f(r)}{r^2} \left(\frac{dt}{d\lambda}\right)^2 - r\, f(r) \left[\left(\frac{d\theta}{d\lambda}\right)^2 + \sin^2\theta \left(\frac{d\phi}{d\lambda}\right)^2 \right] = 0\,, \tag{3.11}$$

$$\frac{d^2\theta}{d\lambda^2} + \frac{2}{r} \frac{dr}{d\lambda} \frac{d\theta}{d\lambda} - \cos\theta \sin\theta \left(\frac{d\phi}{d\lambda}\right)^2 = 0\,, \tag{3.12}$$

$$\frac{d^2\phi}{d\lambda^2} + \frac{2}{r} \frac{dr}{d\lambda} \frac{d\phi}{d\lambda} + 2\frac{\cos\theta}{\sin\theta} \frac{d\theta}{d\lambda} \frac{d\phi}{d\lambda} = 0\,, \tag{3.13}$$

respectively.

The four-momentum vector p^μ of massive particles with mass m can be defined as $p^\mu \equiv mU^\mu$ so that the on-shell condition

$$-g_{\mu\nu} p^\mu p^\nu = m^2 \tag{3.14}$$

follows from Eq. (3.9). For massless particles, we have defined the four-velocity U^μ to be equal to the four-momentum p^μ, as mentioned below Eq. (3.9). The notion of these vectors is coordinate-independent. However, we should note that the components of these vectors depend on the chosen coordinate system. For example, what value of momentum would be measured by a local observer at a certain point? The answer is given by noting that the local observer makes measurements based on an orthonormal basis at the observation point. More specifically, we can always introduce an orthonormal tetrad of one-forms $\{e^{\hat{a}}\}$ ($\hat{a} = \hat{0}, \hat{1}, \hat{2}, \hat{3}$) so that the metric is expressed in the form of

$$\begin{aligned} ds^2 &= \eta_{\hat{a}\hat{b}} e^{\hat{a}} e^{\hat{b}} \\ &= -(e^{\hat{0}})^2 + (e^{\hat{1}})^2 + (e^{\hat{2}})^2 + (e^{\hat{3}})^2\,, \end{aligned} \tag{3.15}$$

where $\eta_{\hat{a}\hat{b}} = \mathrm{diag}(-1, +1, +1, +1)$ denotes the components of the Minkowski metric. In the Schwarzschild metric (3.1), we can establish the orthonormal basis $\{e^{\hat{a}}\}$ by using the coordinate basis $\{dx^\mu\}$ as

$$e^{\hat{t}} = \sqrt{f(r)}\, dt\,, \tag{3.16}$$

$$e^{\hat{r}} = \frac{1}{\sqrt{f(r)}}\, dr\,, \tag{3.17}$$

$$e^{\hat{\theta}} = r\, d\theta\,, \tag{3.18}$$

$$e^{\hat{\phi}} = r \sin\theta \, d\phi \,, \tag{3.19}$$

where we relabel $\hat{a} = \hat{0}, \hat{1}, \hat{2}, \hat{3}$ as $\hat{a} = \hat{t}, \hat{r}, \hat{\theta}, \hat{\phi}$, respectively. The dual basis vectors are given by

$$e_{\hat{t}} = \frac{1}{\sqrt{f(r)}} \, \partial_t \,, \tag{3.20}$$

$$e_{\hat{r}} = \sqrt{f(r)} \, \partial_r \,, \tag{3.21}$$

$$e_{\hat{\theta}} = \frac{1}{r} \, \partial_\theta \,, \tag{3.22}$$

$$e_{\hat{\phi}} = \frac{1}{r \sin\theta} \, \partial_\phi \,. \tag{3.23}$$

These basis vectors satisfy the orthonormal condition, $ds^2(e_{\hat{a}}, e_{\hat{b}}) = \eta_{\hat{a}\hat{b}}$. Local measurements will be conducted using the orthonormal tetrad. For example, the local radial momentum of a particle, denoted by $p^{\hat{r}}$, will be given as the component (expansion coefficient) with respect to $e_{\hat{r}}$ when we expand the four-momentum vector p in the orthonormal basis $\{e_{\hat{a}}\}$. We expand the vector p in two ways,

$$p = p^\mu \partial_\mu = p^{\hat{a}} e_{\hat{a}} \,, \tag{3.24}$$

and then, the radial component $p^{\hat{r}}$ can be read off as

$$p^{\hat{r}} = p^\mu \partial_\mu (e^{\hat{r}}) = \frac{m}{\sqrt{f(r)}} \frac{dr}{d\lambda} \tag{3.25}$$

for massive particles. Similarly, the local energy of massive particles is given by

$$p^{\hat{t}} = p^\mu \partial_\mu (e^{\hat{t}}) = m \sqrt{f(r)} \, \frac{dt}{d\lambda} \,. \tag{3.26}$$

The expressions for massless particles can be obtained by the replacement $\lambda/m \to \lambda$. The vector components with respect to the orthonormal tetrad discussed here will be used later to define the local emission angle of particles.

3.2.2 Constants of Motion

It is not straightforward to directly solve the set of geodesic equations (3.10)–(3.13). However, by recognizing the presence of constants of motion, we can analyze the behavior of the solutions in a more simplified manner.

Firstly, since the metric (3.1) describes the spherically symmetric spacetime, we should note that the spacetime has three-dimensional rotational symmetry. Additionally, the Schwarzschild metric exhibits a symmetry under time translation:

$t \to t + \text{const}$. Each symmetry of spacetime implies the existence of the corresponding Killing vector. A Killing vector K^μ is a vector such that

$$\nabla_\mu K_\nu + \nabla_\nu K_\mu = 0\,. \tag{3.27}$$

For a given Killing vector K^μ, the quantity

$$C \equiv K_\mu U^\mu \tag{3.28}$$

is constant along the geodesic. This fact can be understood as

$$\begin{aligned}\frac{dC}{d\lambda} &= \frac{dx^\mu}{d\lambda}\nabla_\mu C \\ &= U^\mu \nabla_\mu (K_\nu U^\nu) \\ &= U^\mu U^\nu \nabla_\mu K_\nu + K_\nu U^\mu \nabla_\mu U^\nu \\ &= 0\,. \end{aligned} \tag{3.29}$$

The first equality follows from the chain rule of differentiation. The first term in the third line vanishes due to the Killing equation (3.27), and the second term vanishes due to the geodesic equation (3.6).

The three-dimensional rotational symmetry corresponds to the three rotational Killing vectors, resulting in the conservation of the three components of angular momentum along the geodesic. In other words, the angular momentum vector of the geodesic motion is conserved. Conservation of the direction of the angular momentum vector indicates that the particle moves in a plane. Therefore, without loss of generality, we can assume the geodesic to lie in the equatorial plane, i.e., $\theta = \pi/2$. This is confirmed by the fact that Eq. (3.12) is solved by $\theta = \pi/2 = \text{const}$. Then, the residual rotational symmetry is $\phi \to \phi + \text{const.}$, and the corresponding Killing vector is the coordinate basis vector in the ϕ direction, ∂_ϕ. In the (t, r, θ, ϕ) coordinates, the components are simply $(\partial_\phi)^\mu = (0, 0, 0, 1)$, and by lowering the index, we obtain

$$(\partial_\phi)_\mu = (0, 0, 0, r^2 \sin^2\theta)\,. \tag{3.30}$$

Following Eq. (3.28), we can derive the conserved quantity L as

$$L \equiv (\partial_\phi)_\mu \frac{dx^\mu}{d\lambda} = r^2 \frac{d\phi}{d\lambda}\,, \tag{3.31}$$

where we used $\sin\theta = 1$ for particles moving in $\theta = \pi/2$. This L represents the magnitude of the conserved angular momentum for massless particles and that per mass for massive particles.

On the other hand, the Killing vector corresponding to the time translation invariance $t \to t + \text{const}$ is the coordinate basis vector in the t direction, ∂_t. The components are $(\partial_t)^\mu = (1, 0, 0, 0)$, and by lowering the index, we obtain

$$(\partial_t)_\mu = (-f(r), 0, 0, 0)\,. \tag{3.32}$$

Correspondingly, the conserved quantity E is given by

$$E \equiv -(\partial_t)_\mu \frac{dx^\mu}{d\lambda} = f(r)\frac{dt}{d\lambda}\,. \tag{3.33}$$

This E represents the conserved energy for massless particles and that per mass for massive particles. The conservation of L and E can also be confirmed directly using the geodesic equations (3.10)–(3.13).

3.2.3 Emission Angle and Impact Parameter

At the end of Section 3.2.1, we have introduced a set of orthonormal basis vectors. Based on the orthonormal basis, the particle momentum measured by a local observer can be deduced. By construction, $e_{\hat{r}}$ is the unit vector parallel of the direction to the black hole, while $e_{\hat{\theta}}$ and $e_{\hat{\phi}}$ are the unit vectors normal to that direction. For massive particles, the local momentum component parallel to the black hole is expressed by

$$p^{\hat{r}} = p^\mu \partial_\mu (e^{\hat{r}}) = \frac{m}{\sqrt{f(r)}} \frac{dr}{d\lambda}\,, \tag{3.34}$$

as already discussed in Eq. (3.25). By taking the coordinate system such that the particle is moving on the equatorial plane ($\theta = \pi/2$), the local momentum component normal to the black hole reads

$$p^{\hat{\phi}} = p^\mu \partial_\mu (e^{\hat{\phi}}) = m\, r\, \frac{d\phi}{d\lambda}\,. \tag{3.35}$$

Equations (3.34) and (3.35) are applicable to massive particles, while those with λ/m replaced by λ correspond to the massless particle case. Dividing $p^{\hat{r}}$ and $p^{\hat{\phi}}$ by the local energy $p^{\hat{t}}$ derived in Eq. (3.26), we obtain the local radial velocity

$$v^{\hat{r}} \equiv \frac{p^{\hat{r}}}{p^{\hat{t}}} = \frac{1}{f(r)} \frac{dr}{dt} \tag{3.36}$$

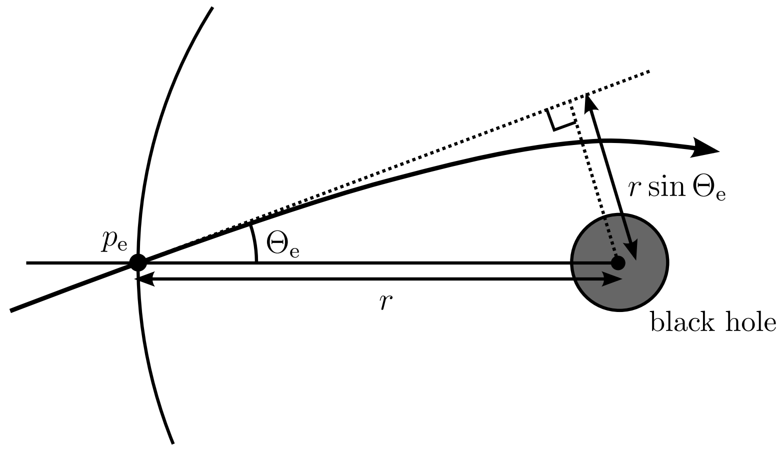

Figure 3.1. A particle is emitted at a point p_e toward a black hole. The view from above of the plane of the particle motion is depicted. On the plane, the local emission angle Θ_e is defined.

and the local tangent velocity

$$v^{\hat{\phi}} \equiv \frac{p^{\hat{\phi}}}{p^{\hat{t}}} = \frac{r}{\sqrt{f(r)}} \frac{d\phi}{dt} \,. \tag{3.37}$$

Note that, at infinity ($r \to \infty$), these agree with the conventional notion in flat spacetime as $v^{\hat{r}} \to dr/dt$ and $v^{\hat{\phi}} \to r\, d\phi/dt$.

Now, let us consider a particle emitted at a point p_e toward the black hole. At the emission point p_e, a local observer will see the local momentum of the particle as given in Eqs. (3.34) and (3.35). The ratio of the normal and parallel components corresponds to the angle between the initial direction of the emitted particle and the direction to the center of the black hole as measured by the local observer. Motivated by this fact, we define the local *emission angle* Θ_e as

$$\tan \Theta_e \equiv \frac{p^{\hat{\phi}}}{p^{\hat{r}}} \,. \tag{3.38}$$

Refer to Figure 3.1. From Eq. (3.16)–(3.19), we can express the emission angle in terms of the coordinates as

$$\tan \Theta_e = \frac{r(d\phi/d\lambda)}{(1/\sqrt{f(r)})(dr/d\lambda)} = r\sqrt{f(r)}\, \frac{d\phi}{dr} \,. \tag{3.39}$$

Note that this expression is applicable to both massive and massless particles since the masses m contained in $p^{\hat{\phi}}$ and $p^{\hat{r}}$ are canceled for massive particles, and we defined $U^{\mu} = p^{\mu}$ for massless particles.

If there were no gravity, $r \sin \Theta_e$ would measure the distance between the black hole and the particle when the particle is closest to the black hole, which is nothing but the conventional definition of impact parameter in flat spacetime. As the particle approaches the black hole, gravity becomes more efficient, and the particle orbit will be bent. However, to an observer at a large distance where gravity is sufficiently weak, the particle will appear to have the impact parameter of $r \sin \Theta_{\rm e}$. Therefore, in the context of General Relativity, it is convenient to define the (apparent) *impact parameter* b as

$$b \equiv \lim_{r \to \infty} r \sin \Theta_{\rm e} \,. \tag{3.40}$$

3.2.4 Particle Motion

In light of the conserved quantities, the geodesic motion can be solved as follows. Using the expression of the Schwarzschild metric (3.1), we can write down Eq. (3.9) for the particles in $\theta = \pi/2$ as

$$-f(r)\left(\frac{dt}{d\lambda}\right)^2 + \frac{1}{f(r)}\left(\frac{dr}{d\lambda}\right)^2 + r^2\left(\frac{d\phi}{d\lambda}\right)^2 = -\kappa \,. \tag{3.41}$$

Multiplying this by $f(r)$ and using the definitions of E and L, we obtain

$$-E^2 + \left(\frac{dr}{d\lambda}\right)^2 + f(r)\left(\frac{L^2}{r^2} + \kappa\right) = 0 \,. \tag{3.42}$$

Given L and E, we can integrate this equation to get $r(\lambda)$. Once $r(\lambda)$ is obtained, we can substitute it into Eqs. (3.31) and (3.33), and integrate them to get $\phi(\lambda)$ and $t(\lambda)$. Below, we do not solve the equations explicitly, but examine a general picture of motion by viewing the structure of Eq. (3.42). The cases of massive and massless particles are analyzed separately.

Massive Particles. For massive particles ($\kappa = +1$), it is convenient to rewrite Eq. (3.42) as

$$\frac{1}{2}\left(\frac{dr}{d\lambda}\right)^2 + V(r) = \mathcal{E} \,, \tag{3.43}$$

where we introduced the "effective potential"

$$V(r) = \frac{1}{2} - \frac{M}{r} + \frac{L^2}{2\,r^2} - \frac{ML^2}{r^3} \tag{3.44}$$

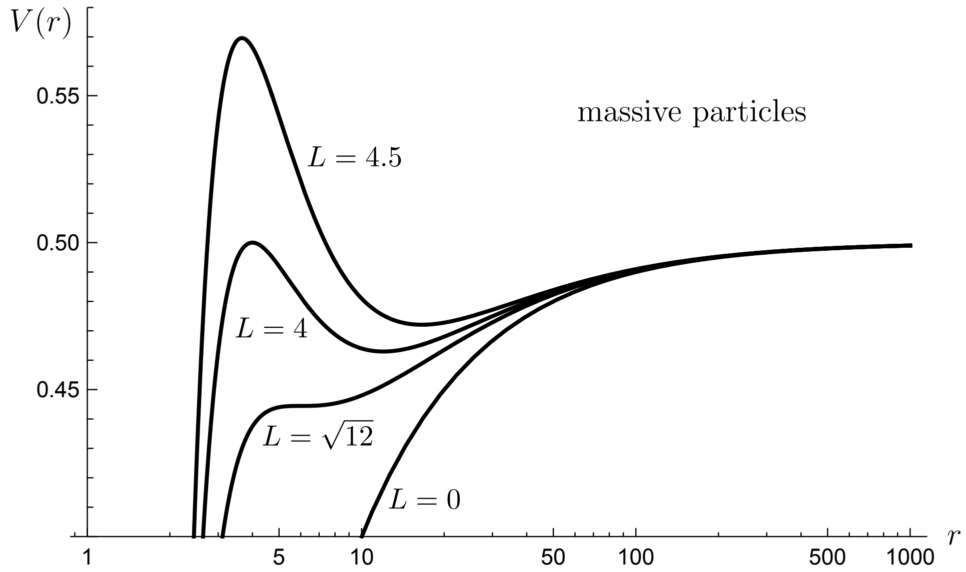

Figure 3.2. The "effective potential" $V(r)$ for massive particles with various L. All dimensional quantities are normalized by M.

and

$$\mathcal{E} = \frac{1}{2}E^2 \,. \tag{3.45}$$

Equation (3.43) shows that the current situation is equivalent to a problem of Newtonian mechanics for a particle of "energy" $\mathcal{E}$ moving in a one-dimensional potential $V(r)$. The particles can move only in the region satisfying $\mathcal{E} \geq V(r)$. Note that the last term in Eq. (3.44) proportional to $1/r^3$ is the effect of General Relativity, which will be dominant at small r. The shape of the effective potential $V(r)$ for various values of L is depicted in Fig.3.2, in which we normalize r and L by M.

Particles approaching the black hole from the outside with finite "energy" $\mathcal{E}$ continuously reduce the radial coordinate r until they reach the barrier of the effective potential $V(r)$. At the point where the particle hits the potential barrier, $\mathcal{E} = V(r)$, the radial velocity $dr/d\lambda$ vanishes as indicated by Eq. (3.43). After hitting the potential barrier, the radial velocity changes sign, and then, the particle moves outward. In other words, the particle is scattered by the black hole.

On the other hand, as illustrated in Fig. 3.2, particles arriving from outside with sufficiently large $\mathcal{E}$ for a given L will continue falling toward $r = 0$ without hitting the potential barrier. Such particles are absorbed into the black hole. It is noteworthy that the effective potential $V(r)$ identically vanishes at $r = 2M$, irrespective of L. Consequently, any particle entering inside $r = 2M$ can never escape, thus characterizing the intrinsic nature of a black hole.

The effective potential for massive particles approaches the asymptotic value $V(r) \to 1/2$ as $r \to \infty$. Consequently, particles with $\mathcal{E} = 1/2$ (equivalently, $E = 1$)

will come to a stop at infinity. This is consistent with the fact that E represents energy per unit mass, and for static particles at infinity, E should be unity. For $L = 4M$, the local maximum of the effective potential is also $1/2$. As L increases, the top of the effective potential becomes higher. Therefore, particles at rest or in the non-relativistic limit at infinity ($E \simeq 1$) will be scattered by the black hole if $L > 4M$, or absorbed into the black hole if $L < 4M$.

The effective potential $V(r)$ can exhibit a local minimum and a local maximum depending on the value of L. Let $V(r_{\mathrm{c}-})$ and $V(r_{\mathrm{c}+})$ represent the local minimum and the local maximum for a given L, respectively. Particles with an "energy" $\mathcal{E}$ equal to $V(r_{\mathrm{c}-})$ can be captured by the potential minimum, and they become stationary at $r = r_{\mathrm{c}-}$. Thus, the $r = r_{\mathrm{c}-}$ corresponds to stable circular orbits. On the other hand, the radial position of the local maximum $r = r_{\mathrm{c}+}$ corresponds to unstable circular orbits. Particles with $\mathcal{E}$ equal to $V(r_{\mathrm{c}+})$ can trace circular orbits at $r = r_{\mathrm{c}+}$, but once some perturbation is added, they will either move outward or be absorbed into the black hole with finite radial velocity. The values of $r_{\mathrm{c}\pm}$ can be found as the roots of $dV(r)/dr = 0$. From Eq. (3.44), we obtain

$$r_{\mathrm{c}\pm} = \frac{L^2 \mp L\sqrt{L^2 - 12M^2}}{2M} \,. \tag{3.46}$$

For $L > \sqrt{12}M$, both the minimum and maximum exist, which is also evident from Fig. 3.2. In the limit of large L, the radii of the circular orbits are given by

$$r_{\mathrm{c}+} \to 3M \,, \quad r_{\mathrm{c}-} \to \frac{L^2}{M} \qquad (\text{for } L \to \infty) \,. \tag{3.47}$$

In this limit, the radius of the stable circular orbit becomes far away, and that of the unstable circular orbit approaches $3M$. The smaller L is, the smaller $r_{\mathrm{c}-}$ is, and the larger $r_{\mathrm{c}+}$ is. Thus, the smallest possible radius of unstable circular orbits is $3M$. At $L = \sqrt{12}M$, the two circular orbits become degenerate, and the radius is given by

$$r_{\mathrm{c}} = 6M \,. \tag{3.48}$$

For even smaller L, there is no circular orbit. Thus, $r_{\mathrm{c}} = 6M$ represents the smallest possible radius of stable circular orbits of massive particles. This is why the circular orbit with $r_{\mathrm{c}} = 6M$ is called the *innermost stable circular orbit (ISCO)*.

For massive particles, by setting $\kappa = +1$ in Eq. (3.42), we have

$$\frac{dr}{d\lambda} = \pm\sqrt{E^2 - f(r)\left(\frac{L^2}{r^2} + 1\right)} \,. \tag{3.49}$$

The sign depends on whether the particle is going outward or inward. Our focus is on particles moving inward. From Eq. (3.31), we can express the azimuthal coordinate derivative as

$$\frac{d\phi}{d\lambda} = \frac{L}{r^2} \,. \tag{3.50}$$

By substituting Eqs. (3.49) and (3.50) into Eq. (3.39), we can derive the emission angle for massive particles as

$$\tan\Theta_{\rm e} = \frac{\sqrt{f(r)}}{r} \frac{L}{\sqrt{E^2 - f(r)((L^2/r^2)+1)}} \,, \tag{3.51}$$

where we rewrite $-L(>0)$ as L. (Note that for incident particles with $\tan\Theta_{\rm e} > 0$, $d\phi/d\lambda$ is negative; see Figure 3.1.) Taking the limit as $r \to \infty$, Eq. (3.51) becomes

$$\tan\Theta_{\rm e} \xrightarrow{r\to\infty} \frac{L}{r\sqrt{E^2-1}} \,, \tag{3.52}$$

where we used $f(r) \xrightarrow{r\to\infty} 1$. Consequently, we obtain

$$\sin\Theta_{\rm e} = \sqrt{\frac{\tan^2\Theta_{\rm e}}{1+\tan^2\Theta_{\rm e}}} \xrightarrow{r\to\infty} \frac{L}{r\sqrt{E^2-1}} \,. \tag{3.53}$$

Thus, the (apparent) impact parameter b defined in Eq. (3.40) is expressed in terms of the conserved quantities E and L as

$$b = \frac{L}{\sqrt{E^2-1}} \,. \tag{3.54}$$

This can be considered an alternative definition of the impact parameter for massive particles.

From Eqs. (3.33) and (3.49), we find

$$\left(\frac{dr}{dt}\right)^2 = \frac{(dr/d\lambda)^2}{(dt/d\lambda)^2} = \frac{f^2(r)}{E^2}\left[E^2 - f(r)\left(\frac{L^2}{r^2}+1\right)\right] \,. \tag{3.55}$$

Similarly, Eqs. (3.31) and (3.33) tell us

$$\left(\frac{d\phi}{dt}\right)^2 = \frac{(d\phi/d\lambda)^2}{(dt/d\lambda)^2} = \frac{f^2(r)\,L^2}{r^4E^2} \,. \tag{3.56}$$

From these expressions, we can deduce the magnitude of the local velocity as

$$v^2 \equiv (v^{\hat{r}})^2 + (v^{\hat{\phi}})^2$$

$$
\begin{aligned}
&= \frac{1}{f^2(r)}\left(\frac{dr}{dt}\right)^2 + \frac{r^2}{f(r)}\left(\frac{d\phi}{dt}\right)^2 \\
&= \frac{1}{E^2}\left[E^2 - f(r)\left(\frac{L^2}{r^2}+1\right)\right] + \frac{f(r)\,L^2}{r^2E^2}\,,
\end{aligned} \tag{3.57}
$$

where we used Eqs. (3.36) and (3.37). Taking the limit $r \to \infty$, we obtain

$$
v^2 \xrightarrow{r\to\infty} \frac{E^2-1}{E^2}\,, \tag{3.58}
$$

or equivalently,

$$
E \xrightarrow{r\to\infty} \frac{1}{\sqrt{1-v^2}}\,, \tag{3.59}
$$

which reproduces the result in Special Relativity. Furthermore, in the non-relativistic limit ($v^2 \ll 1$), we have $\sqrt{E^2-1} \to v$. Thus, for non-relativistic particles, we can rewrite the impact parameter (3.54) as

$$
b = \frac{L}{v}\,, \tag{3.60}
$$

where the magnitude of velocity v is measured by a local observer at infinity. We have already seen that the maximum value of L such that the particles are captured by a black hole is given by $4M$. In other words, the maximum impact parameter of particles that are captured by a black hole reads $b_{\rm max} = 4M/v$. As in collider experiments, if we define the capture cross-section of a black hole for free and non-relativistic massive particles as

$$
\sigma_{\rm capt} \equiv \pi\, b_{\rm max}^2\,, \tag{3.61}
$$

our analysis implies

$$
\sigma_{\rm capt} = \frac{4\pi\, r_{\rm S}^2}{v^2}\,, \tag{3.62}
$$

where $r_{\rm S} = 2M$ is the Schwarzschild radius.

Massless Particles. Next, let us move on to the discussion on massless particles. This part is particularly important since we will focus on photons and relativistic axions in the following chapter.

For massless particles, for which we set $\kappa = 0$, Eq. (3.42) leads to

$$
\frac{dr}{d\lambda} = \pm\sqrt{E^2 - \frac{L^2 f(r)}{r^2}}\,, \tag{3.63}
$$

where the sign is determined by whether the particle is moving outward or inward. Substituting this and Eq. (3.31) into Eq. (3.39) yields

$$\tan\Theta_\mathrm{e} = \frac{\sqrt{f(r)}}{r}\frac{L}{\sqrt{E^2 - (L^2 f(r)/r^2)}}\,, \tag{3.64}$$

where we rewrite $-L(>0)$ as L as in the discussion on massive particles. Consequently, we have

$$\sin\Theta_\mathrm{e} = \sqrt{\frac{\tan^2\Theta_\mathrm{e}}{1+\tan^2\Theta_\mathrm{e}}} = \frac{L}{E}\frac{\sqrt{f(r)}}{r}\,. \tag{3.65}$$

Taking the limit $r \to \infty$, we obtain

$$\tan\Theta_\mathrm{e} \xrightarrow{r\to\infty} \frac{L}{r\,E}\,. \tag{3.66}$$

Similarly,

$$\sin\Theta_\mathrm{e} \xrightarrow{r\to\infty} \frac{L}{r\,E}\,. \tag{3.67}$$

Then, for massless particles, the (apparent) impact parameter b defined in Eq. (3.40) reads

$$b = \frac{L}{E}\,. \tag{3.68}$$

This expression can serve as an alternative definition of the impact parameter for massless particles. The same result can be obtained by taking the relativistic limit, i.e., $E \gg 1$, in the expression for massive particles (3.54). (Note that we have defined E as the conserved energy *per particle mass* m for massive particles.) It is notable that from Eq. (3.65) the following relation holds:

$$b = \frac{r}{\sqrt{f(r)}}\sin\Theta_\mathrm{e}\,. \tag{3.69}$$

Equation (3.42) with $\kappa = 0$ is rewritten as

$$\frac{1}{2}\left(\frac{dr}{d\tilde{\lambda}}\right)^2 + V(r) = \mathcal{E}\,, \tag{3.70}$$

where we renormalized the affine parameter λ as

$$\tilde{\lambda} \equiv L\,\lambda\,, \tag{3.71}$$

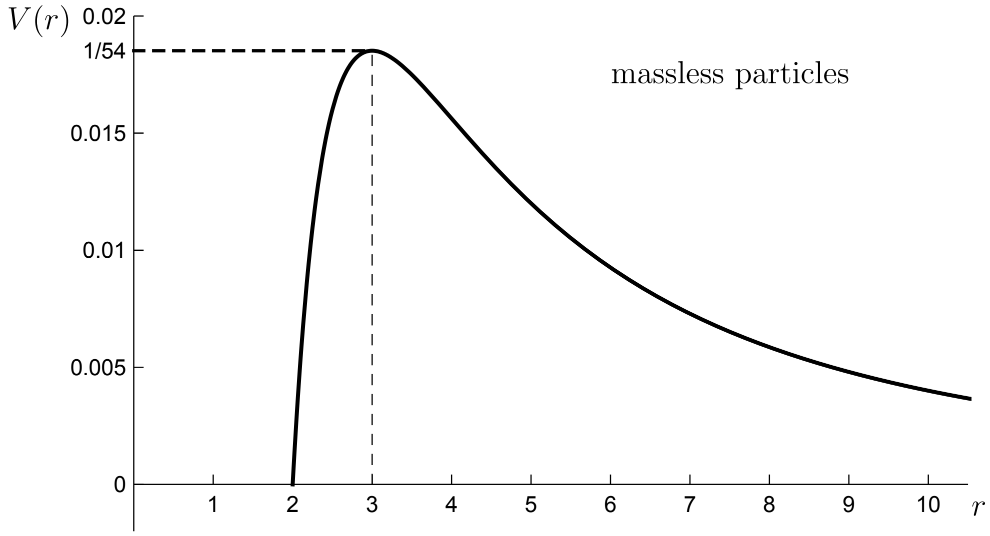

Figure 3.3. The "effective potential" $V(r)$ for massless particles. All dimensional quantities are normalized by M.

and we introduced the "effective potential" for massless particles

$$V(r) = \frac{1}{2\,r^2}\left(1 - \frac{2M}{r}\right), \tag{3.72}$$

and the "energy"

$$\mathcal{E} = \frac{1}{2\,b^2}\,. \tag{3.73}$$

Given $\mathcal{E}$, the massless particle can move within the region satisfying $\mathcal{E} \geq V(r)$. From the structure of Eq. (3.70), it is obvious that the shape of massless particle orbits depends solely on the impact parameter $b = L/E$, and not on E and L independently.

The profile of the "effective potential" $V(r)$ for massless particles is illustrated in Fig. 3.3. The effective potential has a maximum at

$$r_{\rm c} \equiv 3M\,, \tag{3.74}$$

where its value is $V(r_{\rm c}) = 1/(54M^2)$. The fact that the potential maximum occurs at $r = 3M$ is consistent with the outcome of the large L limit in massive particle cases; see Eq. (3.47). The $V(r)$ decreases monotonically from $r_{\rm c}$ to infinity $r \to \infty$. On the other side, the $V(r)$ vanishes at $r = r_{\rm S} = 2M$.

For massless particles approaching the black hole from the outside with a certain $\mathcal{E}$, their fate depends on the value of $\mathcal{E}$. For $\mathcal{E} < V(r_{\rm c}) = 1/(54M^2)$, the particles will reach the point where $\mathcal{E} = V(r)$. Such particles encountering the potential barrier change their velocity towards the outward direction, eventually escaping towards infinity. In other words, the particles are scattered by the black hole. For $\mathcal{E} > V(r_c) = 1/(54M^2)$, the particles persist in moving towards the black hole without encountering the potential barrier. Such particles are inevitably absorbed into the black hole and can never escape again. The critical threshold is $\mathcal{E}_{crit} = 1/(54M^2)$, i.e.,

$$b_{crit} = \sqrt{27}\, M \,, \tag{3.75}$$

which is called the critical impact parameter. As in Eq. (3.61), if we define the capture cross-section of a black hole for massless particles as

$$\sigma_{capt}^{massless} \equiv \pi\, b_{crit}^2 \,, \tag{3.76}$$

it is given by

$$\sigma_{capt}^{massless} = 27\pi M^2 \,. \tag{3.77}$$

If we precisely assign the critical impact parameter b_{crit} to photons, then $r = r_c = 3M = \text{const.}$ is a solution to the geodesic equation. This implies that the Schwarzschild black hole allows for the existence of circular orbits of photons at $r_c = 3M$. However, these circular orbits are *unstable*: Once any perturbation of b is introduced, the photons will either be absorbed into the black hole or will escape towards infinity.

As evident from the analysis of both massive and massless particle orbits, any free particle entering from the outside to the inside of $r_c = 3M$ will follow a geodesic that must be absorbed into the black hole. Notably, the lower limit $r_c = 3M$ emerges in the relativistic (massless) limit. Hence, the sphere of radius $r_c = 3M$ is recognized as one of the surfaces characterizing the strong gravity of black holes, often referred to as the *photon sphere*.

It is noteworthy that the concepts of the photon sphere at $r_c = 3M$ and the event horizon at $r_S = 2M$ are different. The photon sphere is defined as the sphere such that any *free* particle coming *from the outside*, following an *inward geodesic*, cannot escape once it enters the inside. Conversely, when a particle enters just inside $r_c = 3M$, if it is accelerated, for instance, by an electromagnetic force, it will deviate from the geodesic and may then escape. On the other hand, the event horizon is the boundary of the region such that *any physical particle* cannot escape, regardless of the magnitude of its acceleration. Any contact with the outer universe is forbidden by causality.

We anticipate that the photon sphere is a concept of significant observational importance, as the source of inward photons is likely to be distributed well outside the black hole. As mentioned above, photons with $b < b_{\rm crit}$ are absorbed into the black hole. Conversely, photons with $b > b_{\rm crit}$ are scattered by the black hole and, to a distant observer, appear to originate from outside the photon sphere at $r_{\rm c} = 3M$. This implies that no photons can reach the observer from the inside of $r_{\rm c} = 3M$, resulting in a dark region in electromagnetic wave observations known as the *black hole shadow*. Around the black hole shadow, a bright ring-like image is observed, created by photons emanating from the vicinity of the photon sphere. This ring-like image is referred to as the *photon ring* [96, 97]. While the photon sphere radius is $r_{\rm c} = 3M$ in the Schwarzschild coordinates, we should note that the threshold impact parameter is $b_{\rm crit} = \sqrt{27}M$. Therefore, the apparent shadow diameter to a distant observer is given by $2b_{\rm crit} = 2\sqrt{27}M \simeq 10.4M$ [98].

3.3 Orbiting Time of Photons around a Black Hole

In the previous section, we observed the existence of circular orbits for photons at a radius of $r_{\rm c} = 3M$ (photon sphere) around a Schwarzschild black hole. These circular orbits are followed by photons with the critical impact parameter $b_{\rm crit} = \sqrt{27}M$. In this section, we delve into a more detailed examination of the paths taken by photons with an impact parameter b around $b_{\rm crit}$. Specifically, we will provide a formula for the orbiting time of photons around a photon sphere in terms of the impact parameter.

As our focus is on photons that are scattered by a black hole and subsequently reach us, let us consider photons initially traveling inward with $b > b_{\rm crit}$. A schematic picture of the anticipated paths of these photons is depicted in Fig. 3.4. For b close to $b_{\rm crit}$, the photons will encounter the effective potential barrier at a radius outside but close to the photon sphere radius $r_{\rm c} = 3M$. (See the plot of the effective potential for massless particles in Fig. 3.3.) In the vicinity of $r_{\rm c} = 3M$, the circular orbit provides an approximate geodesic solution. As a result, the photons will escape the photon sphere after orbiting around it for a certain duration of time. With a larger difference between $b(> b_{\rm crit})$ and $b_{\rm crit}$, the radius at which the photons encounter the effective potential barrier increases. Consequently, the photons will orbit further outward.

Let us solve the geodesic equation for photons (or more generally, relativistic particles) with b around $b_{\rm crit}$. Combining Eqs. (3.33) and (3.63), we obtain

$$\frac{dr}{dt} = \pm f(r)\sqrt{1 - \frac{b^2 f(r)}{r^2}}\,, \tag{3.78}$$

where the sign $+$ corresponds to outward photons and $-$ to inward photons. In the

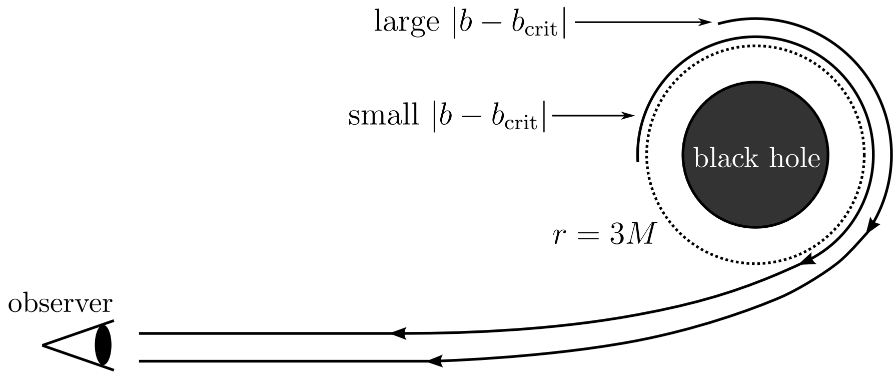

Figure 3.4. A schematic picture of paths followed by photons originating from the vicinity of a black hole is presented. Photons with an impact parameter $b(> b_{\rm crit})$ close to $b_{\rm crit}$ orbit around the photon sphere at $r = 3M$ for a certain duration, after which they travel out to infinity. As the difference between b and $b_{\rm crit}$ increases, the photons travel more distant from the photon sphere, and the duration of their orbit becomes shorter.

critical case $b = b_{\rm crit} = \sqrt{27}M$, Eq. (3.78) can be integrated analytically as

$$t = \pm F(r) \tag{3.79}$$

where we defined the function

$$\begin{aligned} F(r) \equiv & -3\sqrt{3}M \ln\left|\frac{\sqrt{3r}+\sqrt{r+6M}}{\sqrt{3r}-\sqrt{r+6M}}\right| + \sqrt{r(r+6M)} \\ & + 4M\ln\left(\sqrt{\frac{r}{M}+6}+\sqrt{\frac{r}{M}}\right) + 2M\ln\left(\frac{2\sqrt{r}+\sqrt{r+6M}}{2\sqrt{r}-\sqrt{r+6M}}\right). \end{aligned} \tag{3.80}$$

The first term of the right-hand side in Eq. (3.80) implies that $F(r)$ diverges at $r = 3M$, signifying that the photons can travel for an infinitely long time at that radius, which corresponds to the photon sphere. For later convenience, we define a function $\widetilde{F}(t)$ by inverting the equation $t = F(r)$ for $r > 3M$ as

$$r - 3M = \widetilde{F}(t)\,, \tag{3.81}$$

which characterizes the path of outward photons with $b = b_{\rm crit}$ outside the photon sphere as a function of time. The Taylor expansion around $r = 3M$ yields

$$\sqrt{\frac{3r}{M}} - \sqrt{\frac{r+6M}{M}} = \frac{r-3M}{3M} + \mathcal{O}\left(\left(\frac{r-3M}{3M}\right)^2\right). \tag{3.82}$$

Thus, in the vicinity of $r = 3M$, the function $F(r)$ in Eq. (3.80) is approximately given by

$$F(r) \simeq -3\sqrt{3}M \ln\left(\frac{18M}{r-3M}\right) + 3\sqrt{3}\,M \\ + 4M\ln(3+\sqrt{3}) + 2M\ln\left(\frac{2\sqrt{3}+3}{2\sqrt{3}-3}\right) \qquad (\text{for } r \to 3M)\,. \tag{3.83}$$

From this expression, we obtain the function $\widetilde{F}(t) = r - 3M$ in the vicinity of $r = 3M$ as

$$\widetilde{F}(t) \simeq M \exp\left(\frac{t-C}{3\sqrt{3}M}\right) \qquad (\text{for } r \to 3M)\,, \tag{3.84}$$

where the constant C is defined by

$$C = -3\sqrt{3}M\ln 18 + 3\sqrt{3}M + 4M\ln(3+\sqrt{3}) + 2M\ln\left(\frac{2\sqrt{3}+3}{2\sqrt{3}-3}\right). \tag{3.85}$$

From Eq. (3.84), it is evident that photons exponentially depart from the photon sphere with respect to the time coordinate t. On the other hand, the trajectory of inward photons with $b = b_{\text{crit}}$ outside the photon sphere can be obtained by flipping the sign of t in Eq. (3.81).

Now, let us examine photons arriving from outside the black hole with an impact parameter b slightly larger than b_{crit}. It is anticipated that such photons will approach the photon sphere, orbit near the sphere, and eventually escape from it. We model this trajectory as

$$r - 3M = \widetilde{F}(-t-D) + \widetilde{F}(t). \tag{3.86}$$

In the early times, $\widetilde{F}(-t-D)$ is dominant, representing the incident inward photons. Conversely, in the late times, $\widetilde{F}(t)$ becomes dominant, representing the photons flying away from the black hole. The constant D in Eq. (3.86), which should be determined by the impact parameter b, characterizes the duration during which the photons remain in the vicinity of the photon sphere.

To determine the constant D, first, it is essential to note that Eq. (3.86) is approximately given by

$$r - 3M \simeq M\exp\left(\frac{-t-C-D}{3\sqrt{3}M}\right) + M\exp\left(\frac{t-C}{3\sqrt{3}M}\right) \tag{3.87}$$

in the vicinity of $r = 3M$. The minimum of the right-hand side determines the pericenter of the photons' trajectory, i.e., the radial position of the photons when they are closest to the black hole. Let r_{p} denote the radial coordinate of the pericenter.

By finding the minimum of the right-hand side in Eq. (3.87), the $r_{\rm p}$ is given by

$$r_{\rm p} - 3M = 2M \exp\left(\frac{-C - (D/2)}{3\sqrt{3}M}\right) . \tag{3.88}$$

On the other hand, the pericenter $r_{\rm p}$ can be expressed in terms of b by finding the zero of dr/dt given by Eq. (3.78). Introducing $\delta r_{\rm p} = r_{\rm p} - 3M$ and $\delta b = b - b_{\rm crit} (> 0)$, we can perturbatively solve the equation $dr/dt = 0$ as

$$\frac{\delta r_{\rm p}}{3M} = \sqrt{\frac{2}{3}\frac{\delta b}{b_{\rm crit}}} + \mathcal{O}\left(\frac{\delta b}{b_{\rm crit}}\right) . \tag{3.89}$$

By inserting Eq. (3.89) into Eq. (3.88), we can express D in terms of b as

$$D = -2C - 3\sqrt{3}M \ln\left(\frac{b - b_{\rm crit}}{\sqrt{12}M}\right) , \tag{3.90}$$

where we neglected quantities of order $M\mathcal{O}(\sqrt{\delta b/b_{\rm crit}})$.

Let us introduce a small positive parameter ϵ. The first term on the right-hand side in Eq. (3.87) becomes less than $\epsilon M/2$ for $t > -C - D - 3\sqrt{3}M \ln(\epsilon/2)$. Meanwhile, the second term becomes less than $\epsilon M/2$ for $t < C + 3\sqrt{3}M \ln(\epsilon/2)$. Therefore, we can anticipate that the photons remain in a region $3M < r < (3+\epsilon)M$ for the time interval

$$\begin{aligned} T(b) &= 2C + D + 6\sqrt{3}M \ln\frac{\epsilon}{2} \\ &= -3\sqrt{3}M \ln\left[\frac{2(b - b_{\rm crit})}{\sqrt{3}\,\epsilon^2 M}\right] . \end{aligned} \tag{3.91}$$

We refer to this $T(b)$ as the orbiting time of photons within $3M < r < (3+\epsilon)M$, which is the function of the impact parameter b.

Given Eq. (3.91), we can identify the impact parameter at which the orbiting time within $3M < r < (3+\epsilon)M$ vanishes as $b = b_{\rm crit} + \epsilon^2\sqrt{3}M/2$. On the other hand, from Eq. (3.78), the impact parameter with the pericenter $r = (3+\epsilon)M$ turns out to be $b = \sqrt{(3+\epsilon)^3/(1+\epsilon)}M = b_{\rm crit} + \epsilon^2\sqrt{3}M/2 - \epsilon^3 4M/(3\sqrt{3}) + \mathcal{O}(\epsilon^4)$. Photons with b larger than this value cannot enter the region $r < (3+\epsilon)M$. The difference is $\mathcal{O}(\epsilon^3)$, which is originated from the error of $T(b)$ of $M\mathcal{O}(\sqrt{\delta b/b_{\rm crit}})$. Nevertheless, for a small ϵ, this difference becomes negligible, allowing us to regard Eq. (3.91) as a good approximation for the orbiting time in a region $3M < r \lesssim (3+\epsilon)M$. Indeed, the formula (3.91) reproduces the result obtained by solving the geodesic equation numerically [93].

3.4 Black Holes in Our Universe

In this section, we review the properties of astrophysical black holes observed in our universe. First, we present a classification of observed black holes into two categories based on their mass: stellar-mass black holes and supermassive black holes. Subsequently, we discuss the radiative structures in the vicinity of black holes.

3.4.1 Stellar-Mass Black Holes

Stellar-mass black holes are characterized by masses ranging from several to several dozen times that of the sun. They are considered to be one of the final stages in the life of massive stellar stars following gravitational collapse.

The formation of compact objects, including black holes, from main-sequence stellar stars can be summarized as follows. In the dense core of ordinary main-sequence stars, thermal energy is generated through nuclear fusion, converting hydrogen into helium. These stars maintain equilibrium by balancing their self-gravity with the pressure exerted by the hot gas. When the nuclear fuel is exhausted, the temperature decreases, initiating a contraction of the star under the influence of its own gravity. After a certain amount of contraction, an equilibrium state may be reached wherein the Fermi degeneracy pressure of the electrons balances with self-gravity. This stabilized state is denoted as a white dwarf. Nevertheless, beyond the Chandrasekhar limit mass of approximately $1.4M_{\odot}$, the degeneracy pressure becomes insufficient to counteract the self-gravity. In this case, the electrons and protons are combined into neutrons and neutrinos by inverse beta decay. The neutrinos then disperse, leaving a structure composed of high-density neutrons. This resultant object is termed a neutron star, typically characterized by a radius of approximately 10 km. Furthermore, neutron stars also have a maximum possible mass. The upper limit is estimated to be around 3–$4M_{\odot}$ and is referred to as the Tolman–Oppenheimer–Volkov (TOV) limit mass. Any compact object with a mass surpassing this limit is anticipated to have undergone complete gravitational collapse, resulting in the formation of a black hole. More specifically, stellar evolution calculations indicate that main-sequence stars with initial masses greater than $30M_{\odot}$ will eventually evolve into black holes [99].

When stellar-mass black holes form a binary system with another star, they are supplied with gas from the companion star. Then, radiations are emitted as the gas accretes into the black hole. Because of their high compactness, black holes possess a deep gravitational potential, leading to the emission of more energetic radiation, such as X rays, compared to ordinary stars. Consequently, stellar-mass black holes can be observed as X ray sources. The first black hole candidate, known as Cygnus

X-1, is located at a distance of 2 kpc from Earth.

To prove that a compact object in an observed binary system is a black hole, we should determine the mass of the compact object. For this purpose, it is useful to monitor the temporal changes in the redshift of the radiation from the companion star (the radial velocity of the companion star) associated with the orbital motion. If the estimated mass of the compact object exceeds the TOV limit of 3–$4M_\odot$, it is inferred to be a black hole.

3.4.2 Supermassive Black Holes

Since the 1960s, a large number of radiation sources have been observed at far distances enough to experience redshifts due to cosmic expansion. These sources were termed *quasi-stellar objects* or simply *quasars* because of their appearance resembling point sources, similar to stellar stars. The observation that quasars appear luminous even at large distances implies extraordinarily high luminosities, on the order of $10^{13}L_\odot$, which is a hundred times greater than the typical luminosity of galaxies. (Here, $L_\odot$ denotes the solar luminosity.) Moreover, the observation of luminosity variations in quasars on time scales of less than one day suggests a highly compact size, approximately 200 AU $\sim 3 \times 10^{10}$ km.

It is currently recognized that quasars are active galactic nuclei located at cosmological distances. The emission of intense radiation occurs as gas accretes into the supermassive black hole at the center. Here, supermassive black holes collectively refer to black holes with masses far exceeding stellar masses, typically, ranging from millions to billions of times the solar mass. For a Schwarzschild black hole, 6% of the energy is released when a massive particle falls from infinity into the innermost stable circular orbit. In the case of a maximally rotating black hole, the energy release rate can reach up to 42%. Compared to the radiative efficiency of nuclear fusion, which is only 0.7%, black holes exhibit remarkably high efficiency. Seyfert galaxies and blazars are also included in the family of active galactic nuclei, and like quasars, they are believed to emit radiation utilizing a central supermassive black hole as a powerful engine.

Even if intense emissions such as those from active galactic nuclei are not provided, the existence of a supermassive black hole at the center of a galaxy can be inferred by studying the orbital motion of surrounding stars or gases. Currently, supermassive black holes with masses 10^5–$10^{10}M_\odot$ are known to exist in various galactic centers. Let us present two examples of supermassive black holes:

- Sagittarius (Sgr) A*.—This is a radio source located at the center of our Milky Way galaxy, and its emission is supposed to be arising from gas accretion into a supermassive black hole. The distance from Earth is 8 kpc [100]. The mass is estimated to be 4 million solar masses based on the motion of the surrounding stars [101].

- M87*.—Messier 87 (M87) is an elliptical galaxy in the Virgo cluster at a distance of 17 Mpc from Earth [102, 103]. M87* is the supermassive black hole at the center of the M87 galaxy and has a mass of 6 billion solar masses [104, 105].

The two examples above were observation targets for the Event Horizon Telescope to capture black hole shadows in the radio bands [96, 106].

Various scenarios are proposed for the formation of supermassive black holes. One is that supermassive stars were initially formed from huge clumps of gas in the early universe, and they gravitationally collapsed directly. Another scenario is that many stellar-mass black holes grew through repeated mergers. However, the formation theory is not yet completely established. Notably, high-redshift observations at $z \sim 6$ suggest the existence of supermassive black holes within a billion years after the Big Bang. The formation process of these black holes remains under vigorous study [107]. On the other hand, it is observationally indicated that a specific relationship exists between the mass of the supermassive black hole at the center of a galaxy and the mass of the galaxy's bulge as [108]

$$M_{\mathrm{BH}}/M_{\mathrm{bulge}} \sim 0.002\,. \tag{3.92}$$

This relationship implies that galaxies and central black holes have evolved interactively through cosmic history.

3.4.3 Radiation Sources

We end this chapter by discussing the origin of radiations around black holes based on Ref. [94]. As illustrated below, there are several types of radiative structures.

- **Accretion disks.**—The disk is composed of gas that falls toward the black hole while orbiting around it. The structure is geometrically thin but optically thick. The gas is accreted and heated due to friction caused by viscosity originating mainly from magnetic turbulence. The initial gravitational energy of the gas is transformed into heat, leading to thermal radiation. The radiant exitance (the total energy radiated per unit surface area per unit time) of the disk is given by

$$F(r) = \frac{3}{8\pi}\frac{GM\dot{M}}{r^3}\left(1-\sqrt{\frac{r_*}{r}}\right), \tag{3.93}$$

  where $\dot{M}$ is the mass accretion rate and r_* is the inner edge radius of the disk. Typically, r_* is considered to be the radius of the innermost stable circular orbit, which is $r_c = 6GM$ for Schwarzschild black holes. (We restored the gravitational constant G.) From the Stefan–Boltzmann law $F = \sigma T^4$ with the Stefan–Boltzmann constant σ, we can estimate the temperature as

$$T(r) \sim 7 \times 10^6 \text{ K} \left(\frac{M}{10M_\odot}\right)^{-1/2} \left(\frac{\dot{M}}{10^{-8} M_\odot \, \text{yr}^{-1}}\right)^{1/4} \left(\frac{r}{6GM}\right)^{-3/4}. \quad (3.94)$$

For stellar-mass black holes, it is observed that soft X rays are emitted near the inner edge of the disk, while visible and infrared lights emanate from the outer region of the disk around $r \sim 10^4$–$10^5 GM$. On the other hand, for supermassive black holes, the temperature is roughly estimated as

$$T(r) \sim 2 \times 10^5 \text{ K} \left(\frac{M}{10^8 M_\odot}\right)^{-1/2} \left(\frac{\dot{M}}{1 \, M_\odot \, \text{yr}^{-1}}\right)^{1/4} \left(\frac{r}{6GM}\right)^{-3/4}, \quad (3.95)$$

which is cooler than that of stellar-mass black holes. The inner edge of the disk emits ultraviolet rays, while the outer region emits infrared rays and radio waves.

- **Hot accretion flows.**—The accretion disk model is insufficient to account for X ray and gamma ray radiations emitted from supermassive black holes. These high-energy radiations are believed to be generated by geometrically thick and optically thin hot accretion flows. Specifically, the existence of hot advection-dominated accretion flows (ADAF) was suggested in Refs. [109, 110].[*1] In these flows, radiations spanning a wide range of wavelengths, from radio waves to gamma rays, are generated through the following processes [95]:

  1. *Thermal bremsstrahlung.*—Electrons in high-temperature plasmas are not only in thermal motion, but are also accelerated by Coulomb forces from ions. Thermal bremsstrahlung is the radiation produced by the Coulomb acceleration of these thermal electrons. The radiation spectrum is flat up to the frequency determined by the electron temperature and decays exponentially above that frequency.

  2. *Cyclotron (and synchrotron) radiations.*—These are emitted from electrons as they are moved by the Lorentz force to wrap around magnetic field lines. When the electrons are non-relativistic, the emitted radiations are called cyclotron radiations; when the electrons are relativistic, the term synchrotron radiations is used. The radiation frequency is determined by the magnetic field strength B and the Lorentz factor of the

[*1] The radiative efficiency of the ADAF is not as high as that of the accretion disk, so it is also regarded as part of radiatively inefficient accretion flows (RIAF).

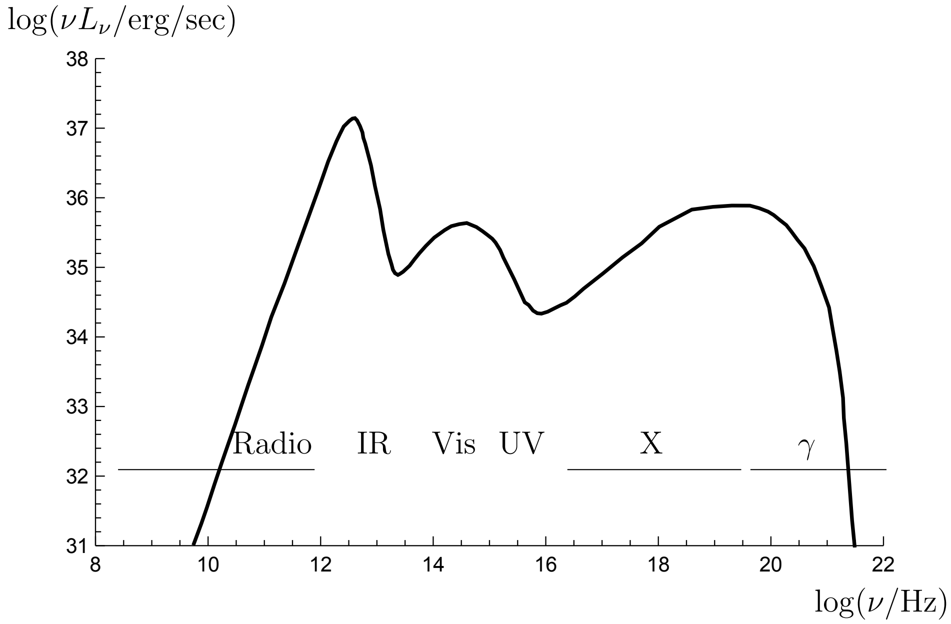

Figure 3.5. The theoretical curve of the spectrum from the optically thin hot accretion flow of the Sagittarius A* black hole. Here, ν represents the frequency, and L_ν represents the spectral luminosity. The curve is taken from Fig. 9 in Ref. [111].

electrons $\gamma = 1/\sqrt{1-(v/c)^2}$:

$$\nu_B \sim 3 \times 10^6 \, \gamma^{-1} \text{ Hz} \left(\frac{B}{\text{Gauss}} \right). \tag{3.96}$$

For magnetic fields of about 1 Gauss, synchrotron radiation falls within the radio band.

3. *Inverse Compton scattering.*—This refers to the process in which low-energy photons are scattered by high-energy electrons and gain energy. When scattered by relativistic thermal electrons, the photon energy is amplified by a factor of $\sim [k_{\rm B}T/(m_e c^2)]^2$, where m_e and T represent the electron mass and temperature, respectively.

Figure 3.5 schematically illustrates the spectrum of radiation emitted from the hot accretion flow for Sgr A* [111]. First, synchrotron radiation produces a peak in the radio and infrared bands. Subsequently, these photons undergo inverse Compton scattering, giving rise to another peak in the visible light region. The peak resulting from the second inverse Compton scattering corresponds to the X ray band. Thermal bremsstrahlung is dominant in high-energy regions such as X and gamma rays. In the frequency band above 100 keV, corresponding to the electron temperature, the spectrum exhibits an exponential decay.

Chapter 4

Axion-Photon Conversion around Black Holes

We have observed in Section 2.3 that photons traveling through magnetic fields are converted into axions, and vice versa. In our universe, substantial magnetic fields surround certain astrophysical entities, such as neutron stars and black holes. Consequently, it is a logical proposition to explore axion-photon conversion around these celestial objects. The advancement in observational techniques, exemplified by the Event Horizon Telescope, has significantly enhanced our ability to study black holes through electromagnetic wave observations in recent years. Therefore, black holes present an observationally compelling domain for investigating axion-photon conversion phenomena.

In this chapter, we delve into the topic of axion-photon conversion around astrophysical black holes and explore its observational implications, based on the author's paper [65]. In Section 4.1, we apply the conversion formula to black holes, demonstrating that efficient conversion can take place within a specific photon energy band. In Section 4.2, we observe that the conversion of photons into axions results in a photon ring dimming within that energy band. It is demonstrated that supermassive black holes are good candidates for efficient dimming, primarily due to the substantial propagation of photons on a very large photon sphere. In Section 4.3, we derive the anticipated photon and axion spectra employing a simplified model for the photon source. We illustrate that the axion mass and the axion-photon coupling can be deduced from the photon spectrum, which is distorted by the conversion process. Additionally, a brief estimation of the axion flux generated through conversion will be provided.

Throughout this chapter, we employ Gaussian units for electromagnetism, distinct from the rationalized Heaviside–Lorentz units used in Chapter 2. Consequently, magnetic fields are measured in the unit of Gauss. Combined with the natural units $c = \hbar = 1$, we have the relation of 1 Gauss $= 1.95 \times 10^{-2}$ eV^2.

4.1 Conversion Probability

In this section, we revisit axion-photon conversion in an external magnetic field discussed in Section 2.3, and apply the formula to black hole magnetospheres. Our analysis will reveal that efficient conversion can take place for X rays and gamma rays propagating near supermassive black holes, such as M87*.

4.1.1 Parameters

The axion-photon conversion phenomenon has been thoroughly reviewed in Section 2.3. For convenience, let us compile the relevant parameters associated with the conversion:

- ω: frequency (or energy) of the propagating photons,
- B: magnetic field strength perpendicular to the photon propagation,
- m_a: axion mass,
- $g_{a\gamma}$: axion-photon coupling constant,
- n_e: number density of the electron in the medium.

Note that the magnetic field component perpendicular to the photon propagation, denoted by $B\sin\Theta$ with the angle Θ in Section 2.3, is here represented simply as B. The number density of the electron n_e is used to determine the plasma frequency as

$$\omega_{\rm pl} \equiv \sqrt{\frac{4\pi\alpha n_e}{m_e}} = 3.7\times 10^{-9}\ {\rm eV}\sqrt{\frac{n_e}{10^4\,{\rm cm}^{-3}}}\,, \tag{4.1}$$

where $m_e = 511\,\mathrm{keV}$ is the electron mass, and $\alpha = 1/137$ is the fine-structure constant. Here, $n_e \sim 10^4\,\mathrm{cm}^{-3}$ is a typical number density in the vicinity of black holes and is used as the reference. As we will see below, we are interested in high energy photons such as X rays, which satisfy $\omega \gg \omega_{\rm pl}$. These high-energy photons can propagate through the plasma without damping, albeit with a modified dispersion relation $\omega = \sqrt{\omega_{\rm pl}^2 + k^2}$, where k represents the wave number.

As derived in Eq. (2.57), after the photons propagate over a distance z, the conversion probability from the photons into axions is expressed by

$$P_{\gamma\to a}(z) = \left(\frac{\Delta_{\rm M}}{\Delta_{\rm osc}/2}\right)^2 \sin^2\left(\frac{\Delta_{\rm osc}}{2}z\right)\,, \tag{4.2}$$

where $\Delta_{\rm osc}$ is defined as

$$\Delta_{\rm osc}^2 \equiv (\Delta_{\rm pl} - \Delta_{\rm vac} - \Delta_a)^2 + 4\Delta_{\rm M}^2\,. \tag{4.3}$$

Here, $\Delta_{\rm M}$, Δ_a, $\Delta_{\rm pl}$, and $\Delta_{\rm vac}$ are given by

$$\Delta_{\rm M} = 9.8 \times 10^{-22}\ \mathrm{eV} \left(\frac{g_{a\gamma}}{10^{-11}\,\mathrm{GeV}^{-1}}\right)\left(\frac{B}{10\,\mathrm{Gauss}}\right), \tag{4.4}$$

$$\Delta_a = 5 \times 10^{-22}\ \mathrm{eV} \left(\frac{m_a}{10^{-9}\,\mathrm{eV}}\right)^2\left(\frac{\mathrm{keV}}{\omega}\right), \tag{4.5}$$

$$\Delta_{\rm pl} = 6.9 \times 10^{-21}\ \mathrm{eV} \left(\frac{n_e}{10^4\,\mathrm{cm}^{-3}}\right)\left(\frac{\mathrm{keV}}{\omega}\right), \tag{4.6}$$

$$\Delta_{\rm vac} = 9.3 \times 10^{-27}\ \mathrm{eV} \left(\frac{\omega}{\mathrm{keV}}\right)\left(\frac{B}{10\,\mathrm{Gauss}}\right)^2, \tag{4.7}$$

respectively. Here, the magnetic field B and the electron number density n_e are normalized by typical values around black holes. The $\Delta_{\rm M}$ determined by $g_{a\gamma}$ and B is an essential parameter for conversion. The effect of a finite axion mass Δ_a, plasma oscillations $\Delta_{\rm pl}$, and the Euler–Heisenberg effective Lagrangian in an external magnetic field incorporating the one-loop corrections of electrons $\Delta_{\rm vac}$, generically suppress the conversion. It is apparent that in certain parameter regions, the factor $\Delta_{\rm M}$ may dominate over the others Δ_a, $\Delta_{\rm pl}$, and $\Delta_{\rm vac}$ for high-energy photons, specifically around X rays and gamma rays with $\omega \gtrsim$ keV.

We should note that the current framework is valid only if the following three conditions are satisfied:

(a) $(\alpha/(45\pi))(B/B_{\rm crit})^2 \ll 1$ where $B_{\rm crit} \equiv m_e^2/\sqrt{4\pi\alpha} = 4 \times 10^{13}$ Gauss, which comes from the validity of the Euler–Heisenberg effective Lagrangian,

(b) $\omega \gg m_a$, i.e., axions should be relativistic,

(c) $\omega \gg \omega_{\rm pl}$ so that photons can propagate in a surrounding plasma.

Indeed, the situations considered in the subsequent analysis satisfy these conditions.

4.1.2 Efficient Conversion

Let us examine when the conversion probability becomes large. The most efficient conversion is achieved when the condition $(\Delta_{\rm pl}-\Delta_{\rm vac}-\Delta_a)^2 \ll 4\Delta_{\rm M}^2$ is met, resulting in $\Delta_{\rm osc} \simeq 2\Delta_{\rm M}$, and the prefactor of the probability (4.2) approaching unity. In this case, the typical length scale of the conversion reads

$$\begin{aligned}\Delta_{\rm osc}^{-1} &\simeq (2\Delta_{\rm M})^{-1}\\ &= 1.0 \times 10^{16}\ \mathrm{cm}\left(\frac{10\,\mathrm{Gauss}}{B}\right)\left(\frac{10^{-11}\ \mathrm{GeV}^{-1}}{g_{a\gamma}}\right)\\ &= 3.4 \times 10^1 \times (2 \times 10^9 M_\odot) \times \left(\frac{10\,\mathrm{Gauss}}{B}\right)\left(\frac{10^{-11}\ \mathrm{GeV}^{-1}}{g_{a\gamma}}\right).\end{aligned} \tag{4.8}$$

From this expression, we see that, for magnetic fields on the order of $B \sim 10^1$–10^2 Gauss, the conversion length becomes comparable to the Schwarzschild radius of a supermassive black hole with a mass of $\sim 10^9$–$10^{10} M_\odot$, assuming $g_{a\gamma} \sim 10^{-11}\,\mathrm{GeV}^{-1}$. Indeed, observations of M87* indicate the mass of $6 \times 10^9 M_\odot$ [96] and a magnetic field of approximately 30 Gauss in the vicinity of the black hole [62]. Due to the ability of photons to stay around the photon sphere of black holes for a certain period of time, efficient conversion into axions is anticipated.

The above condition $(\Delta_{\rm pl} - \Delta_{\rm vac} - \Delta_a)^2 \ll 4\Delta_{\rm M}^2$ is satisfied at least when the axion-photon mixing effect $\Delta_{\rm M}$ dominates over the others Δ_a, $\Delta_{\rm pl}$, and $\Delta_{\rm vac}$. The inequalities $\Delta_a \ll \Delta_{\rm M}$, $\Delta_{\rm pl} \ll \Delta_{\rm M}$, and $\Delta_{\rm vac} \ll \Delta_{\rm M}$ are respectively rewritten as follows.

- $\Delta_a \ll \Delta_{\rm M}$:

$$5.1 \times 10^{-1} \left(\frac{m_a}{10^{-9}\,\mathrm{eV}}\right)^2 \ll \left(\frac{g_{a\gamma}}{10^{-11}\,\mathrm{GeV}^{-1}}\right)\left(\frac{\omega}{\mathrm{keV}}\right)\left(\frac{B}{10\,\mathrm{Gauss}}\right). \tag{4.9}$$

- $\Delta_{\rm pl} \ll \Delta_{\rm M}$:

$$7.0 \times \left(\frac{n_e}{10^4\,\mathrm{cm}^{-3}}\right) \ll \left(\frac{g_{a\gamma}}{10^{-11}\,\mathrm{GeV}^{-1}}\right)\left(\frac{\omega}{\mathrm{keV}}\right)\left(\frac{B}{10\,\mathrm{Gauss}}\right). \tag{4.10}$$

- $\Delta_{\rm vac} \ll \Delta_{\rm M}$:

$$\left(\frac{\omega}{\mathrm{keV}}\right)\left(\frac{B}{10\,\mathrm{Gauss}}\right) \ll 1.1 \times 10^5 \left(\frac{g_{a\gamma}}{10^{-11}\,\mathrm{GeV}^{-1}}\right). \tag{4.11}$$

Except for specific cases (i) and (ii) mentioned later, either Eq. (4.9) or Eq. (4.10) determines the lower bound of ω where conversion occurs efficiently. On the other hand, the upper bound of ω for efficient conversion is given by Eq. (4.11).

Even when the plasma effect is significant, i.e., $\Delta_{\rm pl} \gtrsim \Delta_{\rm M}$, efficient conversion can be realized if $\Delta_{\rm pl}$ is offset by Δ_a or $\Delta_{\rm vac}$. This is possible because $\Delta_{\rm pl}$ contributes to $\Delta_{\rm osc}$ with the opposite sign relative to Δ_a and $\Delta_{\rm vac}$, as we observe in Eq. (4.3). Let us examine these possibilities:

(i) $\Delta_{\rm pl} \simeq \Delta_a$: This condition is equivalent to $m_a^2 \simeq \omega_{\rm pl}^2$, i.e.,

$$\left(\frac{m_a}{10^{-9}\,\mathrm{eV}}\right)^2 \simeq 1.4 \times 10^1 \left(\frac{n_e}{10^4\,\mathrm{cm}^{-3}}\right). \tag{4.12}$$

Here, we assumed that the significant $\Delta_{\rm pl}$ is compensated by the similarly significant Δ_a, which is much larger than $\Delta_{\rm vac}$, i.e.,

$$\left(\frac{\omega}{\mathrm{keV}}\right)^2 \left(\frac{B}{10\,\mathrm{Gauss}}\right)^2 \ll 5.4 \times 10^4 \left(\frac{m_a}{10^{-9}\,\mathrm{eV}}\right)^2. \tag{4.13}$$

Note that, in this case, the conversion can occur at all frequencies satisfying Eq. (4.13) and the conditions for the present treatment to be justified.

(ii) $\Delta_{\rm pl} \simeq \Delta_{\rm vac}$: This condition is written as

$$\left(\frac{\omega}{\rm keV}\right)^2 \left(\frac{B}{10\,{\rm Gauss}}\right)^2 \simeq 7.4 \times 10^5 \left(\frac{n_e}{10^4\,{\rm cm}^{-3}}\right), \tag{4.14}$$

which determines the resonance frequency. Here, we assumed $\Delta_{\rm vac} \gg \Delta_a$, i.e,

$$\left(\frac{\omega}{\rm keV}\right)^2 \left(\frac{B}{10\,{\rm Gauss}}\right)^2 \gg 5.4 \times 10^4 \left(\frac{m_a}{10^{-9}\,{\rm eV}}\right)^2. \tag{4.15}$$

4.1.3 Conversion Probability in the ω-n_e Plane

In the above subsection, we have established the relations between the parameters for efficient conversion to occur. Let us attempt to visualize the conversion probability in the parameter space to provide an overview of its behavior. For this purpose, we set the axion-photon coupling to $g_{a\gamma} = 10^{-11}$ GeV^{-1}, which approximately aligns with the current experimental upper limit. Utilizing information from the Event Horizon Telescope observations, we know the electron number density $n_e \sim 10^4$–10^7 cm^{-3} and the magnetic field $B \sim 1$–30 Gauss near M87* [62]. Consequently, we consider n_e within that range and use $B = 30$ Gauss as a reference value.

The conversion probability (4.2) excluding the z-dependent oscillation factor, i.e., $[\Delta_{\rm M}/(\Delta_{\rm osc}/2)]^2$, is depicted in the ω-n_e plane for axion masses $m_a = 10^{-7}, 10^{-8}, 10^{-9}$ eV in Figure 4.1. In each panel, the region where the maximum conversion probability can approach unity is represented in white.

In Figure 4.1, a white line extends horizontally toward the low ω region in each panel, corresponding to case (i) where $\Delta_{\rm pl} \simeq \Delta_a$. Additionally, a white band extends but becomes narrower toward the upper-right, connecting to the line corresponding to resonance (ii) with $\Delta_{\rm pl} \simeq \Delta_{\rm vac}$.

First, let us see the case $m_a = 10^{-7}$ eV shown in the top-left panel in Figure 4.1. Above the horizontal white line at $n_e = 7.3 \times 10^6$ cm^{-3}, Eq. (4.10) determines the lower bound of the photon energy ω for efficient conversion. Below that line, Eq. (4.9) gives the lower bound. The upper bound of ω for efficient conversion is given by Eq. (4.11). The white region almost lies in $\omega \sim 10^6$–10^7 eV. For photons around these energies, electron-positron pair creations would become relevant, introducing subtleties to the discussion of axion-photon conversion. If the axion mass is heavier than 10^{-7} eV, the window of the efficient conversion (white region) becomes narrower in the ω direction, and eventually closes except for the resonance lines due to cases (i) and (ii). This is because the conditions for efficient conversion given by the inequalities (4.9)–(4.11) are hardly satisfied at the same time.

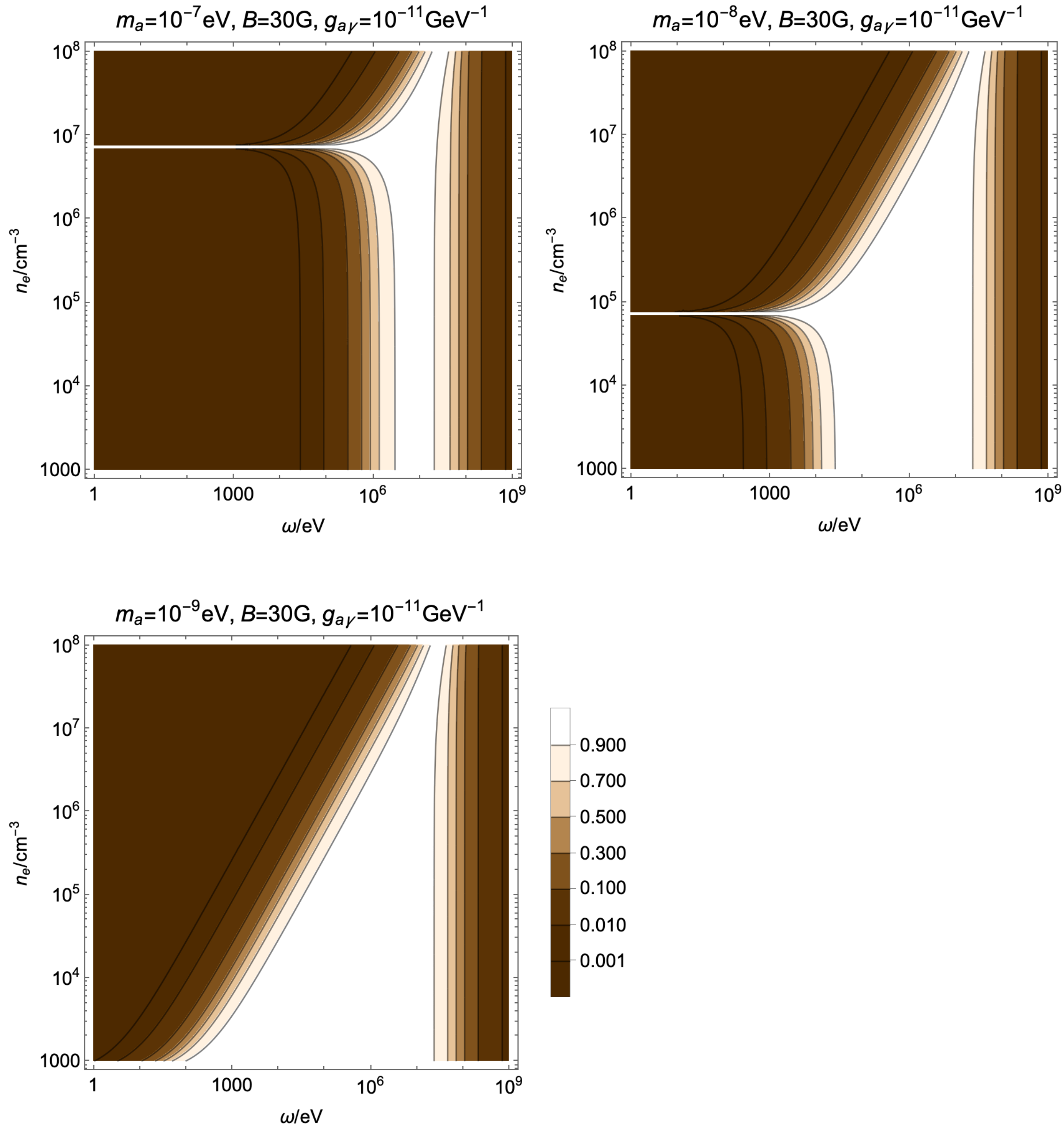

Figure 4.1. Conversion probability omitting the distance-dependent oscillation factor, $[\Delta_{\rm M}/(\Delta_{\rm osc}/2)]^2$, is shown in the ω-n_e plane, where ω is the photon energy and n_e is the electron number density. In each panel, a white area signifies that the factor exceeds 0.9. We set the magnetic field and axion-photon coupling as $B = 30$ Gauss and $g_{a\gamma} = 10^{-11}$ GeV^{-1}, respectively. The axion mass is chosen as $m_a = 10^{-7}, 10^{-8}$, and 10^{-9} eV in the upper-left, upper-right, and lower-left, respectively.

In the case of a smaller axion mass, $m_a = 10^{-8}$ eV, the effect of Δ_a proportional to m_a^2 becomes smaller, and hence, the white line corresponding to case (i) moves toward the smaller n_e as we see in the top-right panel in Figure 4.1. The plasma effect represented by Eq. (4.10) determines the lower bound of ω for efficient conversion in a broad parameter region. Below the resonance line, Eq. (4.9) gives the lower bound. The upper bound of ω for efficient conversion is again given by Eq. (4.11).

For an even smaller axion mass, $m_a = 10^{-9}$ eV, the plasma effect $\Delta_{\rm pl}$ dominates over the axion mass effect Δ_a across the entire range with $n_e \gtrsim 10^3$ cm^{-3}. Consequently, as evident in the bottom-left panel of Figure 4.1, Eq. (4.10) exclusively establishes the lower bound for ω in this region. The upper bound for efficient conversion remains determined by Eq. (4.11).

In our estimations so far, we have treated the plasma density and magnetic field as constant and uniform. However, realistic astrophysical scenarios involve fluctuations in these parameters. Noting that the parameter region satisfying the above specific case (i) or (ii) is quite narrow, the efficient conversion in those cases would be difficult in practice. Conversely, as depicted in Figure 4.1, a broad white region is evident for $m_a \lesssim 10^{-8}$ eV. This suggests that conversion can still occur in the presence of inhomogeneous plasma and magnetic fields, leveraging the extensive nature of this region. Thus, in the subsequent discussion, we will concentrate on the conversion within this broad white region.

4.2 Black Hole Photon Ring Dimming

We have seen that the prefactor in the conversion probability (4.2), i.e., $[\Delta_{\rm M}/(\Delta_{\rm osc}/2)]^2$, approaches unity in the white parameter region in Figure 4.1. Within this parameter region, photons traveling a distance of $\Delta_{\rm osc}^{-1}$ can be efficiently converted into axions, as the distance-dependent oscillating factor (the $\sin^2$ term) can also be close to unity. The length scale $\Delta_{\rm osc}^{-1}$ is typically as long as or longer than the Schwarzschild radius of supermassive black holes, such as M87*. Therefore, for photons propagating radially from a black hole, a strong magnetic field must be sustained over the distance $\Delta_{\rm osc}^{-1}$ for conversion to take place. On the other hand, as outlined in Section 3.2, a black hole spacetime features a photon sphere, consisting of unstable circular orbits for photons (or relativistic particles in general). Considering photons orbiting around the photon sphere, the maintenance of the magnetic field during propagation is automatically ensured, as they remain at a nearly constant radius. This observation implies that efficient conversion from photons to axions occurs around the photon sphere.

For simplicity, we take the Schwarzschild black hole. The metric reads

$$ds^2 = -f(r)dt^2 + \frac{1}{f(r)}dr^2 + r^2(d\theta^2 + \sin^2\theta\, d\phi^2)\,, \tag{4.16}$$

where

$$f(r) = 1 - \frac{2M}{r} \tag{4.17}$$

with M being the mass of the black hole. (Note that we set the speed of light c and the Newton constant G to be unity. Then, the black hole mass M has the dimension of length.) In this case, as discussed in Section 3.2, the photon sphere of the black hole is situated at the radius $r = 3M$. To characterize the motion of a particle, it is convenient to define the impact parameter b as $b \equiv L/E$, where L represents the conserved angular momentum along the geodesic, and E is the conserved energy (see Eq. (3.68)). As demonstrated in Section 3.2, photons with the critical impact parameter $b_{\rm crit} \equiv 3\sqrt{3}M$ can continuously orbit the photon sphere unless subjected to perturbations. For photons emitted from a source located far outside the black hole, with an impact parameter b slightly exceeding the critical value $b_{\rm crit}$, the trajectories will initially approach the photon sphere, linger around it for a certain duration, and ultimately escape from the sphere. We observe the surviving photons that have avoided conversion.

What proportion of photons will eventually be converted into axions? To estimate this fraction, let $d^3N/dt\, d\omega_{\rm c}\, db$ be the number of photons approaching the photon sphere with impact parameter b close to $b_{\rm crit}$, per unit time t, unit frequency $\omega_{\rm c}$, and unit impact parameter b. Here, the subscript "c" of $\omega_{\rm c}$ reminds us that it is measured in a local inertial frame at the photon sphere. The photons with impact parameter b close to $b_{\rm crit}$ stay orbiting in a region near the photon sphere, $3M < r \lesssim (3+\epsilon)M$ with a small constant $\epsilon (> 0)$. The time spent in that region is given by

$$T(b) = -3\sqrt{3}M \ln\left|\frac{2(b - b_{\rm crit})}{\sqrt{3}\,\epsilon^2\, M}\right| \tag{4.18}$$

as shown in Eq. (3.91). Note that the time $T(b)$ measured in the Schwarzschild coordinate t corresponds to the proper time for the observer at infinity. As evident from the local orthonormal frame introduced in Eqs. (3.16)–(3.19), a local observer situated at the radius $r = 3M$ experiences the proper time $\sqrt{f(3M)}\, T(b)$ during the Schwarzschild time period $T(b)$ (ignoring small deviations in the radius, including ϵ). In terms of proper distance, such photons travel for $z \simeq \sqrt{f(3M)}\, T(b) = T(b)/\sqrt{3}$. Therefore, the number of photons converted into axions in that region per unit time

t and unit frequency $\omega_{\rm c}$ is given by

$$\frac{d^2N_{\gamma\to a}}{dtd\omega_{\rm c}} = \int_{b_{\rm crit}}^{b_{\rm crit}+\sqrt{3}\epsilon^2M/2} db\,\frac{1}{2}\cdot\frac{d^3N}{dtd\omega_{\rm c}db}\cdot P_{\gamma\to a}\left(\frac{T(b)}{\sqrt{3}}\right), \tag{4.19}$$

where, by inserting $z = T(b)/\sqrt{3}$ into Eq. (4.2),

$$P_{\gamma\to a}\left(\frac{T(b)}{\sqrt{3}}\right) = \left(\frac{\Delta_{\rm M}}{\Delta_{\rm osc}/2}\right)^2 \sin^2\left(-\frac{3M\Delta_{\rm osc}}{2}\ln\frac{2(b-b_{\rm crit})}{\sqrt{3}\,\epsilon^2M}\right). \tag{4.20}$$

The factor $1/2$ in Eq. (4.19) comes from the fact that only photons with polarization parallel to the external magnetic field can undergo conversion into axions. Integrating over the interval $(b_{\rm crit}, b_{\rm crit}+\sqrt{3}\epsilon^2M/2)$ in Eq. (4.19), we can sum up photons that enter the region $3M < r \lesssim (3+\epsilon)M$ and subsequently escape to infinity. Note that $\Delta_{\rm osc}$ depends on the frequency of the photons $\omega_{\rm c}$, and B in $\Delta_{\rm M}$ and $\Delta_{\rm vac}$ represents a component of the magnetic field normal to the photon sphere.

Assuming that $d^3N/dt\,d\omega_{\rm c}\,db$ in the integrand of Eq. (4.19) does not vary significantly with respect to b, we can approximate it by the value at $b = b_{\rm crit}$ as an approximation. Then, Eq. (4.19) is reformulated as

$$\begin{aligned}
\frac{d^2N_{\gamma\to a}}{dtd\omega_{\rm c}} &\simeq \frac{1}{2}\left.\frac{d^3N}{dtd\omega_{\rm c}db}\right|_{b=b_{\rm crit}} \times \int_{b_{\rm crit}}^{b_{\rm crit}+\sqrt{3}\epsilon^2M/2} db\,P_{\gamma\to a}\left(\frac{T(b)}{\sqrt{3}}\right) \\
&= \frac{1}{2}\left.\frac{d^3N}{dtd\omega_{\rm c}db}\right|_{b=b_{\rm crit}} \times \left(\frac{\Delta_{\rm M}}{\Delta_{\rm osc}/2}\right)^2 \frac{\sqrt{3}\,\epsilon^2M}{4}\frac{(3M\Delta_{\rm osc})^2}{1+(3M\Delta_{\rm osc})^2}.
\end{aligned} \tag{4.21}$$

Consequently, the fraction of photons entering the region near the photon sphere that are converted into axions is given by

$$\frac{d^2N_{\gamma\to a}}{dtd\omega_{\rm c}}\bigg/\frac{d^2N}{dtd\omega_{\rm c}} \simeq \frac{1}{4}\left(\frac{\Delta_{\rm M}}{\Delta_{\rm osc}/2}\right)^2\frac{(3M\Delta_{\rm osc})^2}{1+(3M\Delta_{\rm osc})^2}, \tag{4.22}$$

which depends on the photon energy on the photon sphere $\omega_{\rm c}$. When observing the vicinity of a black hole, a bright image like a ring (known as the "photon ring") can be seen around a dark region (known as the "shadow"), which is created by photons traveling around the photon sphere. The analysis here indicates that we will observe a dimming of the photon ring at the fraction (4.22) due to axion-photon conversion.

The above calculation relies on the assumption that photons propagate without scattering by the surrounding plasma. This assumption holds when the mean free path of photons is significantly longer than the radius of the photon sphere, which is $3M$. Taking into account the finite mean free path of photons, the expression for the number of photons converted into axions per unit time and unit frequency

(4.19) should be modified as

$$\frac{d^2 N_{\gamma\to a}}{dt d\omega_{\rm c}} = \int db \, \frac{1}{2} \cdot \frac{d^3 N}{dt d\omega_{\rm c} db} \cdot P_{\gamma\to a}\left(\frac{T(b)}{\sqrt{3}}\right) \cdot \exp\left(-\frac{T(b)}{\sqrt{3}}\frac{1}{\ell}\right) \tag{4.23}$$

where $T(b)$ is given by Eq. (3.91), $P_{\gamma\to a}$ is given by Eq. (4.20), and ℓ is the mean free path of photons. As in Eq. (4.21), let us replace $d^3N/dt\, d\omega_{\rm c}\, db$ in the integrand by the value at $b = b_{\rm crit}$ for approximation. Then, we can perform the integration over $b \in (b_{\rm crit}, b_{\rm crit} + \sqrt{3}\epsilon^2 M/2)$ as

$$\begin{aligned}\frac{d^2 N_{\gamma\to a}}{dt d\omega_{\rm c}} \simeq \frac{1}{2} \left.\frac{d^3 N}{dt d\omega_{\rm c} db}\right|_{b=b_{\rm crit}} &\times \left(\frac{\Delta_{\rm M}}{\Delta_{\rm osc}/2}\right)^2 \frac{\sqrt{3}\,\epsilon^2\, M}{4} \frac{1}{1+(3M/\ell)} \\ &\times \frac{(3M\Delta_{\rm osc})^2}{(1+(3M/\ell))^2 + (3M\Delta_{\rm osc})^2} \, .\end{aligned} \tag{4.24}$$

It is evident that the result in Eq. (4.21) is reproduced when $3M/\ell \ll 1$. For photons with an energy below the electron mass, the mean free path is given by

$$\ell = \frac{1}{\sigma_{\rm T} n_e} = 1.5 \times 10^{24}\ {\rm cm}\left(\frac{{\rm cm}^{-3}}{n_e}\right) , \tag{4.25}$$

where $\sigma_{\rm T} = 8\pi\alpha^2/(3m_e^2) = 0.67 \times 10^{-24}\ {\rm cm}^2$ is the Thomson cross section, and n_e is the electron density. For the black holes considered in this thesis, with $n_e \sim 10^4$–$10^7\,{\rm cm}^{-3}$ and $M \sim 10^9 M_\odot (\sim 10^{14}\,{\rm cm})$, the condition $3M/\ell \ll 1$ is satisfied. Thus, the formula (4.21) neglecting the finite mean free path ℓ is applicable.

As a notable example, let us focus on the case of the efficient conversion satisfying $\Delta_{\rm osc}/2 \simeq \Delta_{\rm M}$ studied in Section 4.1.2. In this case, the fraction of photons converted into axions is given by

$$\frac{d^2 N_{\gamma\to a}}{dt d\omega_{\rm c}} \bigg/ \frac{d^2 N}{dt d\omega_{\rm c}} \simeq \frac{1}{4} \times \frac{(6M\Delta_{\rm M})^2}{1+(6M\Delta_{\rm M})^2} \, , \qquad \text{when} \ \ \Delta_{\rm osc}/2 \simeq \Delta_{\rm M} \, . \tag{4.26}$$

The key parameter, $6M\Delta_{\rm M} = 3M/(2\Delta_{\rm M})^{-1}$, represents the ratio of the photon sphere radius, $3M$, to the conversion length, $\Delta_{\rm osc}^{-1} \simeq (2\Delta_{\rm M})^{-1}$. It can be expressed as

$$6M\Delta_{\rm M} = 4.4 \times 10^{-3} \left(\frac{M}{10^9 M_\odot}\right)\left(\frac{B}{\rm Gauss}\right)\left(\frac{g_{a\gamma}}{10^{-11}\ {\rm GeV}^{-1}}\right) . \tag{4.27}$$

If this value significantly exceeds unity, the extent of the dimming of a photon ring approaches 25%. This is due to the fact that only photons with polarization parallel to the magnetic field undergo conversion, and an equal number of photons with that polarization are produced as axions, owing to substantial mixing. On the

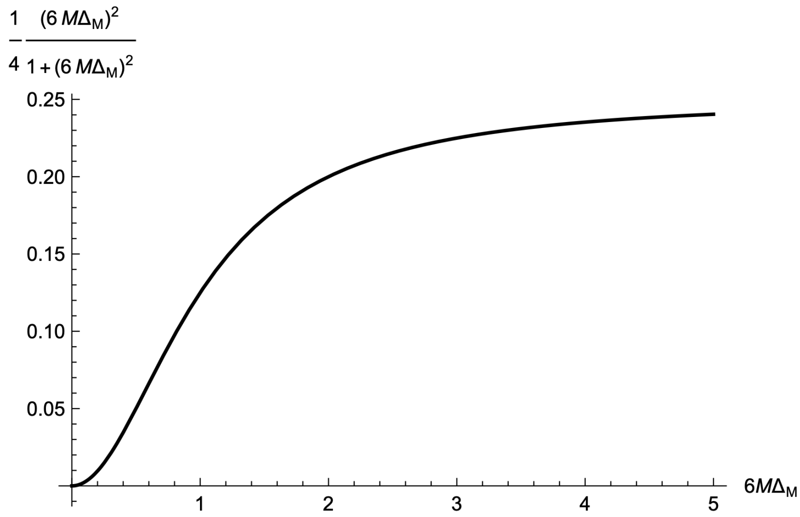

Figure 4.2. The dimming rate of a photon ring due to axion-photon conversion (in other words, the fraction of photons converted into axions) at the efficient case satisfying $\Delta_{\rm osc} \simeq 2\Delta_{\rm M}$ is plotted.

other hand, if $(6M\Delta_{\rm M})^2 \ll 1$, the extent of the dimming can be approximated as $(6M\Delta_{\rm M})^2 \times$ 25%. The extent of the dimming at efficient conversion as a function of $6M\Delta_{\rm M}$ is plotted in Figure 4.2.

Note that $6M\Delta_{\rm M}$ is proportional to the black hole mass M. Thus, supermassive black holes such as M87* are good candidates for substantial dimming of the photon sphere. In contrast, for stellar-mass black holes, it would be challenging to observe dimming unless strong magnetic fields are compensating for the effect of the small black hole masses.

Regarding the supermassive black hole at the center of the galaxy M87, the mass and magnetic field around $r \sim 5M$ are estimated as $M \simeq 6.2 \times 10^9 M_\odot$ [96] and $B \sim$ 1–30 Gauss [62], respectively. The current observational constraint on the axion-photon coupling is given by $g_{a\gamma} \lesssim 10^{-11}$–$10^{-10}$ GeV^{-1} for $m_a \lesssim 10^{-5}$ eV. Thus, let us take $M = 6.2 \times 10^9 M_\odot$, $B = 30$ Gauss, and $g_{a\gamma} = 10^{-11}$ GeV^{-1} as a trial. In this case, we find $6M\Delta_{\rm M} = 0.82$, resulting in a dimming of the photon ring given by

$$\frac{d^2 N_{\gamma\to a}}{dt d\omega_{\rm c}} \Big/ \frac{d^2 N}{dt d\omega_{\rm c}} \simeq 10\% \,, \quad \text{for} \;\; M = 6.2 \times 10^9 M_\odot \,, \;\; B = 30 \text{ Gauss} \,, \;\; g_{a\gamma} = 10^{-11} \text{ GeV}^{-1} \,. \tag{4.28}$$

This result is valid for photon energies within the region satisfying the condition for efficient conversion $\Delta_{\rm osc}/2 \simeq \Delta_{\rm M}$, represented by the white region in Figure 4.1.

4.3 Spectra of Photons and Axions

The energy spectrum of axions produced by axion-photon conversion near a photon sphere can be calculated based on the formula (4.19). Consequently, the energy spectrum of photons, taking into account the dimming effect, can be derived by subtracting the produced axion spectrum from the original photon spectrum.

Of course, to predict the concrete shape of the spectra, we must determine the number of photons entering a region near the photon sphere for each frequency, i.e., the integrand of Eq. (4.19). Therefore, it is imperative to identify the source of such photons. In the following, we employ the simplest model of the photon source to draw expected spectra and to discuss the possibility of detecting traces of axions.

4.3.1 Spherical Gas Model

For astrophysical black holes, the source of photons is believed to be the surrounding gas. In realistic situations, however, the gas configuration can be complex, making precise spectral calculations challenging. Instead, for simplicity, we assume that the gas emitting photons is distributed in a spherical region centered at the black hole. This straightforward assumption allows us to calculate spectra without relying on numerical simulations. Moreover, the low radiative efficiency observed for supermassive black holes like M87* and Sgr A* suggests that their radiating region is not a simple disk but rather a geometrically thick, hot accretion flow (see, e.g., Ref. [112]). Thus, we expect that our results based on the spherical gas model will provide a rough order-of-magnitude estimation for the spectra.

Let us consider a spherical region centered around a black hole where photons are emitted isotropically from each point with a specific emission rate. We aim to estimate how many of these emitted photons can approach the photon sphere of the black hole. For simplicity, in this model, we assume Schwarzschild spacetime geometry, neglecting the rotation of the black hole. The metric for this case is given by Eq. (4.16).

We start by considering an infinitesimal volume $dV_{\rm e}$ at a point $p_{\rm e}$ located at the radial coordinate $r_{\rm e}$. Let us write the number of photons within a frequency (or energy) interval $d\omega_{\rm e}$ emitted from $dV_{\rm e}$ and passing through an infinitesimal solid angle $d\Omega_{\rm e}$ viewed from the emission point $p_{\rm e}$ per unit time $\tau_{\rm e}$ as[*1]

$$d^6\left(\frac{dN}{d\tau_{\rm e}}\right) = J_{\rm e}^{(N)}(\omega_{\rm e}, r_{\rm e})\, d\Omega_{\rm e}\, dV_{\rm e}\, d\omega_{\rm e}\,. \tag{4.29}$$

[*1] In Eq. (4.29), "d^6" on the left-hand side stands for the dimension of the infinitesimal volume on the right-hand side. Here, we treat $d\Omega_{\rm e}$ and $dV_{\rm e}$ as two- and three-dimensional infinitesimal volume elements, respectively.

Here, the frequency $\omega_{\rm e}$, time $\tau_{\rm e}$, solid angle $\Omega_{\rm e}$, and volume $V_{\rm e}$ are measured in a local inertial frame at the point $p_{\rm e}$. In this frame, with the origin at $p_{\rm e}$, $\Theta_{\rm e}$ denotes the zenith angle measured from the direction to the black hole (see Figure 3.1), and $\Phi_{\rm e}$ denotes the azimuth angle in the plane normal to the direction to the black hole. We assume isotropic emission from a point $p_{\rm e}$, implying that $J_{\rm e}^{(N)}$ does not depend on the angles $\Theta_{\rm e}$ and $\Phi_{\rm e}$.

It is convenient to rewrite Eq. (4.29) in terms of the impact parameter of a photon b. For this purpose, we can use Eq. (3.69), and $db = (r_{\rm e}/\sqrt{f(r_{\rm e})})\cos\Theta_{\rm e} d\Theta_{\rm e}$ which follows from Eq. (3.69) for a fixed $r_{\rm e}$. Using these relations, and integrating Eq. (4.29) over the azimuth angle $\Phi_{\rm e}$, we obtain the number of photons emitted toward the photon sphere per unit time as

$$d^5\left(\frac{dN}{d\tau_{\rm e}}\right) = \frac{1}{2}\times 2\pi J_{\rm e}^{(N)}(\omega_{\rm e}, r_{\rm e})\frac{\sqrt{f(r_{\rm e})}}{r_{\rm e}}\frac{b}{\sqrt{(r_{\rm e}^2/f(r_{\rm e})) - b^2}}\, db\, dV_{\rm e}\, d\omega_{\rm e}\,, \tag{4.30}$$

where we multiply a factor of $1/2$ taking into account that only photons with $0 \leq \Theta_{\rm e} \leq \pi/2$ can approach the photon sphere.

The time element $d\tau_{\rm e}$ and volume element $dV_{\rm e}$ in a local inertial frame at $p_{\rm e}$ are respectively given by $d\tau_{\rm e} = \sqrt{f(r_{\rm e})}\, dt$ and $dV_{\rm e} = (r_{\rm e}^2/\sqrt{f(r_{\rm e})})\sin\theta\, dr_{\rm e}\, d\theta\, d\phi$ in terms of the Schwarzschild coordinates. Integrating Eq. (4.30) over θ and ϕ yields the number of photons emitted from a spherical shell of width $dr_{\rm e}$ with impact parameter $(b, b+db)$ per unit Schwarzschild time t and unit frequency $\omega_{\rm e}$. The result is

$$d^2\left(\frac{d^2N}{dt d\omega_{\rm e}}\right) = 4\pi^2 J_{\rm e}^{(N)}(\omega_{\rm e}, r_{\rm e})\frac{b\, r_{\rm e}\sqrt{f(r_{\rm e})}}{\sqrt{(r_{\rm e}^2/f(r_{\rm e})) - b^2}}\, dr_{\rm e}\, db\,. \tag{4.31}$$

Note that $\omega_{\rm e}$ above is the photon frequency (or energy) in a local inertial frame at the emission point $p_{\rm e}$, which is expressed as

$$\begin{aligned}\omega_{\rm e} &= k^\mu \partial_\mu (e^0)|_{p_{\rm e}} \\ &= \frac{dt}{d\lambda}\sqrt{f(r)}\bigg|_{p_{\rm e}} \\ &= \frac{E}{\sqrt{f(r_{\rm e})}}\,, \end{aligned} \tag{4.32}$$

where $k^\mu = dx^\mu(\lambda)/d\lambda$ is the tangent vector of the geodesic of the photon with affine parameter λ, and e^0 is a unit basis one-form in the time direction. (The tetrad is introduced in Eq. (3.16).) In the last line, Eq. (3.33) is utilized. The frequency measured in a local inertial frame at the photon sphere located at $r = 3M$ is $\omega_{\rm c} = E/\sqrt{f(3M)} = \sqrt{3f(r_{\rm e})}\,\omega_{\rm e}$. Thus, the number of photons approaching the photon sphere per unit time t and unit frequency ω_c with impact parameter $(b, b+db)$ is given by

$$d\left(\frac{d^2N}{dtd\omega_c}\right) = \frac{4\pi^2}{\sqrt{3}}\int_{r_{\rm in}}^{r_{\rm out}} dr_{\rm e}\, J_{\rm e}^{(N)}\left(\frac{\omega_c}{\sqrt{3f(r_{\rm e})}}, r_{\rm e}\right) \times \frac{b\, r_{\rm e}}{\sqrt{(r_{\rm e}^2/f(r_{\rm e})) - b^2}}\, db\,, \qquad (4.33)$$

where we assumed that the emission region is a sphere with inner diameter $r_{\rm in}$ and outer diameter $r_{\rm out}$. Strictly speaking, the pericenter of a photon's trajectory depends on the impact parameter b as Eq. (3.89). Here, we approximate the radial coordinate of the trajectory as the value on the photon sphere, $r = 3M$, for all photons.

Since our interest lies in photons with impact parameters b close to $b_{\rm crit} = 3\sqrt{3}M$, we approximate Eq. (4.33) by setting it to the value at $b = b_{\rm crit}$, akin to the treatment in Eq. (4.21). Subsequently, the integration with respect to b over $(b_{\rm crit}, b_{\rm crit} + \sqrt{3}\epsilon^2 M/2)$, which corresponds to summing up all photons entering a region $3M < r \lesssim (3+\epsilon)M$, yields

$$\frac{d^2N}{dtd\omega_c} \simeq 2\pi^2\epsilon^2 M \int_{r_{\rm in}}^{r_{\rm out}} dr_{\rm e}\, J_{\rm e}^{(N)}\left(\frac{\omega_c}{\sqrt{3f(r_{\rm e})}}, r_{\rm e}\right) \times \frac{3\sqrt{3}Mr_{\rm e}}{\sqrt{(r_{\rm e}^2/f(r_{\rm e})) - 27M^2}}\,. \qquad (4.34)$$

Here, we assume that $r_{\rm in}$ is outside the photon sphere so that $r_{\rm in}^2/f(r_{\rm in}) > b^2$ holds for $b \in (b_{\rm crit}, b_{\rm crit} + \sqrt{3}\epsilon^2 M/2)$. By multiplying Eq. (4.34) by an energy ω_c, we obtain the *original* photon spectral luminosity, i.e., the spectral luminosity before incorporating dimming by axion-photon conversion, in the region $3M < r \lesssim (3+\epsilon)M$.

On the other hand, by substituting Eq. (4.33) into Eq. (4.21), we can express the number of photons converted into axions near the photon sphere per unit time and unit frequency as

$$\begin{aligned}\frac{d^2N_{\gamma\to a}}{dtd\omega_c} \simeq{}& \frac{\pi^2\epsilon^2 M}{2}\left(\frac{\Delta_{\rm M}}{\Delta_{\rm osc}/2}\right)^2 \frac{(3M\Delta_{\rm osc})^2}{1+(3M\Delta_{\rm osc})^2} \\ &\times \int_{r_{\rm in}}^{r_{\rm out}} dr_{\rm e}\, J_{\rm e}^{(N)}\left(\frac{\omega_c}{\sqrt{3f(r_{\rm e})}}, r_{\rm e}\right) \times \frac{3\sqrt{3}Mr_{\rm e}}{\sqrt{(r_{\rm e}^2/f(r_{\rm e})) - 27M^2}}\,. \qquad (4.35)\end{aligned}$$

4.3.2 Thermal Bremsstrahlung

From Figure 4.1, where the parameters are taken from M87*, it is obvious that the energy of photons undergoing efficient conversion falls within the X ray range, $\omega \sim 10^3$–10^5 eV, and gamma ray range, $\omega \gtrsim 10^5$ eV. As discussed in Section 3.4.3, for supermassive black holes, the predominant process responsible for such high-frequency radiation is thermal bremsstrahlung of plasma [113]. The radiation energy from thermal bremsstrahlung, per unit time, unit frequency, and unit volume, is given by (see e.g., Sec. 5.2 in Ref. [95])

$$\frac{dE}{d\tau_{\rm e} d\omega_{\rm e} dV_{\rm e}} = \frac{2^4\alpha^3}{3m_e}\left(\frac{2\pi}{3m_e}\right)^{1/2} T_e^{-1/2}\, n_e^2\, e^{-\omega_{\rm e}/T_e}\, \bar{g}_{ff}\,, \tag{4.36}$$

where T_e is the electron temperature, n_e is the electron number density, and $\bar{g}_{ff}$ is a velocity-averaged Gaunt factor. Here, $\tau_{\rm e}$, $\omega_{\rm e}$, and $V_{\rm e}$ denote time, frequency, and volume in a local inertial frame at the emission point, respectively. We assumed that the ion density is equal to the electron density. Strictly speaking, the Gaunt factor $\bar{g}_{ff}$ depends on T_e and $\omega_{\rm e}$, but for the order-of-magnitude estimation, it can be regarded as approximately unity. Assuming isotropic radiation from each infinitesimal volume, $J_{\rm e}^{(N)}$ defined by Eq. (4.29) reads

$$J_{\rm e}^{(N)}(\omega_{\rm e}, r_{\rm e}) = \frac{4\alpha^3}{3\pi m_e}\left(\frac{2\pi}{3m_e}\right)^{1/2} \omega_{\rm e}^{-1}\, T_e^{-1/2}\, n_e^2\, e^{-\omega_{\rm e}/T_e}\, \bar{g}_{ff}\,. \tag{4.37}$$

Let us assume that the electron temperature and number density follow a power law with respect to the radial coordinate $r_{\rm e}$:

$$T_e = T_{e,{\rm c}}\left(\frac{r_{\rm e}}{3M}\right)^{-p_T}, \tag{4.38}$$

$$n_e = n_{e,{\rm c}}\left(\frac{r_{\rm e}}{3M}\right)^{-p_n}, \tag{4.39}$$

where $T_{e,{\rm c}}$ and $n_{e,{\rm c}}$ are the values at the photon sphere, and p_T and p_n are parameters. If the gas is heated to the virial temperature, $T_{\rm vir} = m_p M/(3r) \sim 10^{12}\ {\rm K}\ (r/(3M))^{-1}$ with m_p being the proton mass, we find $p_T = 1$. In theoretical models, T_e is treated as a sub-virial temperature due to cooling processes and inefficient coupling between electrons and ions [112]. In the case of spherical accretion, the mass accretion rate is written as $\dot{M} = 4\pi r^2 \rho v_r$ with mass density ρ and radial velocity v_r. Assuming a constant accretion rate $\dot{M}$ and free-falling gas $v_r \propto r^{-1/2}$, we obtain $p_n = 3/2$. Of course, some other factors (e.g., the presence of outflows) will modify these parameters. Nevertheless, a set of parameters $(p_T, p_n) = (1, 3/2)$ is a reasonable trial.

We can evaluate the integral with respect to $r_{\rm e}$ in Eq. (4.34) with Eqs. (4.37)–(4.39) in a straightforward manner under the following approximations. Given that the source of photons is well outside the photon sphere, the approximation $\sqrt{(r_{\rm e}^2/f(r_{\rm e})) - 27M^2} \sim r_{\rm e}$ holds for the integrand in Eq. (4.34), and $f(r_{\rm e})$ in the argument of $J_{\rm e}^{(N)}$ can be set to unity. The exponential factor $e^{-\omega_{\rm e}/T_{\rm e}}$ in Eq. (4.37) is also approximately unity under the condition

$$\frac{\omega_{\rm c}}{T_{e,{\rm c}}} \ll \sqrt{3}\left(\frac{3M}{r_{\rm e}}\right)^{p_T}. \tag{4.40}$$

We consider the photon energy $\omega_{\rm c}$ such that this inequality is satisfied in a region outside $r_{\rm in}$. Then, Eq. (4.34) reduces to[*2]

$$\begin{aligned}\frac{d^2N}{dtd\omega_{\rm c}} &\simeq 27\omega_{\rm c}^{-1}L_{\omega 0}\int_{r_{\rm in}}\frac{dr_{\rm e}}{3M}\left(\frac{r_{\rm e}}{3M}\right)^{-2p_n+(p_T/2)} \\ &\simeq \frac{27}{2p_n-(p_T/2)-1}\left(\frac{r_{\rm in}}{3M}\right)^{-2p_n+(p_T/2)+1}\omega_{\rm c}^{-1}L_{\omega 0}\,,\end{aligned}\tag{4.41}$$

where we defined

$$\begin{aligned}L_{\omega 0} &\equiv 2\pi^2\epsilon^2M^3\left(\frac{4\alpha^3}{3\pi m_e}\right)\left(\frac{2\pi}{3m_e}\right)^{1/2}T_{e,\rm c}^{-1/2}n_{e,\rm c}^2\bar{g}_{ff} \\ &= 1.7\times 10^{34}\,\epsilon^2\left(\frac{M}{10^9M_\odot}\right)^3\left(\frac{T_{e,\rm c}}{10^{11}\ \rm K}\right)^{-1/2} \\ &\quad\times\left(\frac{n_{e,\rm c}}{10^4\ \rm cm^{-3}}\right)^2\bar{g}_{ff}\ \rm keV\cdot sec^{-1}\cdot keV^{-1}.\end{aligned}\tag{4.42}$$

In the second line in Eq. (4.41), we picked up only the term of $r_{\rm in}$ by assuming $-2p_n+(p_T/2)+1<0$. In particular, setting $(p_T,p_n)=(1,3/2)$ and $r_{\rm in}=4M$, we obtain the original photon spectral luminosity near the photon sphere as $L_\omega = 11.7L_{\omega 0}$ for $\omega_{\rm c}\ll T_{e,\rm c}(3M/r_{\rm in})\simeq 9\ {\rm MeV}(T_{e,\rm c}/10^{11}\,{\rm K})(3M/r_{\rm in})$, which produces a flat spectrum at energies below the gamma ray range. On the other hand, for $\omega_{\rm c}\gtrsim 9\,{\rm MeV}(T_{e,\rm c}/10^{11}\,{\rm K})(3M/r_{\rm in})$, the spectrum is exponentially damped since there are few high-temperature electrons which emit such high-energy photons.

4.3.3 Observing Axions through Photon Ring Dimming

Inserting Eq. (4.37) with Eqs. (4.38) and (4.39) into Eq. (4.35), and multiplying the energy $\omega_{\rm c}$, we can derive the anticipated spectral luminosity of axions within the framework of thermal bremsstrahlung from a spherical gas model. Subsequently, the spectral luminosity of photons originating from a region near the photon sphere can be inferred by subtracting the generated axion luminosity from the original photon luminosity.

We anticipate that the axion-photon conversion will have an impact on the observed photon spectrum. However, since the conversion occurs effectively only near the photon sphere, we should note that only the spectrum near the photon sphere can be distorted. Therefore, to detect the spectral distortion, we need to resolve the near-horizon region. While the Event Horizon Telescope has successfully captured detailed images of the near-horizon structure in the radio band, comparable high-resolution observations are currently unavailable in the X ray and gamma ray

[*2]The upper limit of the integration interval is approximately given by a point where the inequality (4.40) saturates, but the final result of Eq. (4.41) depends only on the lower limit $r_{\rm in}$.

bands. In this situation, the total luminosity from the region outside the black hole will be relevant. When observing a black hole over a size $R(> r_{\rm in})$, we will collect the total luminosity as

$$\begin{aligned} L_{\rm tot} &= 4\pi \int_{r_{\rm in}}^{R} dr_{\rm e}\, r_{\rm e}^2 \, \frac{dE}{d\tau_{\rm e} d\omega_{\rm e} dV_{\rm e}} \\ &\sim \frac{6^3}{\epsilon^2} \frac{1}{3 - 2p_n + (p_T/2)} \left(\frac{R}{3M}\right)^{3-2p_n+(p_T/2)} L_{\omega 0}\,, \end{aligned} \tag{4.43}$$

where we used Eq. (4.36) with Eqs. (4.38) and (4.39), and picked up the contribution around $r_{\rm e} \sim R$. For instance, by setting $p_T = 1$, $p_n = 3/2$, and $\epsilon \sim 1$, we find $L_{\rm tot} \sim 4 \times 10^2\,(R/3M)^{1/2} L_{\omega 0}$. This indicates that the emission from the region outside the horizon will predominantly contribute to the total luminosity, leading to a negligible dimming effect due to the conversion. It is evident that the Chandra observatory, with an angular resolution of arcseconds, is inadequate to detect the dimming of M87* as it observes over a size $R \gg 3M$.

The situation can be significantly improved if the resolution size R becomes comparable to the horizon radius. In our simplified model, the photon sources are not distributed within $r_{\rm in}(> 3M)$. Therefore, when $R \lesssim 3M$, we can selectively collect photons approaching the photon sphere. In this scenario, the total luminosity is described by Eq. (4.34) (approximately Eq. (4.41)), and the observable spectral distortion is anticipated. The necessary angular resolution θ is determined by $R \lesssim 3M$ as

$$\theta = \frac{R}{D} \lesssim 10^{-5}\,\text{arcsec} \left(\frac{M}{10^{10} M_\odot}\right) \left(\frac{10\,\text{Mpc}}{D}\right), \tag{4.44}$$

where D denotes the distance to the black hole. Thus, in the case of M87* ($D = 16.8\,\text{Mpc}$, $M = 6.2 \times 10^9 M_\odot$), we need the angular resolution of $\theta \lesssim 10^{-5}\,\text{arcsec}$, even in the X ray and gamma ray bands.

We illustrate several examples of the anticipated energy spectra in Figure 4.3. In this representation, the horizontal axes denote the observed frequency $\omega_{\rm o}$, which is linked to the frequency at the photon sphere $\omega_{\rm c}$ as $\omega_{\rm o} = \omega_{\rm c}/\sqrt{3}$ due to gravitational redshift. We have disregarded other minor effects such as peculiar velocities and cosmic expansion. The vertical axes represent the spectral luminosity measured in units of $L_{\omega 0}$ as defined in Eq. (4.42). We assumed that the photons are produced by thermal bremsstrahlung of the gas distributed over a spherical region ($r_{\rm in} = 4M, r_{\rm out} = 10^3 M$) around the black hole. The gray curves are the original photon spectrum, i.e., the photon spectrum before incorporating the axion-photon conversion. The original photon spectrum exhibits a cutoff around $\omega_{\rm o} \sim T_{e,{\rm c}} \sim 10^7$ eV due to the exponential suppression factor in Eq. (4.36). The black curves depict the photon spectrum incorporating the conversion into axions in the vicinity of the photon sphere, while the red curves represent the resulting axion spectrum. The solid, dashed, and dotted curves correspond to axion masses m_a of 10^{-9}, 10^{-8}, and 10^{-7} eV, respectively. In both panels of Figure 4.3, we have chosen the parameters $M = 6.2 \times 10^9 M_\odot$, $T_{e,\mathrm{c}} = 10^{11}$ K, $p_T = 1$, $n_{e,\mathrm{c}} = 10^4$ cm^{-3}, and $p_n = 1.5$, all of which are adopted from M87*. The parameters in the upper panel are taken so that $(g_{a\gamma}/10^{-11}\,\mathrm{GeV}^{-1})(B/\mathrm{Gauss}) = 30$ as in Figure 4.1. On the other hand, those in the lower panel are taken so that $(g_{a\gamma}/10^{-11}\,\mathrm{GeV}^{-1})(B/\mathrm{Gauss}) = 300$, for which the conversion is more effective.

From Figure 4.3, we can see that the frequency range displaying dimming depends on the axion mass. This is because the lowest frequency of efficient conversion is determined by the axion mass as evident from Eq. (4.9). Besides, the extent of dimming at the efficient conversion is determined by $g_{a\gamma}$, B, and M as elucidated in Eqs. (4.26) and (4.27). In the upper panel, dimming of 10% can be seen, which is already mentioned in Eq. (4.28). In the lower panel, the dimming reaches approximately 25%, representing the maximum achievable value.

The above demonstration indicates an opportunity to determine (or impose constraints on) the axion mass m_a and axion-photon coupling $g_{a\gamma}$ through the observation of the photon spectrum in the vicinity of a photon sphere. Let us suppose that the mass of the black hole M, and the magnetic field B and the electron density n_e around the photon sphere are known. The spectral shape is characterized by two quantities: the magnitude of the dimming and the frequency range manifesting the dimming. First, when M and B are given, the maximum magnitude of the dimming can be translated to $g_{a\gamma}$ by using Eqs. (4.26) and (4.27). It is noteworthy that, regardless of the magnitude of $g_{a\gamma}$, the dimming saturates at 25%. Consequently, in situations where the dimming approaches approximately 25%, only the lower limit of $g_{a\gamma}$ can be inferred. Second, from Eqs. (4.9) and (4.10), the lowest frequency showing the efficient dimming depends on $g_{a\gamma}$, B, and the axion mass m_a or plasma frequency ω_{pl} (or, equivalently, the electron density n_e). In the case $m_a < \omega_{\mathrm{pl}}$, the lowest frequency is determined by n_e, $g_{a\gamma}$, and B as Eq. (4.10). Hence, it can also be used to read off the coupling $g_{a\gamma}$ from the dimming. In a more intriguing case $m_a > \omega_{\mathrm{pl}}$, the lowest frequency is determined by Eq. (4.9), involving m_a, $g_{a\gamma}$, and B. In this case, if B and $g_{a\gamma}$ are known, the lowest frequency can be utilized to determine m_a. Even if $g_{a\gamma}$ has not been determined, we can obtain the one-to-one relation between m_a and $g_{a\gamma}$ through the lowest frequency exhibiting dimming. Of course, if no dimming is observed, constraints on the axion mass m_a and axion-photon coupling $g_{a\gamma}$ can still be derived.

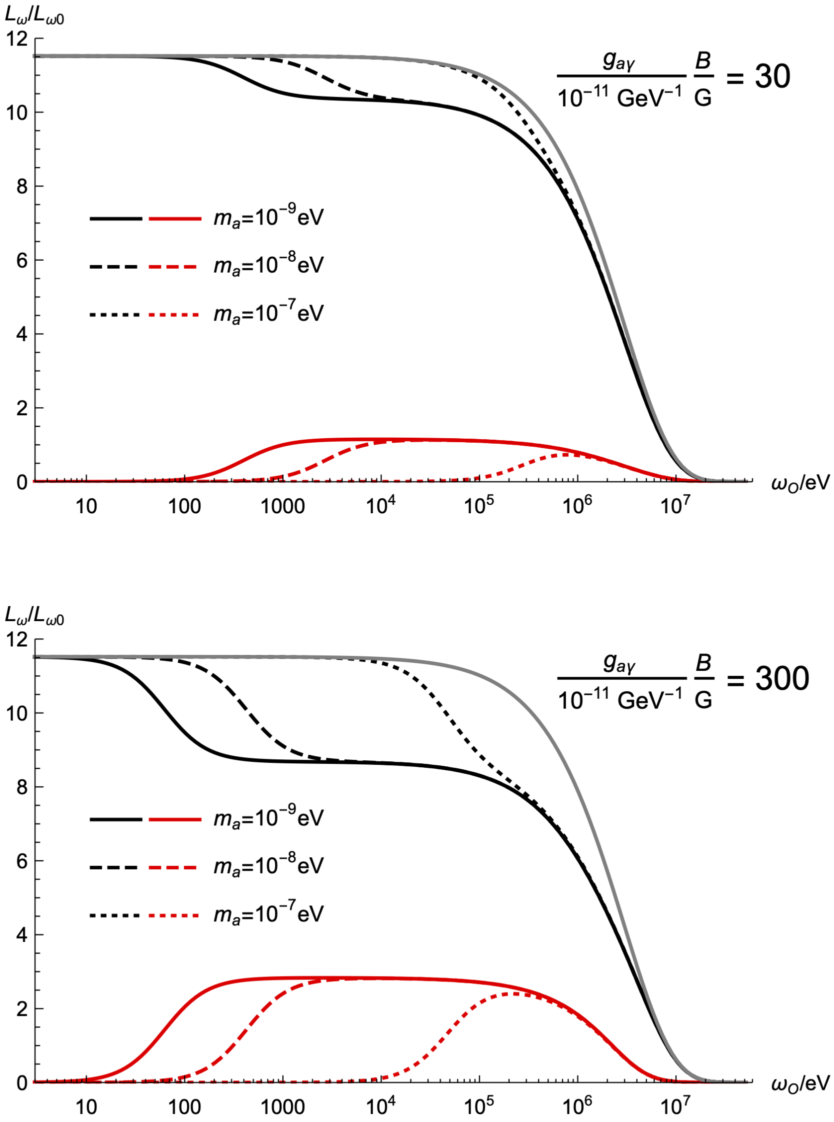

Figure 4.3. The expected spectral luminosities of photons and axions are depicted. The horizontal axes are the observed frequency ω_{o}. The vertical axes are the spectral luminosity L_ω normalized by $L_{\omega 0}$ defined in Eq. (4.42). The gray curves are the original photon spectral luminosity, assuming that the photons are initially produced by thermal bremsstrahlung of the gas distributed in a spherical region over $r \in (r_{\mathrm{in}} = 4M, r_{\mathrm{out}} = 10^3 M)$. The black curves are the photon spectral luminosity incorporating the conversion into axions. The red curves are the produced axion spectral luminosity. For the red and black curves, the solid, dashed, and dotted curves correspond to the axion masses $m_a = 10^{-9}$, 10^{-8}, and 10^{-7} eV, respectively. The upper panel is for $(g_{a\gamma}/10^{-11}\,\mathrm{GeV}^{-1})(B/\mathrm{Gauss}) = 30$, and the lower panel is for $(g_{a\gamma}/10^{-11}\,\mathrm{GeV}^{-1})(B/\mathrm{Gauss}) = 300$. In both panels, other parameters are chosen as follows: $M = 6.2 \times 10^9 M_\odot$, $T_{e,\mathrm{c}} = 10^{11}$ K, $p_T = 1$, $n_{e,\mathrm{c}} = 10^4$ cm^{-3}, and $p_n = 1.5$.

4.3.4 Approximate Formula of Axion Flux

By employing Eqs. (4.22) and (4.41), the spectral number flux of axions from a spherical region near the photon sphere with $3M < r < (3+\epsilon)M$ is approximately given by

$$\begin{aligned}
\frac{d\Phi_a}{d\omega_{\rm o}} &= \frac{1}{4\pi D^2}\frac{d^2N_{\gamma\to a}}{dtd\omega_{\rm o}} \\
&\simeq \frac{1}{4\pi D^2} \times \left[\frac{1}{4}\left(\frac{\Delta_{\rm M}}{\Delta_{\rm osc}/2}\right)^2 \frac{(3M\Delta_{\rm osc})^2}{1+(3M\Delta_{\rm osc})^2}\right] \\
&\quad\times \frac{27}{2p_n-(p_T/2)-1}\left(\frac{r_{\rm in}}{3M}\right)^{-2p_n+(p_T/2)+1} \omega_{\rm o}^{-1}L_{\omega 0} \\
&= 1.4\times 10^{-16}\epsilon^2 \left[\frac{1}{4}\left(\frac{\Delta_{\rm M}}{\Delta_{\rm osc}/2}\right)^2 \frac{(3M\Delta_{\rm osc})^2}{1+(3M\Delta_{\rm osc})^2}\right] \\
&\quad\times \frac{27}{2p_n-(p_T/2)-1}\left(\frac{r_{\rm in}}{3M}\right)^{-2p_n+(p_T/2)+1} \\
&\quad\times \left(\frac{\rm Mpc}{D}\right)^2 \left(\frac{M}{10^9 M_\odot}\right)^3 \left(\frac{T_{e,{\rm c}}}{10^{11}\ {\rm K}}\right)^{-1/2} \\
&\quad\times \left(\frac{n_{e,{\rm c}}}{10^4\ {\rm cm}^{-3}}\right)^2 \left(\frac{\rm keV}{\omega_{\rm o}}\right) \bar{g}_{ff}\ {\rm cm}^{-2}\cdot{\rm sec}^{-1}\cdot{\rm keV}^{-1},
\end{aligned} \tag{4.45}$$

for $\omega_{\rm o} \ll 9$ MeV$(T_{e,{\rm c}}/10^{11}\,{\rm K})(3M/r_{\rm in})$, where D represents the distance to the black hole from us. Specifically, by setting the parameters following M87* ($D = 16.8$ Mpc) as in the upper panel in Figure 4.3 and assuming the axion mass $m_a = 10^{-9}$ eV, the fraction of photons converted into axions [the square bracket in Eq. (4.45)] reaches 10% for keV $\lesssim \omega_{\rm o} \lesssim 10$ MeV. Then, with $\epsilon \sim \bar{g}_{ff} \sim 1$, we find the spectral axion number flux as $d\Phi_a/d\omega_{\rm o} \sim 1\times 10^{-16}{\rm cm}^{-2}\cdot{\rm sec}^{-1}\cdot{\rm keV}^{-1}$ for $\omega_{\rm o} \sim$ keV. For the black hole at the center of the Milky Way, Sgr A* ($D = 8$ kpc, $M = 4\times 10^6 M_\odot$ [106]), the distance D is three orders of magnitude closer than M87*, but the mass M is three orders of magnitude smaller. Consequently, it is challenging to anticipate an axion flux larger than that from M87*. It is noteworthy that the axion flux from a single black hole photon sphere is considerably smaller than that of solar axions (2.61).

Chapter 5

Conclusion and Prospects

If axions exist in nature, the conversion of photons into axions takes place when photons propagate in a magnetic field, governed by the coupling $\mathcal{L}_{\rm int} = -(g_{a\gamma}/4)\phi F_{\mu\nu}\widetilde{F}^{\mu\nu}$. Notably, there are many black holes in our universe and they are accompanied by a magnetosphere. In particular, sizable magnetic fields are anticipated around black holes in active galactic nuclei. In this thesis, we have investigated the axion-photon conversion phenomenon around black holes. For a magnetic field strength $B \sim 10^1$–10^2 Gauss and axion-photon coupling constant $g_{a\gamma} \sim 10^{-11}$ GeV^{-1}, the propagation length required for conversion has turned out to be comparable to the Schwarzschild radius of a supermassive black hole with mass $M \sim 10^9$–$10^{10} M_\odot$ as shown in Eq. (4.8). At first glance, it might seem that the magnetic field must be maintained over such a long conversion length in the radial direction for a substantial conversion to occur. However, photons can orbit around a photon sphere of a black hole for a certain period of time. Since such orbiting photons stay at a nearly constant radius, it is automatically ensured that the magnetic field is maintained during propagation. Consequently, it is expected that axion-photon conversion will efficiently occur near the photon sphere, which will affect the observation of the photon ring around the black hole shadow.

Supposing the axion-photon coupling constant $g_{a\gamma} \sim 10^{-11}$ GeV^{-1}, a magnetic field $B \sim 30$ Gauss and an electron number density $n_e \sim 10^4$–10^7 cm^{-3}, which are expected values near M87* [62], we have shown that the photons in the X ray and gamma ray bands can be efficiently converted into axions in the mass range $m_a \lesssim 10^{-7}$ eV (see Figure 4.1). This fact indicates that, when observing the vicinity of the black hole with electromagnetic waves, we will see a dimming of the photon ring in those wavelengths, provided a sufficiently high resolution is achieved in the future. We have shown that the maximum dimming rate of the photon ring is 25%. In the case of M87*, we found that the dimming rate can be around 10% if the angular resolution of the Event Horizon Telescope level (i.e., 10^{-5} arcsec precision) is achieved. In general, the magnitude of dimming depends on the axion-photon coupling $g_{a\gamma}$, the black hole mass M, and the magnetic field strength B as in Eqs. (4.26) and (4.27). We depicted the dependence in Figure 4.2. Provided M and B are known from other observations, we can determine the value of (or give a constraint on) $g_{a\gamma}$ from the photon ring dimming. The larger M, the greater the dimming, thus supermassive black holes such as M87* are good candidates for observing the photon ring dimming. Furthermore, the photon frequency range exhibiting the dimming has information on the axion mass. In the case that the axion mass m_a is smaller than the plasma frequency $\omega_{\rm pl}$, the lowest frequency of dimming is determined by Eq. (4.10) where $g_{a\gamma}$, n_e, and B appear. On the other hand, in the case of $m_a > \omega_{\rm pl}$, it is determined by Eq. (4.9) where $g_{a\gamma}$, m_a, and B appear. Hence, the lowest frequency of dimming can be used to measure $g_{a\gamma}$ and m_a. We have demonstrated photon ring dimming in Figure 4.3, where the photons are assumed to be sourced by thermal bremsstrahlung of gas spherically distributed around the black hole. Certainly, to observe the dimming of the photon ring, high-resolution observations of the near-horizon region are essential. Although the Event Horizon Telescope has successfully imaged this region in the radio band, such high-resolution observations have not yet been achieved in the X ray and gamma ray bands. The present study anticipates the future potential of multi-wavelength observations with higher resolution. As to this direction, high-resolution X ray interferometry is proposed e.g. in Ref. [114]. We anticipate that our findings will serve as motivation for future observations.

In this thesis, we simplified the treatment of the magnetic field and plasma density by considering them as homogeneous near the photon sphere. Intriguingly, Figure 4.1 illustrates that conversion takes place across a wide parameter range. Hence, we anticipate that conversion will persist even in more realistic scenarios involving inhomogeneous magnetic fields and varying plasma density.

There are several directions to be pursued beyond the scope of the current study. One is to incorporate the rotation of black holes. Notably, rotating black holes known as Kerr black holes exhibit circular photon orbits at two distinct radii on the equatorial plane. Due to varying gravitational redshifts experienced by photons emitted from these different radii, axion-photon conversion at these locations may induce dimming at different frequencies. Another important issue is to investigate how axion-photon conversion influences the polarization of light originating from the photon sphere. Additionally, it is worth investigating axion-photon conversion not only in the presence of a magnetic field but also in an axion background [115], which is not explored in this thesis. Indeed, axions may constitute dark matter [9, 13, 16, 17] or be generated through superradiance around black holes [73, 116]. Finally, we have estimated the axion flux from the photon sphere of a single black hole in Eq. (4.45), which turned out to be too tiny to be detected. However, our universe hosts a vast number of black holes. Notably, quasars are significantly brighter than low-luminosity active galactic nuclei such as M87*, and the resulting axion luminosity may be larger than that of M87*. The cumulative axion luminosity could potentially contribute to the cosmic axion background [117]. The exploration of these contributions remains an intriguing avenue for future investigations.

Acknowledgments

I express my gratitude to my supervisor, Jiro Soda, for his unwavering encouragement and fruitful discussions throughout this research endeavor. Additionally, I extend my thanks to Toshifumi Noumi for his valuable suggestions. I am sincerely appreciative of all the individuals I have encountered during my time at Kobe University.

The author acknowledges support from the Grant-in-Aid for JSPS Research Fellowship and JSPS KAKENHI Grant No. JP21J20600.

Bibliography

[1] R. D. Peccei and H. R. Quinn. “CP Conservation in the Presence of Instantons”. In: *Phys. Rev. Lett.* 38 (1977), pp. 1440–1443.

[2] S. Weinberg. “A New Light Boson?” In: *Phys. Rev. Lett.* 40 (1978), pp. 223–226.

[3] F. Wilczek. “Problem of Strong P and T Invariance in the Presence of Instantons”. In: *Phys. Rev. Lett.* 40 (1978), pp. 279–282.

[4] J. E. Kim. “Weak Interaction Singlet and Strong CP Invariance”. In: *Phys. Rev. Lett.* 43 (1979), p. 103.

[5] M. A. Shifman, A. I. Vainshtein, and V. I. Zakharov. “Can Confinement Ensure Natural CP Invariance of Strong Interactions?” In: *Nucl. Phys. B* 166 (1980), pp. 493–506.

[6] M. Dine, W. Fischler, and M. Srednicki. “A Simple Solution to the Strong CP Problem with a Harmless Axion”. In: *Phys. Lett. B* 104 (1981), pp. 199–202.

[7] A. R. Zhitnitsky. “On Possible Suppression of the Axion Hadron Interactions. (In Russian)”. In: *Sov. J. Nucl. Phys.* 31 (1980), p. 260.

[8] P. Svrcek and E. Witten. “Axions In String Theory”. In: *JHEP* 06 (2006), p. 051. arXiv: hep-th/0605206.

[9] D. J. E. Marsh. “Axion Cosmology”. In: *Phys. Rept.* 643 (2016), pp. 1–79. arXiv: 1510.07633 [astro-ph.CO].

[10] K. Freese, J. A. Frieman, and A. V. Olinto. “Natural inflation with pseudo - Nambu-Goldstone bosons”. In: *Phys. Rev. Lett.* 65 (1990), pp. 3233–3236.

[11] J. E. Kim, H. P. Nilles, and M. Peloso. “Completing natural inflation”. In: *JCAP* 01 (2005), p. 005. arXiv: hep-ph/0409138.

[12] S. Dimopoulos et al. “N-flation”. In: *JCAP* 08 (2008), p. 003. arXiv: hep-th/0507205.

[13] J. Preskill, M. B. Wise, and F. Wilczek. “Cosmology of the Invisible Axion”. In: *Phys. Lett. B* 120 (1983). Ed. by M. A. Srednicki, pp. 127–132.

[14] L. F. Abbott and P. Sikivie. “A Cosmological Bound on the Invisible Axion”. In: *Phys. Lett. B* 120 (1983). Ed. by M. A. Srednicki, pp. 133–136.

[15] M. Dine and W. Fischler. “The Not So Harmless Axion”. In: *Phys. Lett. B* 120 (1983). Ed. by M. A. Srednicki, pp. 137–141.

[16] L. Hui et al. “Ultralight scalars as cosmological dark matter”. In: *Phys. Rev. D* 95.4 (2017), p. 043541. arXiv: 1610.08297 [astro-ph.CO].

[17] F. Chadha-Day, J. Ellis, and D. J. E. Marsh. “Axion dark matter: What is it and why now?” In: *Sci. Adv.* 8.8 (2022), abj3618. arXiv: 2105.01406 [hep-ph].

[18] J. A. Frieman et al. “Cosmology with ultralight pseudo Nambu-Goldstone bosons”. In: *Phys. Rev. Lett.* 75 (1995), pp. 2077–2080. arXiv: astro-ph/9505060.

[19] R. R. Caldwell, R. Dave, and P. J. Steinhardt. “Cosmological imprint of an energy component with general equation of state”. In: *Phys. Rev. Lett.* 80 (1998), pp. 1582–1585. arXiv: astro-ph/9708069.

[20] I. Zlatev, L.-M. Wang, and P. J. Steinhardt. “Quintessence, cosmic coincidence, and the cosmological constant”. In: *Phys. Rev. Lett.* 82 (1999), pp. 896–899. arXiv: astro-ph/9807002.

[21] K. Choi. “String or M theory axion as a quintessence”. In: *Phys. Rev. D* 62 (2000), p. 043509. arXiv: hep-ph/9902292.

[22] E. J. Copeland, M. Sami, and S. Tsujikawa. “Dynamics of dark energy”. In: *Int. J. Mod. Phys. D* 15 (2006), pp. 1753–1936. arXiv: hep-th/0603057.

[23] L. Maiani, R. Petronzio, and E. Zavattini. “Effects of Nearly Massless, Spin Zero Particles on Light Propagation in a Magnetic Field”. In: *Phys. Lett. B* 175 (1986), pp. 359–363.

[24] G. Raffelt and L. Stodolsky. “Mixing of the Photon with Low Mass Particles”. In: *Phys. Rev. D* 37 (1988), p. 1237.

[25] P. Sikivie. “Experimental Tests of the Invisible Axion”. In: *Phys. Rev. Lett.* 51 (1983). Ed. by M. A. Srednicki. [Erratum: Phys.Rev.Lett. 52, 695 (1984)], pp. 1415–1417.

[26] I. G. Irastorza and J. Redondo. “New experimental approaches in the search for axion-like particles”. In: *Prog. Part. Nucl. Phys.* 102 (2018), pp. 89–159. arXiv: 1801.08127 [hep-ph].

[27] V. Anastassopoulos et al. “New CAST Limit on the Axion-Photon Interaction”. In: *Nature Phys.* 13 (2017), pp. 584–590. arXiv: 1705.02290 [hep-ex].

[28] E. Armengaud et al. “Conceptual Design of the International Axion Observatory (IAXO)”. In: *JINST* 9 (2014), T05002. arXiv: 1401.3233 [physics.ins-det].

[29] S. J. Asztalos et al. "A SQUID-based microwave cavity search for dark-matter axions". In: *Phys. Rev. Lett.* 104 (2010), p. 041301. arXiv: 0910.5914 [astro-ph.CO].

[30] A. De Angelis, M. Roncadelli, and O. Mansutti. "Evidence for a new light spin-zero boson from cosmological gamma-ray propagation?" In: *Phys. Rev. D* 76 (2007), p. 121301. arXiv: 0707.4312 [astro-ph].

[31] M. Simet, D. Hooper, and P. D. Serpico. "The Milky Way as a Kiloparsec-Scale Axionscope". In: *Phys. Rev. D* 77 (2008), p. 063001. arXiv: 0712.2825 [astro-ph].

[32] M. A. Sanchez-Conde et al. "Hints of the existence of Axion-Like-Particles from the gamma-ray spectra of cosmological sources". In: *Phys. Rev. D* 79 (2009), p. 123511. arXiv: 0905.3270 [astro-ph.CO].

[33] A. Mirizzi and D. Montanino. "Stochastic conversions of TeV photons into axion-like particles in extragalactic magnetic fields". In: *JCAP* 12 (2009), p. 004. arXiv: 0911.0015 [astro-ph.HE].

[34] M. Meyer, D. Horns, and M. Raue. "First lower limits on the photon-axion-like particle coupling from very high energy gamma-ray observations". In: *Phys. Rev. D* 87.3 (2013), p. 035027. arXiv: 1302.1208 [astro-ph.HE].

[35] K. Kohri and H. Kodama. "Axion-Like Particles and Recent Observations of the Cosmic Infrared Background Radiation". In: *Phys. Rev. D* 96.5 (2017), p. 051701. arXiv: 1704.05189 [hep-ph].

[36] G. Zhang and B.-Q. Ma. "Axion-photon conversion of LHAASO multi-TeV and PeV photons". In: (Oct. 2022). arXiv: 2210.13120 [hep-ph].

[37] G. Galanti, M. Roncadelli, and F. Tavecchio. "Explanation of the very-high-energy emission from GRB221009A". In: (Oct. 2022). arXiv: 2210.05659 [astro-ph.HE].

[38] S. V. Troitsky. "Parameters of axion-like particles required to explain high-energy photons from GRB 221009A". In: (Oct. 2022). arXiv: 2210.09250 [astro-ph.HE].

[39] A. Baktash, D. Horns, and M. Meyer. "Interpretation of multi-TeV photons from GRB221009A". In: (Oct. 2022). arXiv: 2210.07172 [astro-ph.HE].

[40] W. Lin and T. T. Yanagida. "Electroweak axion in light of GRB221009A". In: (Oct. 2022). arXiv: 2210.08841 [hep-ph].

[41] M. M. Gonzalez et al. "GRB 221009A: A light dark matter burst or an extremely bright Inverse Compton component?" In: (Oct. 2022). arXiv: 2210.15857 [astro-ph.HE].

[42] S. Nakagawa et al. “Axion dark matter from first-order phase transition, and very high energy photons from GRB 221009A”. In: (Oct. 2022). arXiv: 2210.10022 [hep-ph].

[43] P. Carenza and M. C. D. Marsh. “On ALP scenarios and GRB 221009A”. In: (Nov. 2022). arXiv: 2211.02010 [astro-ph.HE].

[44] G. Galanti, M. Roncadelli, and F. Tavecchio. “Assessment of ALP scenarios for GRB 221009A”. In: (Nov. 2022). arXiv: 2211.06935 [astro-ph.HE].

[45] T. Yanagida and M. Yoshimura. “Resonant Axion - Photon Conversion in the Early Universe”. In: *Phys. Lett. B* 202 (1988), pp. 301–306.

[46] A. Mirizzi, J. Redondo, and G. Sigl. “Constraining resonant photon-axion conversions in the Early Universe”. In: *JCAP* 08 (2009), p. 001. arXiv: 0905.4865 [hep-ph].

[47] H. Tashiro, J. Silk, and D. J. E. Marsh. “Constraints on primordial magnetic fields from CMB distortions in the axiverse”. In: *Phys. Rev. D* 88.12 (2013), p. 125024. arXiv: 1308.0314 [astro-ph.CO].

[48] D. Hooper and P. D. Serpico. “Detecting Axion-Like Particles With Gamma Ray Telescopes”. In: *Phys. Rev. Lett.* 99 (2007), p. 231102. arXiv: 0706.3203 [hep-ph].

[49] K. A. Hochmuth and G. Sigl. “Effects of Axion-Photon Mixing on Gamma-Ray Spectra from Magnetized Astrophysical Sources”. In: *Phys. Rev. D* 76 (2007), p. 123011. arXiv: 0708.1144 [astro-ph].

[50] A. De Angelis, O. Mansutti, and M. Roncadelli. “Axion-Like Particles, Cosmic Magnetic Fields and Gamma-Ray Astrophysics”. In: *Phys. Lett. B* 659 (2008), pp. 847–855. arXiv: 0707.2695 [astro-ph].

[51] A. Abramowski et al. “Constraints on axionlike particles with H.E.S.S. from the irregularity of the PKS 2155-304 energy spectrum”. In: *Phys. Rev. D* 88.10 (2013), p. 102003. arXiv: 1311.3148 [astro-ph.HE].

[52] M. Ajello et al. “Search for Spectral Irregularities due to Photon–Axionlike-Particle Oscillations with the Fermi Large Area Telescope”. In: *Phys. Rev. Lett.* 116.16 (2016), p. 161101. arXiv: 1603.06978 [astro-ph.HE].

[53] M. C. D. Marsh et al. “A New Bound on Axion-Like Particles”. In: *JCAP* 12 (2017), p. 036. arXiv: 1703.07354 [hep-ph].

[54] C. Zhang et al. “New bounds on axionlike particles from the Fermi Large Area Telescope observation of PKS 2155-304”. In: *Phys. Rev. D* 97.6 (2018), p. 063009. arXiv: 1802.08420 [hep-ph].

[55] C. S. Reynolds et al. “Astrophysical limits on very light axion-like particles from Chandra grating spectroscopy of NGC 1275”. In: *Astrophys. J.* 890 (2020), p. 59. arXiv: 1907.05475 [hep-ph].

[56] A. Payez et al. “Revisiting the SN1987A gamma-ray limit on ultralight axion-like particles”. In: *JCAP* 02 (2015), p. 006. arXiv: 1410.3747 [astro-ph.HE].

[57] C. Dessert, J. W. Foster, and B. R. Safdi. “X-ray Searches for Axions from Super Star Clusters”. In: *Phys. Rev. Lett.* 125.26 (2020), p. 261102. arXiv: 2008.03305 [hep-ph].

[58] C. Dessert, A. J. Long, and B. R. Safdi. “No Evidence for Axions from Chandra Observation of the Magnetic White Dwarf RE J0317-853”. In: *Phys. Rev. Lett.* 128.7 (2022), p. 071102. arXiv: 2104.12772 [hep-ph].

[59] D. Noordhuis et al. “Novel Constraints on Axions Produced in Pulsar Polar Cap Cascades”. In: (Sept. 2022). arXiv: 2209.09917 [hep-ph].

[60] M. J. Dolan, F. J. Hiskens, and R. R. Volkas. “Advancing globular cluster constraints on the axion-photon coupling”. In: *JCAP* 10 (2022), p. 096. arXiv: 2207.03102 [hep-ph].

[61] C. Dessert, D. Dunsky, and B. R. Safdi. “Upper limit on the axion-photon coupling from magnetic white dwarf polarization”. In: *Phys. Rev. D* 105.10 (2022), p. 103034. arXiv: 2203.04319 [hep-ph].

[62] K. Akiyama et al. “First M87 Event Horizon Telescope Results. VIII. Magnetic Field Structure near The Event Horizon”. In: *Astrophys. J. Lett.* 910.1 (2021), p. L13. arXiv: 2105.01173 [astro-ph.HE].

[63] K. Saito, J. Soda, and H. Yoshino. “Universal 10^{20} Hz stochastic gravitational waves from photon spheres of black holes”. In: *Phys. Rev. D* 104.6 (2021), p. 063040. arXiv: 2106.05552 [gr-qc].

[64] M. Ould El Hadj and S. R. Dolan. “Conversion of electromagnetic and gravitational waves by a charged black hole”. In: *Phys. Rev. D* 106.4 (2022), p. 044002. arXiv: 2106.09731 [gr-qc].

[65] K. Nomura, K. Saito, and J. Soda. “Observing axions through photon ring dimming of black holes”. In: *Phys. Rev. D* 107.12 (2023), p. 123505. arXiv: 2212.03020 [hep-ph].

[66] R. D. Peccei. “The Strong CP problem and axions”. In: *Lect. Notes Phys.* 741 (2008). Ed. by M. Kuster, G. Raffelt, and B. Beltran, pp. 3–17. arXiv: hep-ph/0607268.

[67] J. E. Kim. “Light Pseudoscalars, Particle Physics and Cosmology”. In: *Phys. Rept.* 150 (1987), pp. 1–177.

[68] P. Sikivie. “Axion Cosmology”. In: *Lect. Notes Phys.* 741 (2008). Ed. by M. Kuster, G. Raffelt, and B. Beltran, pp. 19–50. arXiv: astro-ph/0610440.

[69] G. G. Raffelt. “Astrophysical axion bounds”. In: *Lect. Notes Phys.* 741 (2008). Ed. by M. Kuster, G. Raffelt, and B. Beltran, pp. 51–71. arXiv: hep-ph/0611350.

[70] L. Di Luzio et al. “The landscape of QCD axion models”. In: *Phys. Rept.* 870 (2020), pp. 1–117. arXiv: 2003.01100 [hep-ph].

[71] V. Baluni. “CP Violating Effects in QCD”. In: *Phys. Rev. D* 19 (1979), pp. 2227–2230.

[72] R. J. Crewther et al. “Chiral Estimate of the Electric Dipole Moment of the Neutron in Quantum Chromodynamics”. In: *Phys. Lett. B* 88 (1979). [Erratum: Phys.Lett.B 91, 487 (1980)], p. 123.

[73] A. Arvanitaki et al. “String Axiverse”. In: *Phys. Rev. D* 81 (2010), p. 123530. arXiv: 0905.4720 [hep-th].

[74] P. A. R. Ade et al. “Planck 2015 results. XX. Constraints on inflation”. In: *Astron. Astrophys.* 594 (2016), A20. arXiv: 1502.02114 [astro-ph.CO].

[75] R. L. Workman et al. “Review of Particle Physics”. In: *PTEP* 2022 (2022), p. 083C01.

[76] V. Iršič et al. “First constraints on fuzzy dark matter from Lyman-α forest data and hydrodynamical simulations”. In: *Phys. Rev. Lett.* 119.3 (2017), p. 031302. arXiv: 1703.04683 [astro-ph.CO].

[77] H. Primakoff. “Photoproduction of neutral mesons in nuclear electric fields and the mean life of the neutral meson”. In: *Phys. Rev.* 81 (1951), p. 899.

[78] W. Heisenberg and H. Euler. “Consequences of Dirac’s theory of positrons”. In: *Z. Phys.* 98.11-12 (1936), pp. 714–732. arXiv: physics/0605038.

[79] J. S. Schwinger. “On gauge invariance and vacuum polarization”. In: *Phys. Rev.* 82 (1951). Ed. by K. A. Milton, pp. 664–679.

[80] I. H. Hutchinson. “Introduction to Plasma Physics”. http://silas.psfc.mit.edu/introplasma/. Lecture notes at MIT.

[81] K. S. Thorne and R. D. Blandford. *Modern classical physics: optics, fluids, plasmas, elasticity, relativity, and statistical physics*. Princeton University Press, 2017.

[82] M. Gell-Mann and A. Pais. “Behavior of Neutral Particles under Charge Conjugation”. In: *Phys. Rev.* 97 (5 Mar. 1955), pp. 1387–1389. URL: https://link.aps.org/doi/10.1103/PhysRev.97.1387.

[83] B. Pontecorvo. “Mesonium and anti-mesonium”. In: *Sov. Phys. JETP* 6 (1957), p. 429.

[84] Z. Maki, M. Nakagawa, and S. Sakata. “Remarks on the unified model of elementary particles”. In: *Prog. Theor. Phys.* 28 (1962), pp. 870–880.

[85] *Axion-photon coupling.* URL: https://cajohare.github.io/AxionLimits/docs/ap.html.

[86] J. K. Vogel et al. “IAXO - The International Axion Observatory”. In: *8th Patras Workshop on Axions, WIMPs and WISPs.* Feb. 2013. arXiv: 1302.3273 [physics.ins-det].

[87] A. Ayala et al. “Revisiting the bound on axion-photon coupling from Globular Clusters”. In: *Phys. Rev. Lett.* 113.19 (2014), p. 191302. arXiv: 1406.6053 [astro-ph.SR].

[88] P. Sikivie. “EXPERIMENTAL TESTS OF THE ”INVISIBLE” AXION”. In: *Phys. Rev. Lett.* 52 (8 Feb. 1984), pp. 695–695. URL: https://link.aps.org/doi/10.1103/PhysRevLett.52.695.2.

[89] P. Sikivie. “Detection Rates for ’Invisible’ Axion Searches”. In: *Phys. Rev. D* 32 (1985). [Erratum: Phys.Rev.D 36, 974 (1987)], p. 2988.

[90] C. Bartram et al. “Search for Invisible Axion Dark Matter in the 3.3–4.2 μeV Mass Range”. In: *Phys. Rev. Lett.* 127.26 (2021), p. 261803. arXiv: 2110.06096 [hep-ex].

[91] C. W. Misner, K. S. Thorne, and J. A. Wheeler. *Gravitation.* Macmillan, 1973.

[92] S. Shapiro and S. Teukolsky. *Black holes, white dwarfs and neutron stars: The physics of compact objects.* John Wiley and Sons Inc., New York, NY, 1983.

[93] H. Yoshino, K. Takahashi, and K.-i. Nakao. “How does a collapsing star look?” In: *Phys. Rev. D* 100.8 (2019), p. 084062. arXiv: 1908.04223 [gr-qc].

[94] I. D. Novikov and K. S. Thorne. “Astrophysics of black holes”. In: *Black holes (Les astres occlus)* 1 (1973), pp. 343–450.

[95] G. B. Rybicki. *Radiative Processes in Astrophysics.* Wiley-VCH, 2004. ISBN: 978-0-471-82759-7, 978-3-527-61817-0.

[96] K. Akiyama et al. “First M87 Event Horizon Telescope Results. I. The Shadow of the Supermassive Black Hole”. In: *Astrophys. J. Lett.* 875 (2019), p. L1. arXiv: 1906.11238 [astro-ph.GA].

[97] K. Akiyama et al. “First M87 Event Horizon Telescope Results. V. Physical Origin of the Asymmetric Ring”. In: *Astrophys. J. Lett.* 875.1 (2019), p. L5. arXiv: 1906.11242 [astro-ph.GA].

[98] J. .-. Luminet. “Image of a spherical black hole with thin accretion disk”. In: *Astron. Astrophys.* 75 (1979), pp. 228–235.

[99] A. Heger et al. “How massive single stars end their life”. In: *Astrophys. J.* 591 (2003), pp. 288–300. arXiv: astro-ph/0212469.

[100] M. J. Reid. “The distance to the center of the galaxy”. In: *Ann. Rev. Astron. Astrophys.* 31 (1993), pp. 345–372.

[101] S. Gillessen et al. “Monitoring stellar orbits around the Massive Black Hole in the Galactic Center”. In: *Astrophys. J.* 692 (2009), pp. 1075–1109. arXiv: 0810.4674 [astro-ph].

[102] J. P. Blakeslee et al. “The ACS Fornax cluster survey. V. Measurement and recalibration of surface brightness fluctuations and a precise value of the Fornax–Virgo relative distance”. In: *The Astrophysical Journal* 694.1 (2009), p. 556.

[103] S. Bird et al. “The inner halo of M 87: a first direct view of the red-giant population”. In: *Astronomy & Astrophysics* 524 (2010), A71.

[104] K. Gebhardt and J. Thomas. “The black hole mass, stellar mass-to-light ratio, and dark halo in M87”. In: *The Astrophysical Journal* 700.2 (2009), p. 1690.

[105] K. Gebhardt et al. “The black hole mass in M87 from Gemini/NIFS adaptive optics observations”. In: *The Astrophysical Journal* 729.2 (2011), p. 119.

[106] K. Akiyama et al. “First Sagittarius A* Event Horizon Telescope Results. I. The Shadow of the Supermassive Black Hole in the Center of the Milky Way”. In: *Astrophys. J. Lett.* 930.2 (2022), p. L12.

[107] K. Inayoshi, E. Visbal, and Z. Haiman. “The Assembly of the First Massive Black Holes”. In: *Ann. Rev. Astron. Astrophys.* 58 (2020), pp. 27–97. arXiv: 1911.05791 [astro-ph.GA].

[108] A. Marconi and L. K. Hunt. “The relation between black hole mass, bulge mass, and near-infrared luminosity”. In: *Astrophys. J. Lett.* 589 (2003), pp. L21–L24. arXiv: astro-ph/0304274.

[109] R. Narayan and I.-s. Yi. “Advection dominated accretion: A Selfsimilar solution”. In: *Astrophys. J. Lett.* 428 (1994), p. L13. arXiv: astro-ph/9403052.

[110] R. Narayan and I. Yi. “Advection dominated accretion: Underfed black holes and neutron stars”. In: *Astrophys. J.* 452 (1995), p. 710. arXiv: astro-ph/9411059.

[111] T. Manmoto, S. Mineshige, and M. Kusunose. “Spectrum of optically thin advection dominated accretion flow around a black hole: application to sgr a*”. In: *Astrophys. J.* 489 (1997), p. 791. arXiv: astro-ph/9708234.

[112] F. Yuan and R. Narayan. "Hot Accretion Flows Around Black Holes". In: *Ann. Rev. Astron. Astrophys.* 52 (2014), pp. 529–588. arXiv: 1401.0586 [astro-ph.HE].

[113] E. Quataert. "A thermal bremsstrahlung model for the quiescent x-ray emission from sagittarius a*". In: *Astrophys. J.* 575 (2002), pp. 855–859. arXiv: astro-ph/0201395.

[114] P. Uttley et al. "The high energy Universe at ultra-high resolution: the power and promise of X-ray interferometry". In: *Exper. Astron.* 51.3 (2021), pp. 1081–1107. arXiv: 1908.03144 [astro-ph.HE].

[115] E. Masaki, A. Aoki, and J. Soda. "Stability of Axion Dark Matter-Photon Conversion". In: *Phys. Rev. D* 101.4 (2020), p. 043505. arXiv: 1909.11470 [hep-ph].

[116] R. Brito, V. Cardoso, and P. Pani. "Superradiance: New Frontiers in Black Hole Physics". In: *Lect. Notes Phys.* 906 (2015), pp.1–237. arXiv: 1501.06570 [gr-qc].

[117] J. A. Dror, H. Murayama, and N. L. Rodd. "Cosmic axion background". In: *Phys. Rev. D* 103.11 (2021), p. 115004. arXiv: 2101.09287 [hep-ph].